Experimental investigation of relevant road surface descriptors for tire-road noise measurements on low-absorbing road surfaces

Zur Erlangung des akademischen Grades eines

DOKTORS DER INGENIEURWISSENSCHAFTEN

(Dr. -Ing.)

von der KIT-Fakultät für Maschinenbau des
Karlsruher Instituts für Technologie (KIT)

genehmigte

DISSERTATION

von

M.Sc. Julien Pinay

geb. in Vendôme

Tag der mündlichen Prüfung: 06.10.2023

Hauptreferent: Prof. Dr. rer. nat. Frank Gauterin
Korreferent: Prof. Dr.-Ing. Wolfgang Kropp

Vorwort des Herausgebers

Die Fahrzeugtechnik ist kontinuierlich Veränderungen unterworfen. Klimawandel, die Verknappung einiger für Fahrzeugbau und –betrieb benötigter Rohstoffe, globaler Wettbewerb, gesellschaftlicher Wandel und das rapide Wachstum großer Städte erfordern neue Mobilitätslösungen, die vielfach eine Neudefinition des Fahrzeugs erforderlich machen. Die Forderungen nach Steigerung der Energieeffizienz, Emissionsreduktion, erhöhter Fahr- und Arbeitssicherheit, Benutzerfreundlichkeit und angemessenen Kosten sowie die Möglichkeiten der Digitalisierung und Vernetzung finden ihre Antworten nicht aus der singulären Verbesserung einzelner technischer Elemente, sondern benötigen Systemverständnis und eine domänenübergreifende Optimierung der Lösungen.

Hierzu will die Karlsruher Schriftenreihe für Fahrzeugsystemtechnik einen Beitrag leisten. Für die Fahrzeuggattungen Pkw, Nfz, Mobile Arbeitsmaschinen und Bahnfahrzeuge werden Forschungsarbeiten vorgestellt, die Fahrzeugsystemtechnik auf vier Ebenen beleuchten: das Fahrzeug als komplexes, digitalisiertes mechatronisches System, die Mensch-Fahrzeug-Interaktion, das Fahrzeug in Verkehr und Infrastruktur sowie das Fahrzeug in Gesellschaft und Umwelt.

Verkehrslärm ist störend und kann gesundheitlich negative Auswirkungen haben. Der Gesetzgeber schreibt daher die Einhaltung von Geräuschemissionsgrenzwerten vor, die in den kommenden Jahren weiter abgesenkt werden. Die Geräuschemission wird bei modernen Automobilen und insbesondere bei Elektrofahrzeugen bei Geschwindigkeiten unterhalb 130 km/h fast ausschließlich durch den Reifen-Fahrbahn-Rollkontakt erzeugt. Für die Fahrzeughomologation ist die Durchführung von Geräuschmessungen auf einer Fahrbahn verlangt, die der internationale Norm ISO 10844 entspricht. Nach diesem Standard gefertigte Strecken weisen jedoch untereinander deutliche Unterschiede der Geräuschmesswerte auf. Die zur Geräuschcharakterisierung vorgeschriebenen

Kenngrößen der Mittleren Rauigkeitstiefe und des Schallabsorptionsgrads sind nicht ausreichend, um diese Unterschiede zu erklären.

Hier setzt die Arbeit von Herrn Pinay an, in der er die Einflussgrößen und ihre Wechselwirkungen auf das Vorbeirollgeräusch auf einer größeren Anzahl von ISO-Strecken sowie weiterer Fahrbahnen in Versuch und Simulation analysiert. Er erarbeitet dabei neue Kenngrößen zur Charakterisierung der Geräuschemission, deren Relevanz insbesondere für ISO-Strecken er nachweist. Besonders ausführlich betrachtet er den bislang wenig untersuchten Beitrag von stehenden Wellen in Reifenprofilrillen in der Bodenaufstandsfläche. Unter Verwendung der neuen Kenngrößen erstellte Prädiktionsmodelle erlauben eine genauere Vorhersage des Schalldruckpegels beim Vorbeirollen von Pkws.

Frank Gauterin

Karlsruhe, im Oktober 2023

Acknowledgements

I would like to thank my colleagues in the laboratory, Kerstin Dietrich, Markus Diehm, Julian Deeg and Jochen Bodmer, for their support in carrying out measurements on the inner drum test bench and for helping me with the (many) technical problems that occurred.

One of my - if not the - biggest thanks goes to my test driver, master mechanic and handyman Benjamin Töpfer. I can not thank you enough for the time we spent during the field measurements, driving more than 12 000 km through four countries in Europe. I would not have got so much data in such a small time schedule without your constant availability, flexibility and professionalism.

I would also like to thank the numerous students who have gained important insights during their diploma, master or bachelor theses. To name just a few of them, I would like to thank Xiaoji Cao and Victor Hittinger for developing tools that enabled the numeric analysis of the groove resonance phenomenon. My thanks also go to Tobias Klesen and Tomasz Gütschow for the thorough literature reviews they performed under my supervision.

I would like to thank my colleagues at the Institute for the very friendly and cordial working atmosphere, the fruitful discussions and for the spare time out of office. The past few years would have been only half as beautiful without all of you.

Finally, I would like to thank my family, who always supported me during this long time spent at the university. By constantly asking the same question that each PhD student loves to hear: "How is you PhD going? When will you finish it?", you somehow motivated me to write down this thesis.

Julien Pinay

Feldkirch, October 2023

Abstract

Due to acoustic improvements from the automotive industry, the contact between the tire and the road is now the major noise source outside the vehicle. This tendency will worsen with the development and spreading of electric vehicles. As the demand from people and politics for a reduced traffic noise increases, the regulation for tire and vehicle approval is strengthened on a regular basis. Further research on the influence of the road surface characteristics on noise emission of tires and vehicles is therefore needed.

This work aims at identifying relevant road surface characteristics to mitigate tire-road noise of free-rolling tires using a systematic approach. As using open porous roads is already known as an efficient measure to reduce tire rolling noise, this study will focus on compact road surfaces which have a low acoustic absorption. Mechanisms generating tire-road noise will be first presented, as well as the main research results concerning the influence of tire and road characteristics on tire-road noise emission. After giving the necessary theoretical background to understand this work, different methods used to acoustically analyze the interaction between the road surface and the tire will be presented. These methods are divided in two groups: measurement and statistical methods.

Application of statistical methods to road surface and tire-road noise measurements enables several possibilities. First, multidimensional data are reduced to scalars so that the numbers of parameters used as input is reduced to its minimum. Then the most relevant road surface parameters are identified to reduce tire-road noise and some of its sub-phenomena such as groove resonance. In the end, an analysis is performed to see if the definition of the approval test track according to the ISO 10844 standard is complete enough or if additional parameters are needed to explain the noise variance between different standardized tracks. Using all gathered information, an optimal road surface design can be given in order to reduce tire-road noise emission for tire approval tests but also for standard rolling conditions on public roads.

Kurzfassung

Aufgrund von geräuschsenkenden Maßnahmen der Automobilindustrie ist der Kontakt zwischen Reifen und Straße heute die wichtigste Geräuschquelle außerhalb des Fahrzeugs. Diese Tendenz wird sich mit der Verbreitung von Elektrofahrzeugen noch verstärken. Mit zunehmender Forderung von Bevölkerung und Politik nach einer Reduzierung des Verkehrslärms wird die Regelung für die Reifen- und Fahrzeugzulassung regelmäßig verschärft. Daher sind weitere Untersuchungen über den Einfluss der Eigenschaften der Fahrbahnoberfläche auf die Geräuschemission von Reifen und Fahrzeugen erforderlich.

Ziel dieser Arbeit ist es, die relevanten Fahrbahneigenschaften zu identifizieren, um das Reifen-Fahrbahn-Geräusch von frei rollenden Reifen mit einem systematischen Ansatz zu mindern. Da die Verwendung offenporiger Asphalte bereits als effiziente Maßnahme zur Reduzierung des Reifenrollgeräusches bekannt ist, konzentriert sich diese Arbeit auf kompakte Straßenoberflächen mit geringer Schallabsorption. Zunächst werden die Mechanismen, die Reifen-Fahrbahngeräusche erzeugen, sowie die wichtigsten Forschungsergebnisse über den Einfluss der Reifen- und der Straßeneigenschaften auf die Reifen-Fahrbahngeräusche vorgestellt. Nachdem die notwendigen theoretischen Grundlagen zum Verständnis dieser Arbeit vermittelt wurden, werden die verschiedenen Methoden zur akustischen Analyse der Wechselwirkung zwischen Fahrbahnoberfläche und Reifen vorgestellt. Diese Methoden werden in zwei Gruppen unterteilt: die Mess- und die statistischen Methoden.

Die Anwendung statistischer Methoden auf die Messung der Fahrbahnoberfläche und des Reifenfahrgeräusches bietet mehrere Vorteile. Erstens können multidimensionale Daten auf Skalare reduziert werden, so dass die Anzahl der als Eingabe verwendeten Parameter minimiert wird. Dann können die wichtigsten Straßenbelagsparameter identifiziert werden, um das Reifen-Fahrbahngeräusch und einige seiner Entstehungsmechanismen wie die Rillenresonanz zu reduzieren. Am Ende wird eine Analyse durchgeführt, um festzustellen, ob die Definition der Homologationsprüfstrecke nach der Norm ISO 10844 vollständig

genug ist oder ob zusätzliche Parameter benötigt werden, um die Geräuschvarianz zwischen verschiedenen, der Norm entsprechenden Prüfstrecken zu erklären. Anhand aller gesammelten Informationen kann eine optimale Straßenbelagsgestaltung vorgenommen werden, um die Reifen-Fahrbahn-Geräusche bei Homologationstests, aber auch bei normalen Rollbedingungen auf öffentlichen Straßen zu reduzieren.

List of Abbreviations

CPX	Close-proximity method
FPC	Functional principal component
FPCA	Functional principal component Analysis
KIT	Karlsruhe Institute of Technology
NOA	Noise-optimized asphalt
PMA	Porous mastic asphalt
RMSE	Root mean square error
SMA	Stone mastic asphalt
SPL	Sound pressure level
TiRN	Tire-road noise

Nomenclature

Road surface descriptors

α	Absorption coefficient	%
$\tilde{z}_\lambda$	Root mean square of the filtered profile centered at the wavelength band λ	m
g	Shape factor	%
$Z(x)$	Measured road surface profile	m
Abbott FPC$_i$	i^{th} Functional principal component of the Abbott curve	–
END$_T$	Expected pass-by noise level difference from texture level variation of the road surface	dB
Ltx FPC$_i$	i^{th} Functional principal component of the texture amplitude spectrum	–
MPD	Mean profile depth	mm
MTD	Mean texture depth	mm
RKU	Kurtosis	–
RMS	Root mean square	mm
RSK	Skewness	–

Statistic descriptors

β	Regression coefficients	–
$\chi(t)$	Functional data	–
ϵ	Residuals	–
$\overline{\chi}$	Average value of χ	–
$\phi_k(t)$	k^{th} eigenfunction	–
$\psi_n(t)$	n^{th} independent function	–
ρ	Pearson's correlation coefficient	–

σ	Standard deviation	–
$\widehat{\chi}$	Estimate of χ	–
c_n	Basis functions coefficient	–
$F(Z)$	Complementary cumulative distribution function of $Z(x)$	–
$P(Z)$	Probability density function of $Z(x)$	–
R^2	Coefficient of determination	–
r_s	Spearman's correlation coefficient	–
s	Shrinkage coefficient	–
X	Explanatory variables	–
Y	Predicted outcome	–
RSS	Residuals sum of squares	–
TSS	Total sum of squares	–
VIF	Variance inflation factor	–

Other descriptors

γ	SPL Temperature correction coefficient	dB/°C
λ	Texture wavelength	mm
a, b	Speed coefficients	dB
A, B, C	Coefficients for the computation of END_T	dB
c_{sound}	Speed of sound	m/s
f	Frequency	Hz
f_{groove}	Groove resonance frequency	Hz
L	Length of the measured road surface profile	m
L_{groove}	Groove length	m
T	Road surface temperature	°C
v	Driving speed	km/h

Table of Contents

1 Introduction

1.1 Motivation

The mobility industry is undergoing one of the greatest changes since the invention of motorized passenger cars by Carl Benz in 1886. Autonomous, electrified and connected vehicles, as well as new mobility concepts are constantly being developed, while adapting to constant changing requirements such as ecology, safety, energy efficiency and improved quality of life.

Between 1996 and 2016, the number of the passenger car fleet grew in the European Union by 42 % [1]. This led to a constant increase of the number of people exposed every day to a certain noise level that could have consequences on public health. In 2017, more than 78 million people in the EU were exposed to an average day-evening-night noise level of 55 dBA, which corresponds to 15 % of the EU population. More than 55 million EU citizens suffer a night noise level above 50 dBA when the World Health Organization recommends a night noise limit at 40 dBA [2].

Traffic noise has therefore consequences on the appreciation of life quality near roads [3] but also has an impact on public health. Long-time exposure to traffic noise increases the risk of having cardiovascular diseases [4], hypertension [5] or myocardial infarction [6]. A recent study performed by the Danish Ministry of Infrastructure and Environment estimated the costs savings by reducing the traffic noise by 6 dBA between 2009 and 2020. Such a reduction of traffic noise would lead to 13 million less people annoyed and 6 million less people sleep-disturbed by it [7].

Traffic noise is composed of many noise sources. Among them can be cited motor and powertrain noise, aerodynamic turbulence, noise caused by the exhaust system or brake squealing. However, it was demonstrated in [8] that nowadays, tire-road noise (TiRN) induces the major part of traffic noise not

only above 40 km/h, but in all driving conditions. This tendency is going to increase given the growing interest in electro-mobility which will logically lead to the disappearance of the acoustic contribution of combustion engines.

These studies led the regulation authorities to strengthen the regulation for tire approval tests. For a tire nominal width between 185 mm und 275 mm, the maximal noise emission has been reduced by four to five decibels [9]. Although the test track used for acoustic approval of tires is standardized, it is widely known that one tire can show up to 3 dBA difference from one standardized track to another [10].

Several questions arise that this research work will try to answer: Are the parameters used to describe standardized test tracks adequate enough? Which road surface characteristics are relevant for TiRN? Are road surface characteristics of standardized test tracks representative of public roads?

1.2 State of the art

The influence of many parameters on TiRN emission has been investigated over the years and can be clustered in three categories: operating parameters, tire and road surface parameters. The influence of each category are summarized in the following three sections, which are based on [11, 12].

1.2.1 Operating parameters influence on tire-road noise

Driving speed

Findings of multiple researchers are consistent: the relationship between TiRN and driving speed follows a similar trend for different tire-road combinations [8, 13]. Researchers at the Technical University of Gdansk collected 1700 data points and determined only minor deviation from a regression line between TiRN and the logarithm of the speed [8]. The TiRN Sound Pressure Level (SPL) can be modeled by Eq. 1.1:

$$SPL = a + b \cdot \log v \tag{1.1}$$

where: SPL Sound Pressure Level [dB]

a, b Speed coefficients (constants)

v Driving speed [km/h]

Both speed coefficients a and b of Eq. 1.1 are quantified by numerous re-searchers, giving substantial meaning to this equation. a-values range mostly between 15 and 35 while b-values vary between 30 and 40 [8]. This equation is valid and proven for multiple surfaces, although irregularities in certain frequencies and on certain surfaces can occur. Those irregularities are tonal components that mostly appears, when tread pattern frequencies coincide with tire resonance frequencies, creating a vibration peak and subsequently maxi-mum noise emission [8].

Beside tire optimization, a reduction of highway speeds is often used to limit highway traffic noise. It is shown in [14] that limiting speeds from 120 km/h to 100 km/h leads to a decrease of TiRN emission of approx. 2 dBA.

Tire load

Tire load variation has various effects on the tire-road interaction. An increase in tire load will influence the tire rotational symmetry and change its foot-print shape [8]. Not only will the tire contact patch become bigger, but load distribution will also change. Increasing tire load usually means that the tire shoulder carries more weight compared to the tire center. This can lead to a high increase in TiRN if the tire shoulders have a relative aggressive tread pattern design compared to the tire tread center [15].

Figure 1.1 illustrates the tire footprint shape evolution upon different tire loads. It is clearly visible that a higher load leads to an increase of the footprint area, both in longitudinal and lateral direction [8]. The dependency of the footprint width and length upon tire load was analyzed experimentally in [16]. While the footprint length grows linearly with the driving speed, an increase in tire load will lead to a non-linear width increase. Depending upon the tread pattern, this should have an influence on the pipe network and on groove resonance noise [17]. An extensive study of this phenomenon will be presented in section 4.2.

(a) 2400 N	(b) 3600 N	(c) 4800 N
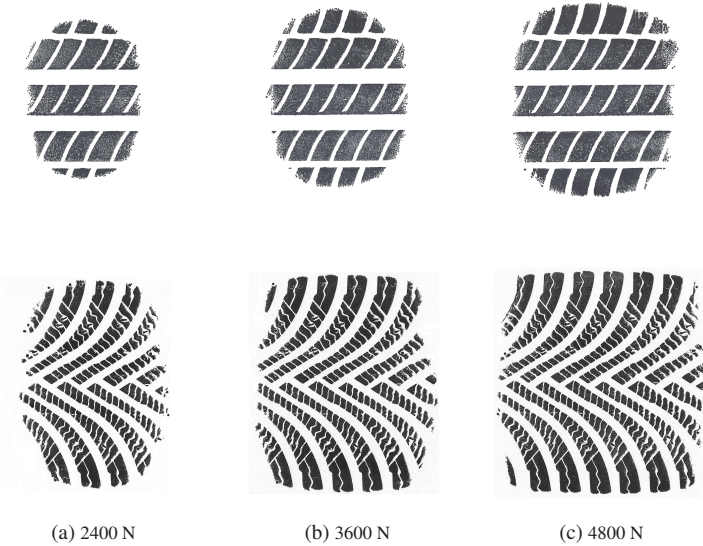
Figure 1.1: Tire load influence on tire contact patch

Tire load measurements are mostly done in laboratory conditions, where adjusting contact pressure is easily realized. Consequences of increased tire load are however a complicated function of tire type, inflation, speed and road surface [8]. Adjusting tire load influences numerous other tire parameters as well as TiRN generation mechanism. An overview of the subphenomena generating TiRN is given in section 2.1. The influence of tire load variation on the predominant mechanism generating TiRN will therefore determine the overall influence of tire load on total TiRN [8]. An increase in tire load on a rough surface will not have the same effect as an increase in tire load on a smooth surface. A generalization of tire load influence on TiRN is however not possible, because each generating mechanism is differently affected by tire load variation.

Already in 1982, researchers measured a TiRN increase of 1 dBA to 2 dBA by doubling the tire load of a car, if inflation pressure is adjusted to the load [18]. If the road surface has a high texture level, an increased tire load leads to a decreased TiRN in the low frequency range between 400 Hz to 800 Hz.

This can be explained by a reduced contribution of noise due to road texture impact. At medium frequencies (1 kHz to 1.25 kHz), higher tire load leads to an increase of TiRN. A possible explanation would be a higher contribution of air pumping noise and other aerodynamic mechanisms. Furthermore, there is also a positive correlation between a load increase and a noise increase in the high frequency range starting at 3 kHz. This frequency range can typically be attributed to enhanced friction noise. A higher tire load is probably causing higher tangential and adhesion forces, resulting in higher stick-slip and stick-snap effects [8].

On the other hand, it has been found in [19] that TiRN generally increases when increasing tire load by 80 %, except in the medium to high frequency range from 1100 Hz to 1700 Hz. By comparing the spectra of the acceleration measured on the wheel hub with the emitted noise, they found out that a load increase led to a decrease of axial vibration amplitude in this specific frequency range. As inflation was not adapted to the different tire load steps, the authors suggest that increasing tire load would lead to an increased tread and sidewall stiffness and could reduce noise radiation, as it is more difficult for the tire to deform [19]. This interpretation might be true for the sidewall stiffness, but as the inflation pressure was kept constant, the contact patch should become larger but the tread stiffness should not have increased significantly.

The interaction between tire load and driving torque also influences TiRN [20]. The overall TiRN level of a tire under driving torque was highest at a tire load of 3000 N, followed by 2000 N and 1000 N. During rolling condition, the medium tire load of 2000 N was measured as the most silent setup. Based on that, one can assume that under certain driving scenarios, TiRN increases when deviating from an ideal tire load in both negative and positive direction [20].

Other researcher highlight clear effect of tire load on TiRN. An increase of 7 dBA was measured by doubling the load of a truck tire from 5.9 t to 13.2 t [21]. Due to the differences in findings, current literature highlights the dependence on multiple aspects of load effect on noise. Rib tires are not very sensitive and relatively unaffected by tire load variations, with changes mostly below 1 dBA when doubling tire load [8, 15]. However, aggressive tire tread pattern or laterally grooved tires are especially sensitive to tire load. Globally, current literature still determines positive correlation of load influence on TiRN, especially under propulsion or at aggressive tread patterns [8].

Temperature

When examining the influence of temperature on TiRN, it is necessary to differentiate between three different types of temperature measurements: air, road and tire temperature. Temperature influences rubber properties and alters the frictional and vibrational behavior of a tire [8]. Higher temperatures typically reduce contact stiffness due to decreasing tread compound hardness. Additionally, rising tire temperatures may increase tire inflation pressure, due to air volume increase. TiRN measurements are typically performed at ambient temperatures between 5 °C and 30 °C, which may falsify tests by 2 dBA to 3 dBA only due to different temperatures [8].

Current research usually indicates a negative correlation between TiRN and temperature, which is confirmed in [22] for eight of the ten tested tires. When only considering tires with acceptable correlation, an average noise reduction of 0.11 dBA per positive degree of air temperature was found (0.10 dBA for road temperature).This noise reduction is confirmed in [23], with noise levels varying on average by 0.1 dBA/°C for multiple surfaces, although results are highly dependent on the tire type. Applying this to central Europe with a typical air temperature scale of −15 °C to 40 °C, this would lead to a TiRN variation of approx. 6 dBA over the complete temperature range [22].

It was shown in [24] that an increased temperature leads to a decrease of TiRN at low frequencies (below 500 Hz) and high frequencies (1.6 kHz to 5 kHz). Tire and road stiffness decrease with increasing temperature, which reduces contact forces and therefore tire excitation. This will lead to a reduced contribution of road impact noise to TiRN [24]. The medium frequency range above 500 Hz is not strongly influenced by temperature, which could be explained by a non-significant influence of temperature on high-frequency vibration noise and low-frequency air pumping noise. The high-frequency noise reduction could be an effect of decreased friction coefficient and adhesion sensitivity to temperature [24]. This hypothesis is supported in [23], where temperature correction coefficients are highest for frequencies above 1.6 kHz.

As mentioned before, temperature tests can be obtained by varying either air, road or tire temperature. Therefore, multiple researchers review the correlation between these three measurement methods in an effort to agree on a unique measurement procedure. Measurements of road surface temperatures coupled to TiRN measurements in a trailer are presented in [25]. The observed noise

reduction of 0.06 dBA/°C using pavement temperature is in line with other researchers, although lower as the average coefficients for air temperature. Indeed, the correction value for road surface is expected to be lower than air and tire values, as the road pavement temperatures fluctuate more, because asphalt stores thermal energy e.g. from exposure to sunlight [25]. Coast-By measurements were performed while measuring all three different temperatures with two test tires on seven different road surfaces. TiRN decreases with increased temperature for all seven road surfaces, with correlation coefficients between 82 % and 84 % for all three forms of temperature measurements [24]. In [22], correlation results also varied between 76 % and 78 %, where the correlation between road and air temperature was determined at 97 %, when neglecting a specific test day with rain. This is supported by [26] with a value of 95 % when comparing road and air temperatures on four different surfaces. This supports the hypothesis that a correction based on air temperature is sufficient to capture TiRN deviations [22, 24, 25].

For tire approval test according to regulation R117, a temperature correction must be applied using road temperature measurements [9]. The temperature-corrected SPL is computed using a reference road surface temperature of 20 °C according to Eq. 1.2:

$$\text{SPL}_{A_{max}}(20\,°C) = \text{SPL}_{Amax}(T) - \gamma \cdot (T - 20) \tag{1.2}$$

where: $\text{SPL}_{A_{max}}$ Maximum A-weighted SPL [dBA]

          T Surface temperature [°C]

          γ Temperature correction coefficient [dBA/°C]

The correction factor γ equals 0.03 dBA/°C, if the test surface temperature is above 20 °C and 0.06 dBA/°C otherwise [9].

Inflation pressure

The higher the tire inflation, the more load will be carried at the tire center while less load is supported by the tire shoulders [27]. Higher inflation increases tension in the tire sidewalls and results in a lessened flexibility. A reduced

deflection through tread impact and less vibrational excitation of the tire are therefore expected [8].

Maximizing inflation pressure within reasonable safety limits might be useful to minimize tire deformation and reduce TiRN emission [28]. In [29], TiRN increases by approx. 2.1 dBA when increasing tire inflation by 50 %. In [8] however, inflation changes were found to be inconsistent in terms of TiRN emission. On a smooth surface, a 10 % increase of inflation resulted in a noise increase of 0 dBA to 0.3 dBA, while noise decreased by 0.2 dBA on a rough surface.

These inconsistencies are best analyzed along the frequency spectrum but remain difficult to interpret. In the low frequency range on rough surfaces, higher inflation favors a reduction of TiRN. On smooth surfaces however, TiRN emission seems to increase between 1250 Hz and 2500 Hz at higher inflation [8]. High tire pressures are positive for TiRN emission in low frequencies, while negative effects are observed in the medium to high frequency range. As for other operating parameters, an influence of inflation pressure on TiRN is expected if – for the specific tire-road combination tested – the major generation mechanism of TiRN is affected by it [8].

In general, inflation effects on TiRN seem to depend on the vehicle speed, as research indicates more prominent influence until 80 km/h, but weaker effect at higher speeds [8]. The generation mechanism highly depends on the roughness of the road surface. On rough surfaces, a 20 % inflation increase leads to a noise reduction in the low frequency range by up to 8 dBA. On a smooth surface, the same inflation increase will lead to an increase of TiRN between 2 dBA and 3 dBA in the medium to high frequency range. In general, a fluctuation of the inflation pressure can lead to a variation of TiRN by up to 1 dBA [8].

In this research work, the inflation pressure will be adjusted during the measurements in order to have a constant inflation of 2.5 bar in warm state.

1.2.2 Tire influence on tire-road noise

The characteristics of a tire can be summarized in four groups: its dimensions (width, diameter, cross section), structure, tread pattern and rubber compound.

Although the tested tires will have the same dimension, the structure, tread pattern and rubber compound will vary and affect differently TiRN.

Tire dimension

Tire width is the most commonly researched dimensional parameter of a tire. A wider tire displaces more air volume, which results in an increased aerodynamic influence on the tire and therefore leads to a higher TiRN emission [8, 30]. As the volume of the horn-shaped geometry in front of the tire increases with tire width, the horn effect is more effective which also affects TiRN propagation. A wider tire will lead to a bigger footprint and to a more pronounced interaction of the tread blocks with the road surface per unit time [30]. The global length of the tread blocks impacting the road and being released at the trailing edge also increases per unit time, which leads to an enhanced sound radiation. Accordingly, this leads to a greater mechanical excitation of the tire in both radial and tangential directions and to a transmission of vibration into the sidewalls [8].

Data averaged from different publications show an increase of TiRN of approximately 0.5 dBA per 10 mm width [8], while a more recent study suggests a higher influence of tire width on noise emission [30]. Here, measurements performed on two test sites show that TiRN increases between 0.92 dBA and 0.97 dBA per 10 mm tire width.

When analyzing the tire outside diameter, results are not necessarily consistent, although there is a tendency that noise decreases with larger tire outside diameters [8]. The problematic nature of measuring noise differences when alternating tire diameter is that a change of dimension of the same tire results in consequent changes in tire carcass, tread and groove size.

Generally, a larger tire diameter decreases the tire attack angle. This influences road impact and aerodynamic mechanisms in opposite ways. A lower TiRN is observed if the diameter increases, because of a smaller attack angle. This results in a smoother impact of the tire on the road and therefore to a reduced vibrational excitation of the tire. This is especially visible on rough surfaces [8]. The tread blocks deformation also takes place over a longer time span, which could lead to a reduction of tread impact noise [8]. On the other hand, a larger diameter would lead to an increase of the TiRN amplification mechanisms. The

horn effect efficiency is namely expected to increase if the horn does not open too rapidly. Therefore, researchers in [8, 30] determine a positive correlation of tire diameter with TiRN amplification and a negative correlation with the impact generation mechanisms, although tendencies remain speculative.

Tire structure

There is not much literature about the influence of the tire inner structure on TiRN emission. However, a literature review showed that radial tires are in average 2 dBA less noisy than bias tires [8]. Belt stiffness also seems to have an influence but conclusions from several papers disagree. An increased belt stiffness leads to a reduction of TiRN in [18] while positive effects of an increased tire carcass stiffness on TiRN emission are depicted in [31]. A combination of high tire shoulder stiffness and lower belt tension at the tread center leads to less TiRN in [32]. Simulation results suggests that increasing tire bending stiffness can reduce TiRN if the belt mass is also increased [33]. A more recent study showed that optimizing belt structure could reduce vibration noise by 7.5 dB [34].

Tread pattern

A tire without pitch length variation generates TiRN at discrete frequencies corresponding to the tread pattern fundamental frequency. A solution to this problem is a variable tread segment pitch, which distributes noise power along the spectrum [35]. Tread randomization is the key parameter to avoid droning noise due to extreme tire excitation, when multiple tread blocks successively impact the road with the same time interval. Hence, noise emission of a tire largely depends on the pitch length and the distribution of the tread blocks [35]. Modern tires feature randomized, unequal pitch arrangement. Tread pattern randomization disperses tonal components and avoids TiRN concentration on a small frequency band. Nowadays, tread randomization is supported by 3D modeling and computational tire pitch optimization algorithms [8, 36]. In [37], it is concluded that higher void proportion – especially in lateral direction – typically increases the amplitude of the fundamental frequency and the corresponding harmonics.

An effect resulting from the individual tread pattern of a tire is its air ventilation ability [8]. The tread pattern is a key factor for TiRN generation phenomenon of air pumping and consequent aerodynamic noise effects. Approaching air will find the path of least resistance through or around the tire when a vehicle is moving [8]. Accordingly, the objective is to form ventilation channels with similar requirements as the water drainage properties. A tire which is prone to aquaplaning will probably be prone to allow air pumping mechanism to occur greatly [8]. Experiments with specific air pockets or narrow ventilation outlets resulted in increased noise emission due to alternating local pressure zones [8]. Only a groove ventilation can reduce the negative effects of closed tire pockets on TiRN emission and ensure that groove resonances remain limited [38, 39]. In [40], noise related to circumferential groove resonances of passenger car tires is observed at a frequency close to 1000 Hz.

In [37], the trade-off between low and high tire tread stiffness is explained. A low stiffness leads to a higher deflection of the tread elements, while a high stiffness leads to a higher transmission of road excitation to the tire carcass. A higher tread stiffness therefore increases TiRN emission due to tensions within the tread block. Additionally, damping capabilities of stiff tread blocks are limited, which may overlay vibrations in the tire carcass [38]. Reducing tire tread stiffness by using microslots can also be used to reduce TiRN by several decibels [38]. This approach is supported in [39] and it is mentioned to keep the stiffness rather low and constant for each individual tread segment to have a low-noise pattern design.

In [38], lateral groove widths between 2 mm and 12 mm are tested (see upper part of Fig. 1.2). A groove width of 2 mm features similar TiRN emission to a slick tire, as the grooves are too small to imply great influence on TiRN. A noise increase is observed for a groove width increase from 2 mm to 9 mm. A further width increase above 9 mm leads however to a reduced TiRN emission. The noise reduction while increasing the groove width from 9 mm to 12 mm is expected to be related to lower air pumping influence due to better groove ventilation [38]. By using a hybrid statistical/physical approach on ventilated S-shaped grooves, a slight noise reduction with increasing groove width is observed, especially in peak TiRN frequencies [39]. The groove width influence is prominent starting at 500 Hz and up to approx. 1.25 kHz. These results differ slightly from [38], where the void ratio was not kept constant for all tires and the groove pattern is much coarser than in [39].

11
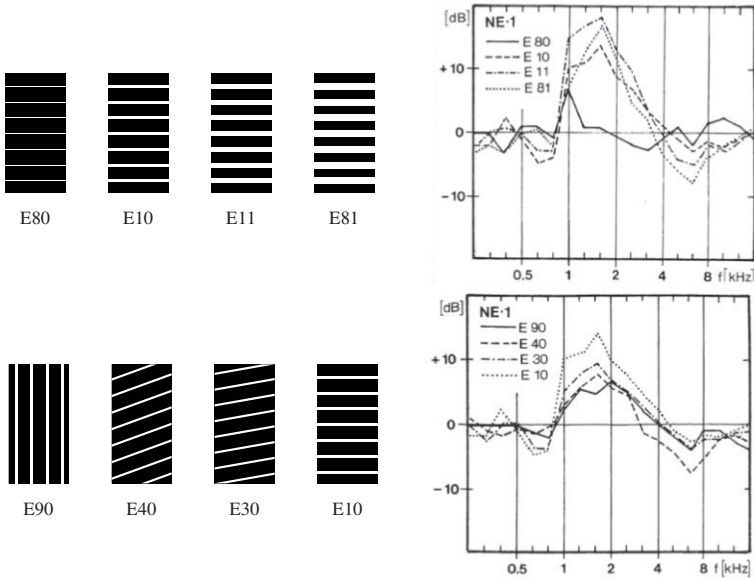
Figure 1.2: Groove angle and groove width influence on TiRN compared to a slick tire (from [38]). The measurements are performed on an outer drum with a road surface replica.

Groove angle also influences tread pattern noise. Tests of tread randomization through curved tread blocks indicated that the impact direction of the tread block at the leading edge is the most determining factor for TiRN [8, 38, 41]. TiRN decreases with inclined groove angle opposed to fully lateral grooves, because this configuration avoids simultaneous impact of multiple tread blocks over the tread width [15]. Thus, an optimal impact angle of the tread elements at the leading edge of the tire is vital for a better noise perfomance of a tire.

The lower part of Fig. 1.2 illustrates the influence of groove angle on the TiRN spectrum. Grooves with an inclination of 0°, 60°, 75° and 90° are tested. An inclination angle of 0° depicts a tire with longitudinal grooves and an angle of 90° corresponds to a tire with lateral grooves only. Over the complete speed range, a reduced groove angle is beneficial to mitigate TiRN, as the abruptness of the tread impact on the road is reduced. The influence of inclination angle on tread impact noise seems to decrease above 60°. On the contrary, lateral

grooves can lead to a high noise emission, especially at speeds where the tread impact frequency coincides with the groove resonance frequency [38].

When assuming that the lateral groove has a straight shape, researchers developed an equation to determine the "magic angle" of lateral grooves based on the groove width and length, where TiRN theoretically becomes zero [41]. Using a prototype tire tested on a drum facility, the simulation results showed very good agreement with the measurements

Another important parameter is the tread depth which is correlated to tire wear. Tire wear results in loss of tread rubber material which goes with lower tread grooves or even changes in the tread pattern [42]. Tire wear usually decreases the air/rubber ratio, as the corresponding air channels decrease in volume. Accordingly, airflow through the groove system is modified. Reduced tread height may also manipulate the tread block dynamic stiffness and change the vibrational characteristics of the tire. This can also influence its damping capabilities and resonance frequencies [42]. Researchers in [42] analyze summer and winter tires from the same production batch with three different tread depths. On a smooth surface similar to sand paper, tire wear led to a noise increase ranging from 0.5 dBA to 1.5 dBA. A rough surface would lead to a constant increase of noise with wear while a medium textured surface shows almost no tire influence on the TiRN emission.

Rubber Hardness

Shore Hardness has a positive correlation with TiRN emission [8]. The harder a tire, the more noise it will emit. A harder tire rubber seems to enhance TiRN generation mechanism especially at frequencies between 1000 Hz and 3000 Hz [43]. Stronger stick-slip motions are considered to be the reason for higher TiRN on tires with higher Shore values. Several studies show an average increase of TiRN between 1 dBA and 4 dBA per 10 Sh [8, 43, 44]. However, softer tire compound also results in increased local deformation. This can have two effects: Firstly, higher tire belt excitation may be observed due to increased vibrational overlay into the tire belt. Secondly, the soft rubber tread can reduce tire-road impacts and transmit less vibrations into the tire belt. As both effects are counteractive, the resulting effect on TiRN can not easily be determined [43].

A correction factor is presented in [45] to consider rubber hardness influence on near field TiRN measurements. As increasing temperature softens rubber, the reference tire rubber temperature is set to 20 °C. A normalization for rubber hardness deviation from an average value of 66 Sh is proposed for CPX testing in [45].

1.2.3 Road surface influence on tire-road noise

Micro-Roughness

Microtexture is generally considered to play a minor role in terms of TiRN, especially when no cornering or driving forces are applied to the tire. Although microtexture has a significant influence on road grip, various studies have shown no clear correlation between microtexture or road grip and TiRN [8, 45, 46]. Two noise emission mechanisms are mainly influenced by microtexture or road grip, which have very little effect under normal free-rolling conditions. On the one hand, stick-snap effects are stimulated more strongly on extremely smooth and sticky surfaces such as a polished steel surface, when the attraction force between rubber and road surface is increased. On the other hand, stick-slip noise is generated when tangential pressures build up during the tire runway and are suddenly released. An increased microtexture generally produces a higher road grip and consequently a stronger excitation of stick-slip noise. At the same time, the adhesion bond strength between the tire and the road could weaken, thus reducing stick-snap effects [8].

Macro- and mega-roughness

Macrotexture and the low wavelength range of megatexture have a significant influence on TiRN. While megatexture increases the noise level due to tire vibrations excitation, macrotexture has a wider range of influence, so that a same macrotexture level can have both positive and negative effects on TiRN. A higher macrotexture leads to higher tire vibrations and stronger low-frequency noise, but at the same time reduces higher-frequency air pumping noise due to a better ventilation of the tire-road contact [8]. TiRN increases in the low frequency range below 1000 Hz if the texture amplitudes level is high at

wavelengths between 10 mm and 50 mm. In the higher frequency range, noise level decreases with increasing texture amplitudes and wavelengths between 0.5 mm and 10 mm [47].

The influence of road surface texture on TiRN at speeds between 55 km/h and 100 km/h was studied using on-board sound intensity measurements in [48]. They showed that noise measurements are related to a specific transformation of the texture spectrum. This spectrum takes into account the driving speed of the vehicle to convert the spectrum from the wavelength domain to the frequency domain and then apply an A-weighting to model the frequency-dependent human hearing sensitivity.

Roughness scalar descriptors

The Mean Profile Depth (MPD), Mean Texture Depth (MTD) and Root Mean Square (RMS) introduced in the ISO 13743 standard are generally used to characterize macrotexture. MTD can be determined approximately from MPD using a transformation equation [49], whereby MPD computation is based on a more precise measurement method and should therefore be preferred. Nevertheless, comparative studies show that MTD can also be determined relatively precisely using the sand stain method and that MTD measurement results correlate very well with MPD [27, 50].

The impact of MPD on TiRN is described controversially in the literature. Different investigations indicate a positive correlation between an increasing TiRN level and a greater MPD or MTD [46, 51–53]. Particularly in the lower frequency range below 1000 Hz, an increased MPD leads to a higher TiRN level, whereas in the higher frequency range it has no influence or slighlty reduces noise emission [54]. However, individual studies also show that increasing the MPD does not necessarily lead to higher noise levels [8,55]. MPD influence is stronger on slick tires because TiRN is dominated by the road impact noise. For profiled tires, the tread impact generation mechanism greatly contributes to TiRN. A variation of MPD can therefore lead to very different effects for profiled tires. [8].

The influence of RMS on TiRN is investigated in [52]. Based on their measurements, increased noise levels could be measured with an increase of RMS.

15

However, this connection has not yet been sufficiently researched in the literature.

Surface shape orientation

Due to different results with regard to texture parameters such as MPD and RMS, which only represent the road surface roughness amplitude, additional parameters were developed to investigate the influence of surface shape orientation on TiRN. Surface texture can be distinguished between a negative texture (concave) characterized by plateaus with deep ravines and a positive texture (convex) characterized by "sharp" protruding points. Two parameters enable this distinction: the shape factor g and the profile skewness RSK. Rolled road surfaces tend to have concave textures and a high shape factor g from 60 % to 90 %, whereas scattered surfaces form convex textures with a low shape factor between 20 % and 60 %. Negative textures induce a negative profile skewness RSK and positive textures produce a positive profile skewness. Concave road types tend to be less noisy than convex road types with the same maximum grain diameter [56, 57]. As the penetration between road surface asperities and tire rubber is reduced, results in a smoother rolling over the road surface and therefore a reduced tire excitation [58].

A concave texture with a high shape factor can result in lower ventilation due to smaller cavities [58]. This can enhance air pumping contribution and have a negative effect on TiRN. Investigations have shown that the shape factor decreases over time as a result of stress and that the acoustic properties can deteriorate as a result [59].

While the shape factor influence on TiRN was largely investigated within the scope of the Sperenberg project [56], no direct investigation of the profile skewness influence on noise generation could be found in the literature. Nevertheless, it is widely agreed that these two parameters are important parameters with regard to acoustic properties of road surfaces.

Similar result using an angular description of the surface roughness maxima are presented in [60]. Road surfaces are quieter when angles formed by profile tips are blunt and angles between profile tips and the horizontal are flat. They also found that a narrower density of the roughness maxima had a positive effect on TiRN. The findings are equivalent to a concave pavement texture

with a high shape factor and negative profile shift. These results are confirmed in [61, 62], where the surface shape influence on tire vibration excitation is investigated, without referring to TiRN.

Acoustic absorption

Sound absorption affects TiRN in two ways. On the one hand, a high absorption capacity reduces the horn effect amplification efficiency, since the asphalt layer has less reflective properties [63, 64]. On the other hand, sound energy is attenuated on the propagation path from the noise source to the receiver [8, 65]. This also has a favorable effect on other contributors to vehicle noise, as the sound waves are reflected several times between the under-body and the roadway [8].

A good absorption capacity is achieved when high absorption maxima are obtained over a wide range of frequencies or at frequencies around 1000 Hz, where most of the generating mechanism of TiRN are concentrated [8]. Different coating types are investigated for their absorption properties in [66, 67]. They found that sound absorption of open-porous road surface was hardly noticeable in lower frequency ranges around 500 Hz. Even higher noise levels were measured, whereas in the medium to higher frequency range between 1000 Hz to 2000 Hz, noise absorption was very pronounced. It is assumed that due to a combination of rough surface and cavities formation, the resulting stronger stimulation of lower frequency noise compensates noise absorption. This means that noise absorption has a positive effect in the medium frequency range, whereas it is almost ineffective in the lower frequency range. The absorption spectrum is mainly determined by the void content, layer thickness, flow resistance and tortuosity [68].

Open-porous road surfaces are also susceptible to dirt due to their high void ratio. Due to soiling, particles gather in the road surface cavities, so that the height of the absorption coefficient peak is lowered. In addition, the clogged pores lead to lower permeability and higher flow resistance, resulting in a widening of the absorption peaks [69]. Dirt deposits also increase tortuosity, which has the same effect as increasing the thickness of the layer. The absorption maxima are consequently shifted to lower frequency ranges. The opposite effect is also possible if the dirt settles mainly on the ground. This reduces the

effective layer thickness, which results in a shift of the absorption maximum towards higher frequency ranges [69].

1.3 Aim of this work and work outline

The aim of this work is to understand and to quantify the road surface characteristics influence on rolling noise of passenger car tires. Measuring TiRN on different road surfaces and with various operating parameters will enable the extraction of relevant road surface parameters. Understanding and interpreting the statistical results will be useful to find the optimal road surface design to mitigate TiRN emission. Two serial tires and a ribbed-slick tire will be tested in order to isolate the road surface influence on global TiRN, but also on the sub-components that build it.

The research results are presented in four chapters. The introductory chapter shows the problem of traffic noise and its contribution to health problems. With the rise of electric vehicles and consequently the slow disappearance of combustion engines, tires become the main contributing source to traffic noise. Knowledge about how tire and road interact under different driving scenarios is essential to mitigate TiRN and will be summarized in a state of the art overview.

The second chapter presents fundamentals required to understand this work. First, the contribution of the main phenomena to TiRN will be presented. Then, an overview of the road surface descriptors used in this work will be provided, followed by a presentation of the ISO 10844 standard. This standard describes the characteristics of a test track used for tire and vehicle noise approval tests. In the end, the different statistical methods used to quantify the influence of road surface characteristics and operating parameters on TiRN are explained.

Several testing facilities, measurement procedures and simulation tools were used to analyze and understand road contribution to TiRN. They will be presented in chapter 3.

The final chapter 4 presents results of numerous road surface and TiRN measurements. First an analysis of the road surface characteristics summarizes and clusters road surface descriptors based on their correlation coefficients. A comparison between ISO 10844 test tracks and public roads measurements will

also be performed to see if standardized track are acoustically representative of public roads. The influence of operating parameters and road surface on TiRN will then be presented in the near field. A closer look will be given to one TiRN sub-component: groove resonance noise. This analysis will be supported with numerical results. Finally, the road surface influence on TiRN will be studied in the far field. Repeating coast-by measurements on a large amount of different roads enables the extraction of acoustic relevant road surface descriptors.

This research work is then concluded by a short summary and outlook on possible optimization measures.

2 Fundamentals

This chapter gives the relevant basics to understand this thesis. First an overview of the different mechanisms contributing to TiRN will be given. Then, the different possibilities to characterize a road surface will be detailed, followed by a summary of the ISO 10844 standard requirements. Finally, the statistical methods used in this thesis will be explained.

The acoustic theory will not be detailed here, as it can be found in many textbooks [70–72]. Detailed information about the structure and characteristics of passenger car tires can be found in [73–75].

2.1 Phenomena contributing to tire-road noise

An overview of TiRN contributing mechanisms is given in Tab. 2.1. Cells filled in gray denote the sub-phenomena that will be investigated through chapter 4. TiRN is generated mainly by vibrations of the tire structure and by fluctuations of the air pressure surrounding the tire.

2.1.1 Vibration noise

When a tire rolls on a road surface, vibrations continuously occur in the contact patch, propagate through the tire structure and are radiated outside the vehicle. These vibrations are mainly due to the road roughness, the impact of tread blocks at the leading edge of the tire and to the tread block release at the trailing edge. Friction noise can also occur under certain circumstances. The working principles of these vibration generation mechanisms will be further detailed in the following sections.

Table 2.1: Mechanisms contributing to TiRN (from [8])

Generation mechanism	Vibrational (structure-borne)	Impact mechanisms	Road impact
			Tread impact
			Running deflection
		Friction mechanisms	Stick-Slip
			Stick-Snap
	Aerodynamical (air-borne)	Air displacement mechanisms	Air turbulence
			Air pumping
			Groove resonance
			Helmholtz resonance
Amplification or reduction mechanisms			Horn effect
			Acoustic impedance effect
			Mechanical impedance effect
			Tire resonance

Road impact noise

Road surface characteristics presented later in section 2.2 are very important to describe road surface influence on road impact noise. Depending on the spatial distribution of the road surface roughness, the tire will be more or less excited by the road. A rough surface will mainly lead to tire radial vibrations, followed by belt and sidewall vibrations [8, 76, 77]. The frequency content of road impact noise depends linearly on the driving speed. The frequency of the road-induced excitation can be calculated directly by dividing the vehicle driving speed with the texture wavelength [8].

Tread impact and release noise

Another source of radial vibrations is the tread block impact at the leading edge of the tire. Tread impact frequencies depend on the impact sequence of the tread blocks and on the driving speed. If the tread pattern is not randomized, the tread impact frequency can be calculated by dividing the driving speed with the pitch (i.e. the distance between two tread blocks). While the tread blocks pass through the contact patch, they are submitted to radial, tangential and lateral forces, which they store as potential energy. When the tread block is released at the contact patch trailing edge, its rubber experiences a stress relaxation. The stored energy is then dissipated in the form of radial and tangential vibrations, which are also transmitted to the tire belt and sidewalls [8, 76].

Running deflection

The tire rotational symmetry is broken if the tire is exposed to a certain tire load. During the rolling process, the tire flattens out due to tire load. This running deflection leads to a radial deformation of the tire. The tire sidewalls are also pushed outwards. This leads to radial vibration excitation at the leading and trailing edges which are propagated to the belt along the circumference of the tire [8].

Stick-slip noise

The last vibration contributors to TiRN are friction noise. They are the consequence of friction properties of the tire-road contact. The first adhesion mechanism that influences TiRN is the stick-slip effect. If the maximum adhesion limit inside the contact patch is reached, the tread block swings back and can be deflected again. This process leads mainly to tread block tangential vibrations and leads to tonal noise in the frequency range of 1 kHz to 2 kHz [8, 76], commonly named "tire squeal". Not only tonal noise but also broadband frequency noise between 800 Hz and 4000 Hz are also attributed to stick-slip processes on the molecular level [75].

Stick-slip noise occurs mainly when driving with high tangential forces, as can be observed in fast acceleration, strong braking and cornering. This effect

23

will therefore be neglected in this study because the tire will always be driven straight and under free-rolling conditions.

Stick-snap noise

The stick-snap effect occurs when the tire adheres particularly well to the road surface which results from adhesion forces. This can occur especially when the tread and/or the road surface becomes sticky (e.g. winter tire compounds at summer temperatures or hot asphalt surfaces) [56]. High adhesion forces are created between the tire and the road surface, so that the tread elements in the contact surface stick to the road surface. When leaving the contact patch, the tread elements break away from the road and snap back to their undeformed shape. The stored potential energy during this process is here again dissipated into radial and tangential vibrations. This leads to high-frequency adhesion noise [8, 76].

However, there is usually no clean and very smooth road under normal rolling and ambient conditions. This effect can be mainly expected under test bench conditions with very clean and smooth drum surfaces [56], while this phenomenon should be less excited on real road surfaces with a higher macrotexture level. This effect will therefore be neglected in this work.

2.1.2 Aerodynamic noise

Aaerodynamic noise is due to a dynamic fluctuation of air pressure around the tire. This contribution to TiRN is related to tire rotation, the tread pattern geometry and the road surface void volume.

Air pumping

This effect is first presented in [78], where air is trapped between the tread elements cavities and the road at the contact patch leading edge. Due to tire flattening and tread blocks deformation, the air volume inside the tread pattern grooves is reduced compared to an undeformed tire, thus compressing

the enclosed air [8, 76]. The same phenomenon also applies for air cavities between the tire and the road surface cavities.

As the tire continues to roll, these cavities are released inside the contact patch and at the trailing edge, as the trapped air expands. To reduce this effect, good ventilation of the cavities and avoiding air pockets in the tread pattern are required to prevent air compression. This can be partially achieved by optimizing the tread pattern and creating open-porous road surfaces [77].

Groove resonance noise

When a profiled tire rolls over a road surface, standing waves can build up inside the groove network. This groove network forms a system of tube resonators, whose resonance frequencies depends directly on the groove geometry [8, 79]. Circumferential grooves opened at both ends correspond to half-wavelength resonators. The fundamental resonance frequency of a pipe with such boundary conditions can be computed according to Eq. 2.1. A groove closed at one end and opened at the other is called a quarter-wavelength resonator. Its fundamental resonance frequency is half the resonance frequency of a half-wavelength resonator (see Eq. 2.2).

$$f_{\frac{\lambda}{2}} = \frac{c_{sound}}{2 \cdot L_{groove}} \tag{2.1}$$

$$f_{\frac{\lambda}{4}} = \frac{c_{sound}}{4 \cdot L_{groove}} \tag{2.2}$$

where: $f_{\frac{\lambda}{2}}$ Groove resonance frequency for a pipe opened at both ends (half-wavelength resonator) [Hz]

$f_{\frac{\lambda}{4}}$ Resonance frequency for a pipe closed at one end and opened at the other (quarter-wavelength resonator) [Hz]

c_{sound} Speed of sound [m/s]

L_{groove} Groove length [m]

According to the literature, this effect mainly occurs on smooth road surfaces, where the pipe network geometry is better defined. This can not achieved on rough and open-porous surfaces, as additional openings are created between the tire and the road, leading to a reduction of groove resonance noise [79].

An improved ventilation of the tread pattern can also reduce groove resonance noise generation.

Helmholtz resonators

Helmholtz resonances can be described by a simplified acoustic mass-spring system, in which the air enclosed in the road surface cavities works as a spring and the compressed air between the tread blocks works as a vibrating mass [56]. By leaving or opening the cavity in the contact surface, the air volume in the coupled area increases and vibrations are stimulated. This effect can be illustrated by a bottle which is blown at the opening of its neck and thus produces a tone with a frequency dependent on the filling level [56]. If the tire-road contact surface is well ventilated – for example by a porous road surface or numerous longitudinal and transverse grooves in the tread pattern of the tire – this effect collapses [56].

2.1.3 Amplification and reduction mechanisms

The phenomena previously described deal with TiRN generation. Due to geometric and physical properties of the tire-road contact, TiRN can be also amplified or reduced.

Horn effect

Many of the TiRN contributing phenomena presented above are generated and/or radiated at the leading and trailing edges of the contact patch. This radiation will be enhanced by the horn geometry that the deformed tire builds on the road. This geometry is often modeled as an exponential horn and can be compared for example to the bell of a trumpet. This leads to an acoustic impedance adjustment and consequently to a directional amplification of the sound, which starts at about 300 Hz and reaches a maximum between 1500 Hz and 2000 Hz [8, 76].

Acoustic and mechanical impedance effects

Physical and mechanical properties of the road surface also affect TiRN. Mechanical impedance is a measure of the motion resistance of a structure when subjected to a harmonic force. The influence of mechanical impedance on TiRN was studied in [80] and will not be considered in this work. Acoustic impedance describes how strongly a system opposes to an acoustic flow resulting from an applied acoustic pressure. In this work, the acoustic impedance of the road surface will be accounted for by measuring the absorption spectrum of the road surface with an impedance tube (see section 2.2.1). While the sound wave is propagated from the tire to the receiver, it might be reflected several times on the road surface. Depending upon the road surface absorption characteristics, this might lead to a further reduction of TiRN. Open-porous asphalts tend to have a high absorption coefficient and are therefore used to avoid TiRN amplification by reducing radiation efficiency of the horn effect [63].

Tire resonances

In the literature, two different forms of tire resonances are distinguished: resonances caused by vibrations of the tire belt and resonances of the tire cavity. As already described in the previous sections, these resonances are caused by mechanical excitation mechanisms in the contact patch. In general, several belt resonances are very efficient at radiating noise in the frequency range from 700 Hz to 1300 Hz [8]. This frequency is critical because many TiRN generating phenomenon lie in the same frequency range (e.g. road impact, tread impact, and groove resonance noise). If these phenomena lie in the same frequency domain as tire resonances, their amplitude may be amplified, resulting in a higher TiRN. Just like air inside the tread pattern grooves, air inside the tire can also resonate. An extensive study of tire cavity resonance is presented in [81]. Tire cavity noise is rather low-frequent (below 300 Hz for the fundamental resonance frequency) and is therefore of great importance for vehicle interior noise but less for external TiRN [82].

2.2   Road surface characterization
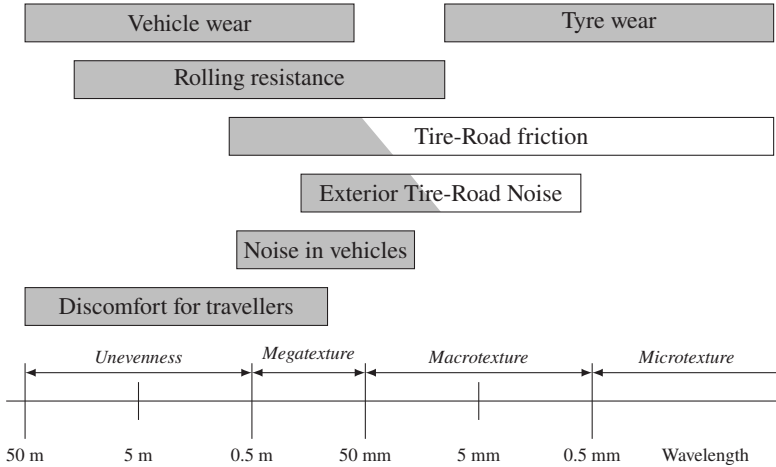
Figure 2.1: Texture wavelength's expected consequences on the vehicle-road interaction. A bright background indicates a favorable effect of the texture in that area, while a darker background indicates an undesirable effect (from [83])

In order to examine their acoustic properties, road pavements can be distinguished in terms of texture spectrum, surface shape and void content.

In road construction, texture is typically characterized by frequency-analytical methods. Decomposition of the texture profile allows to assign an amplitude to each texture wavelength. The resulting wavelength-amplitude spectrum makes it easier to identify dominant texture areas with frequently occurring texture wavelengths and to draw conclusions about their influence on the acoustic or friction properties of the tire. The entire texture spectrum is defined up to a limit wavelength of 500 mm, whereby unevenness describe a texture wavelength above 500 mm [83] (see Fig. 2.1).

Microtexture designates a wavelength range up to 0.5 mm and mainly describes the intrinsic roughness of the stones in contact with tire rubber. Macrotexture describes the surface roughness from wavelengths between 0.5 mm and 50 mm. As shown in Fig. 2.1, macrotexture can have both positive and negative effects on TiRN.

While microtexture or macrotexture can have both negative and positive effects on TiRN, megatexture influence on TiRN is clear. Due to large wavelengths in the same order of magnitude as the tire-road interface, megatexture generates relatively strong mechanical excitation of the tire belt and a relatively high noise level. It not only has an influence on exterior noise, but also plays a decisive role in vehicle interior noise. The wavelengths corresponding to megatexture vary between 50 mm and 500 mm. Megatexture is generally an unwanted characteristic and results from pavement aging (potholes, ruts, etc.).

2.2.1 Acoustic absorption

The parameters mentioned so far refer to road surface acoustic properties in terms of texture spectrum. With regard to open-porous pavements, road surfaces can also be distinguished by their absorption properties. Acoustic absorption in road construction is mainly found in open-porous road layers, where good absorbing properties are achieved by a favorable mix composition and omission of fine grain fractions. The decisive parameter for the sound absorption capacity of a road surface is the sound absorption coefficient α, which represents the relative share of the sound energy which is not reflected but absorbed by the road surface.

At an absorption coefficient of one, the total sound energy that hits the surface is "swallowed", at a value of zero it is completely reflected [57]. However, the sound absorption coefficient of open-porous surface does not have the same value over the entire frequency range in which TiRN is effective. It is frequency-dependent and only achieves high values in certain narrow frequency ranges [57]. The absorption coefficient frequency response is characterized by pronounced maxima, which can vary in the frequency range relevant for TiRN from 200 Hz to 4000 Hz depending on the condition of the road surface.

Only low-absorbing road surfaces will be considered in this work, due to the limitations of the in-situ acoustic impedance measurements (see section 3.1.2). This corresponds to road surfaces with an absorption coefficient below 15% for each third-octave band.

2.2.2 Scalar roughness descriptors

From now on, the road surface height profile will be denoted by $Z(x)$, where x depicts the longitudinal traveling direction of the car. Road surface measurements are performed over a length L.

Mean profile septh

The mean profile depth (MPD) is computed according to ISO 13473-1 based on 100 mm long of road surface profile measurements [49]. The long-wave portions must be first eliminated by high-pass filtering or by suppressing the baseline slope [84]. Each line measurement is then divided in two parts and the maximum roughness levels of each part is extracted (see Fig. 2.2). The MPD is then computed according to Eq. 2.3.

$$\text{MPD} = \frac{Z_{max_1} + Z_{max_2}}{2} - \overline{Z} \qquad (2.3)$$

where: MPD Mean profile depth [mm]

$\quad\quad\quad Z_{max_1}$ Peak level of the first baseline half [mm]

$\quad\quad\quad Z_{max_2}$ Peak level of the second baseline half [mm]

$\quad\quad\quad \overline{Z}$ Average roughness level [mm]

The MPD replaces the originally used mean texture depth MTD, which is determined by the classic volumetric method ("sand patch method", see section 2.3.3). The MTD describes the distance between the examined surface and a plane passing through the peaks of the three highest points of this surface [84]. Due to the manual execution of the test, results can however be strongly influenced by the person performing the measurement. As optical methods are increasingly used in practice due to their higher accuracy, the MPD is the decisive parameter to describe road surface roughness for acoustic purposes [84].
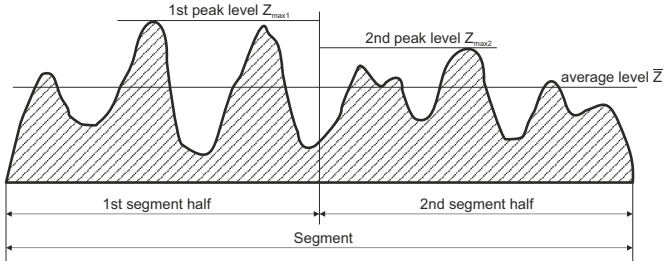
Figure 2.2: Reference lines to compute the MPD according to ISO 13473-1 (from [49])

Root mean square

The root mean square (RMS) of the profile describes the standard deviation of the profile height distribution [84]. In contrast to the arithmetic mean, this parameter gives greater weight to larger roughness values of the profile, so that pronounced local peaks have a stronger influence than smaller ones. Planar surfaces with locally occurring roughness elements, which may possibly lead to a stronger vibration excitation of the tire, can be better identified with this texture parameter in comparison to the arithmetic mean [85]. The RMS value is calculated according to Eq. 2.4:

$$\text{RMS} = \sqrt{\frac{1}{L} \int_0^L Z^2(x)\,dx} \tag{2.4}$$

Skewness

Up to now, only the roughness amplitude was described using the MPD and the RMS. These parameters can not describe whether roughness amplitude is oriented towards the tire or not. A texture parameter that addresses this problem is the skewness RSK. It is a measure of the asymmetry of the probability density function of the surface roughness $P(Z)$. It indicates whether the roughness

31

profile is mainly shaped by peaks upwards (positive profile skew) or downwards (negative profile skew). It is dimensionless and is calculated with Eq. 2.5 [84].

$$RSK = \frac{1}{RMS^3} \left[\frac{1}{L} \int_0^L Z^3(x)dx \right] \tag{2.5}$$

Figure 2.3 illustrates the influence of the skewness sign on the road surface profile roughness. The second profile has almost the same number of peaks and valleys. The height and frequency of peaks is therefore approximately equal to the height and frequency of valleys. This coincides with a symmetric probability density function of the surface roughness and therefore to a skewness of zero. Both the upper and lower profiles in Fig.2.3 show an asymmetric distribution of the height profile. The upper profile has a plateau shape with deep and narrow cavities, which corresponds to a negative-oriented surface (i.e. to a negative skewness). The lower profile, in contrast, has extreme profile tips and thus represents a positive-oriented profile with a positive skewness.

(a) Texture roughness   (b) Distribution functions
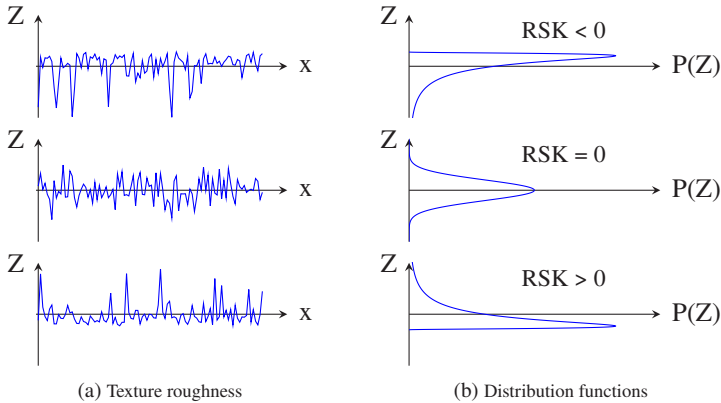
Figure 2.3: Profile skewness as a function of the profile roughness according to ISO 13473-2

Kurtosis

The kurtosis RKU is dimensionless and describes the flatness of the profile probability density function. It measures the influence of the outer edges of a distribution and measures how "balanced" or "pronounced" the distribution is in comparison to a normal distribution. For example, a distribution with "long wide drags" has a high RKU value [84]. The kurtosis is calculated using Eq.2.6:

$$RKU = \frac{1}{RMS^4} \left[\frac{1}{L} \int_0^L Z^4(x)dx \right] \tag{2.6}$$

With a normally distributed roughness profile, the kurtosis is equal to three. If the RKU value is greater than three, this means that sharp, pronounced peaks and valleys are present in the roughness profile. The flattened profile tips and troughs correspond to a value of less than three [86].

(a) Texture roughness　　(b) Distribution function
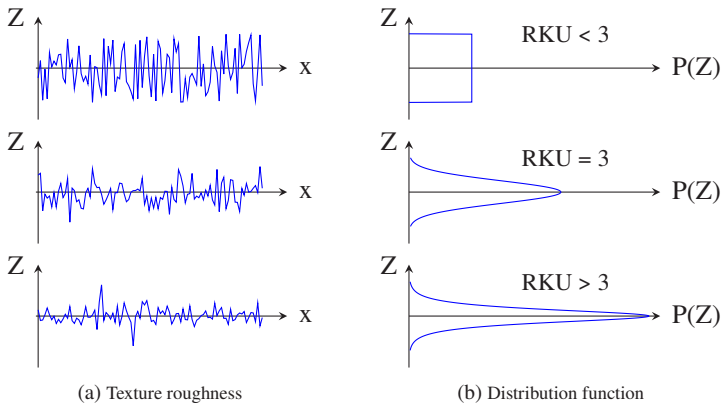
Figure 2.4: Profile kurtosis as a function of profile roughness according to ISO 13473-2

Shape Factor

As the skewness RSK, the shape factor g describes texture orientation. Concave ("plateau with pronounced cavities") and and convex textures ("plateau with pronounced peaks") are distinguished. The shape factor can be determined

by using the complementary cumulative distribution function, also known as the Abbott-Firestone curve. To build the Abbott-Firestone curve (see section 2.2.3), an imaginary cutting line is passed through the measured profile from the highest to the lowest roughness value. For each cutting line, the number of points above the cutting line is divided by the total number of points building the road surface profile. The shape factor g is equal to the material ratio at a roughness of half the roughness amplitude range [56]. High g-values tend to indicate concave textures, whereas low g-values tend to be convex [68]. A strong negative correlation is expected between g and RSK.

(a) Texture roughness   (b) Abbott curve
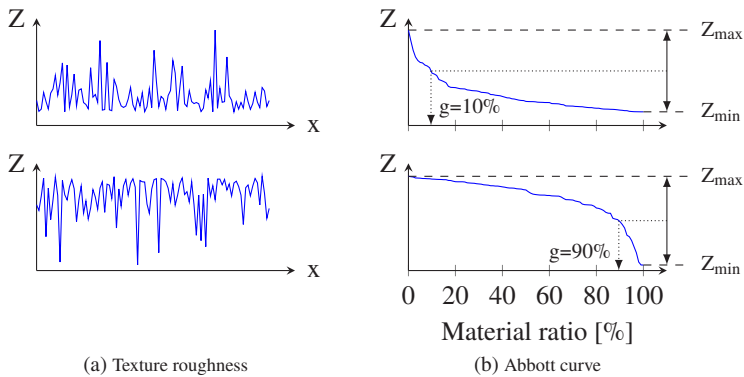
Figure 2.5: Illustration of the shape factor g for a convex profile (upper part) and for a concave profile (lower part)

2.2.3 Roughness non-scalar descriptors

Roughness amplitude band spectrum

The roughness amplitude band spectrum depicts the distribution of the road surface roughness amplitude along the wavelength domain. Three methods are proposed in ISO 13473-4 to compute it. For the road surface measurements performed in this work, the second method is used. Outliers are first removed from the profile, then a digital bandpass filter with constant bandwidth is

applied at the wavelengths of interest. For each wavelength λ, the roughness amplitude band spectrum Ltx_λ is computed according to Eq. 2.7.

$$\text{Ltx}_\lambda = 20 \cdot \log\left(\frac{\tilde{z}_\lambda}{z_{ref}}\right) \tag{2.7}$$

where: $\quad \text{Ltx}_\lambda \qquad\qquad$ Roughness amplitude band spectrum [dB]

$\qquad\qquad z_{ref} = 10^{-6}\ m \quad$ Reference value

$\qquad\qquad \tilde{z}_\lambda \qquad\qquad\quad$ RMS value of the filtered profile [m]

An example of the roughness amplitude band spectrum can be seen in Fig. 2.7a.

Abbott-Firestone curve

The Abbott-Firestone curve has already been shortly presented in section 2.2.2 and was first described by Abbott and Firestone in [87]. It can mathematically be described by the probability that the roughness profile Z is greater than or equal to a certain roughness level z (see Eq. 2.8).

$$F_Z(z) = P(Z \geqslant z) \tag{2.8}$$

The Abbott-Firestone curve is closely related to the probability density function (see Fig. 2.3b) and can be seen as the area under the probability density function from minus infinity to z.

2.3 The ISO 10844 standard

Test tracks built according to the ISO 10844 standard are used to measure vehicle noise and TiRN. According to the standard, the surface design should produce consistent TiRN levels under a wide range of operating conditions, minimize inter-site variation, provide minor absorption of the vehicle noise source and be consistent with road-building practice [88]. This section resumes the characteristics of the 2014 version of the ISO 10844 standard that are relevant for this work. A very exhaustive and well depicted overview of the ISO 10844 standard is given in [89, 90].

2.3.1 Road surface requirements

The required geometry for standardized ISO 10844 test tracks is depicted in Fig. 2.6. It consists of two surfaces: a driving lane and a propagation area. The AA' line depicts the beginning of the propagation area and the BB' line its end. The microphones should be put on the PP' line at a distance of 7.5 m from the CC' line. Around the test track center, a circular surface with a 50 m radius must be free of large reflective objects such as buildings, trees or fences. The track must be built, so that the propagation area is on the same plane as the driving lane or at most 20 mm below it. The transverse and longitudinal slope should be chosen within the tolerances to enable water drainage outside of the propagation area.

The maximal grain sieve size for ISO 10844 asphalt mixture is 8 mm, although tolerances between 6.3 mm and 10 mm are allowed. The sieves used for the asphalt mix should follow a specific sieving curve. Polymer modified bitumen can be used for the asphalt mix but no elastic materials such as rubber or polyurethane.

The requirements for ISO 10844 test tracks are summarized in Table 2.2. The driving lane and the propagation area must have homogeneous results regarding their physical and geometrical characteristics (e.g. geometry, unevenness, texture roughness and acoustic absorption). This implies that the average measurement result as well as 80% of the measurements should meet the standard requirements. Unevenness should be measured according to EN 13036-7 using a 3-meter straightedge and a gap gauge. The MPD of the driving

lane should be computed from laser profile measurements performed on the wheel tracks according to ISO 13473-1. The acoustic absorption spectrum in third-octave bands should be measured in-situ using an impedance tube and computed according to ISO 13472-2.
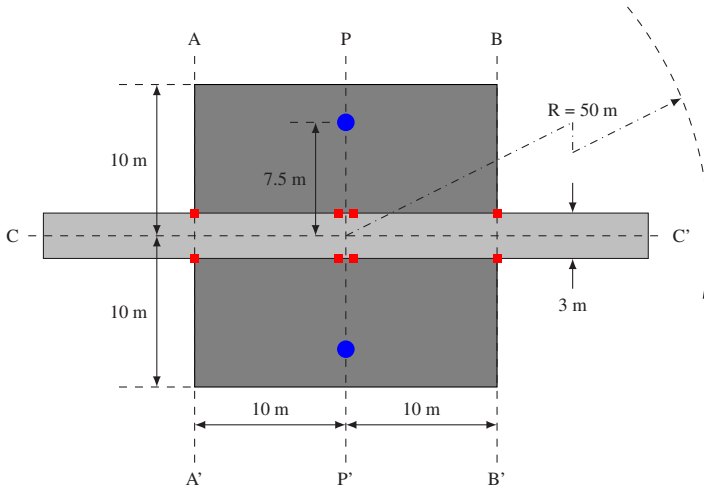
Figure 2.6: Schematic representation of an ISO 10844 test track (according to [91]). The red squares illustrate the photoelectric sensors used to determine the vehicle's position and speed. The blue points depict the microphones.

2.3.2 Expected pass-by noise level difference from texture level variation of the road surface

The Expected pass-by noise level difference from texture level variation of the road surface (END_T) was developed during the SILVIA project [92]. It aims at quantifying the road surface texture influence on pass-by noise compared to a reference surface. This characteristic is not a normative part of the standard. It is computed according to ISO 13472-3 by comparing the texture third-octave band spectrum of the test track with a reference test track and by using a reference TiRN spectrum (see Fig. 2.7).

Table 2.2: Requirements for a standardized ISO 10844 test track. The gray cells depicts the characteristics, where the focus will be put on in this work.

Test track property	Construction approval		Periodical inspection	
	Driving lane	Propagation area	Driving lane	Propagation area
Sieving curve	Meet requirements	n.a.	n.a.	n.a.
Step	$\leqslant$ 20 and $\geqslant$ 0 mm	n.a.	n.a.	n.a.
Longitudinal slope	$\leqslant$ 0.5 %	n.a	n.a	n.a
Transverse slope	$\leqslant$ 1 %	$\leqslant$ 2 %	n.a	n.a
Longitudinal unevenness	$\leqslant$ 2 mm	$\leqslant$ 20 mm	$\leqslant$ 5 mm	n.a
Transverse unevenness	$\leqslant$ 3 mm	$\leqslant$ 20 mm	$\leqslant$ 5 mm	n.a
Texture (MPD)	0.5 ± 2 mm	n.a	0.5 ± 2 mm	n.a
Absorption	$\leqslant$ 8 %	$\leqslant$ 10 %	$\leqslant$ 8 %	n.a
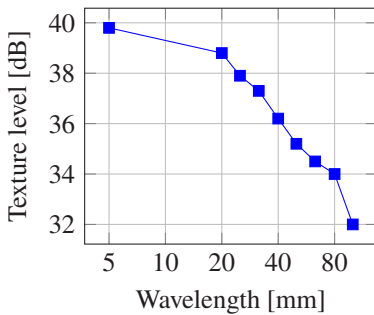
(a) Reference texture level
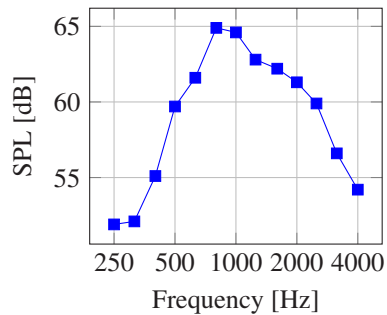
(b) Reference SPL

Figure 2.7: Reference texture and sound level spectra for the computation of END_T according to ISO 10844:2014

END_T can be computed with Eq. 2.9.

$$END_T = 10 \cdot \log(A/B) - C$$

$$A = \sum_{i=1}^{13} 10^{L_{mi} + b_i \cdot \Delta Ltx_\lambda / 10}$$

$$\tag{2.9}$$

$$B = \sum_{i=1}^{13} 10^{L_{mi}/10}$$

$$C = 0.25 \cdot \Delta Ltx_{5\ mm}$$

where: L_{mi} Reference noise levels given in the ISO 10844 standard [dB]

         b_i Factors fixed in the ISO 10844 standard [-]

         ΔLtx_λ Roughness amplitude band spectrum difference between the reference track and the measured one at the wavelength λ [dB]

2.3.3 Standard evolution

Differences between 1994 and 2011

The 2011 version is a major revision of the 1994 version. The major improvements are summarized in Table 2.3 and are enabled due to the improvement of measuring techniques. In the 1994 version, the texture specification was done using the MTD, which was measured according to the sand patch method. To avoid operator influence and therefore have a more objective characteristic value, the specification is now to be made using the MPD. To improve test track resistance to wear and higher temperatures, it is now allowed to use polymer modified bitumen inside the asphalt mix. A reduced wear should also lead to an improved stability of acoustic properties over time [90]. The acoustic absorption specification also reduces the variance between the test sites, as a track could fulfill the void content specification but not the acoustic absorption requirements.

Table 2.3: Technical evolution between ISO 10844:1994 and ISO 10844:2011 (from [90])

ISO 10844: 1994	ISO 10844: 2011
Evenness required but not defined	Unevenness specification included and test method detailed
Straight bitumen	Allowance of polymer modified bitumen
Texture specification using the volumetric method (sand patch method)	Texture specification using laser profilometers
Texture specification one-sided (lower limit only)	Texture specification using target and tolerance
Sieving curve informative	Sieving curve normative
Acoustic absorption measured by void content or using core samples with a limit of 10 % in average over band	Acoustic absorption measured in-situ with specification of 8 % in each third-octave band

Differences between 2011 and 2014

The 2014 version is a minor revision of the 2011 version with mainly editorial corrections.

2.4 Statistics

Several statistical tests and methods are used in this work. Necessary background to understand their application on TiRN measurements is presented in this section. For a mathematical approach, please refer to [93] for the functional principal component analysis (FPCA), to [94, 95] for the multiple linear regression and to [96, 97] for further information about adaptive shrinkage techniques and the double lasso shrinkage technique. An overview of regression shrinkage techniques is given in [98].

Different wording is used in the statistical literature. In this work, the word "explanatory variable" will be preferred to "independent variable" to avoid confusion with the "dependent variable". The latter will also be denoted as "outcome".

2.4.1 Functional principal component analysis

Functional principal component analysis (FPCA) is the application of principal component analysis (PCA) to functional data. Functional data analysis consists in analyzing information coming from multidimensional data such as curves or surfaces. These data can vary over one or multiple variables such as time, frequency, wavelength. First, the functional data $X(t)$ is projected to a base of independent functions $\psi_n(t)$. Generally, a Fourier basis is used for periodical and stable data while a spline basis is used for non-periodical data [93]. In this work, non-periodical functional data are studied (roughness spectrum and Abbott curve). Therefore, linear penalized B-spline functions are used as basis functions. Penalized B-spline functions use an additional penalty function to force smoothness and thus reduce overfitting [99]. Model selection (i.e. the number of basis functions N chosen) is realized by minimizing the Bayesian information criterion (BIC). An estimation of the original functional data $\widehat{X_N}(t)$ is obtained:

$$\widehat{\chi_N}(t) = \sum_{n=1}^{N} c_n \cdot \psi_n(t) \tag{2.10}$$

where: $\widehat{\chi_N}(t)$ Estimation of the functional data after projection

    c_n Basis functions coefficients

    $\psi_n(t)$ Basis functions

The main mode of variations of the fitted functional data $\widehat{X_N}(t)$ can now be studied. This method can be compared to structural modal analysis, where structure vibration can be computed – under several assumptions – as the superimposition of its eigenmode contribution. In FPCA, the counterpart of the eigenvalue is the functional principal component (FPC) and the equivalent of the eigenvector is the eigenfunction $\phi_k(t)$. The main difference with modal analysis is that FPCA analyses variation along the mean fitted functional data $\overline{\widehat{X_N}}(t)$.

$$\widehat{\chi_K}(t) = \overline{\widehat{\chi_N}}(t) + \sum_{k=1}^{K} \text{FPC}_k \cdot \phi_k(t) \tag{2.11}$$

where: $\widehat{\chi_K}(t)$ Estimated functional data

    $\overline{\widehat{\chi_N}}(t)$ Average value of the projected functional data

    FPC_k k^{th} Functional principal component

    ϕ_k k^{th} eigenfunction

For e.g. a texture amplitude spectrum, the eigenfunctions ϕ_k are used to decompose the roughness amplitude-wavelength dependency into main modes of variation in a consistent way for all road surfaces. It is therefore important to first understand the physical meaning of each eigenfunction. This will be presented in section 4.1.1 and 4.1.2. The sign and value of each FPC are then used to quantify the variance between the texture spectra of different road surfaces. To understand the contribution of each eigenfunction to the variation in the functional data, the following function can be used

$$\widehat{\chi_K}(t) + \eta \cdot \phi_k(t) \tag{2.12}$$

where η corresponds to the FPC and varies between a fixed positive and a negative value. To best interpret the influence of the sign of the FPC on the non-scalar roughness descriptors (see section 4.1.1), the values chosen for η are -0.2 and 0.2.

2.4.2 Multiple linear regression

The base used for the statistical analysis in this work is multiple linear regression. Multiple linear regression is used to predict an outcome Y based upon several explanatory variables X_j.

$$Y = \beta_0 + \sum_{j=1}^{p} \beta_j X_j + \epsilon \tag{2.13}$$

where: Y Predicted outcome
        X_i Explanatory variables
        β_i Regression coefficients
        ϵ Error term, also known as residuals

The regression coefficients β_j are computed according to the ordinary least square method [94]. Several assumptions are made for the multiple linear regression [94]:

- The relationship between the predicted outcome Y and the explanatory variables X is linear

- The correlation between the explanatory variables is low

- The observations of Y are done randomly and independently

- The residuals ϵ follow a normal distribution

2.4.3 Variable selection using shrinkage technique

To improve model interpretability and its prediction accuracy, only the most significant variables must be identified and kept inside the regression model. This can be done using shrinkage techniques. While the ordinary least square methods minimizes the squared sum of the residuals, regularization or shrinkage technique add a penalty parameter to the optimization function. One of these shrinkage techniques is known as the lasso shrinkage and uses a L1 penalty, which refers to the first norm of the regression coefficients $||\beta_j||_1$.

The best generalized regression model is obtained by computing the following target function:

$$\min_{\beta} \left(\epsilon^2 + s \sum_{j=1}^{p} |\beta_j| \right) \qquad (2.14)$$

where: ϵ Residuals

s Shrinkage or penalization coefficient

β_i Regression coefficients

The choice of the penalization coefficient s can be done for example by minimizing the cross-validation error or the BIC. If the regression coefficient of one variable β is shrunk to zero, this parameter is set out from the model and is considered as non-significant.

The double lasso, also known as relaxed lasso is extensively presented in [96] and consists of two steps, in order to separate the selection from the shrinkage steps. First, the double lasso performs variable selection with an initial lasso model. The retained explanatory variables are then used as input in a second lasso model [100].

The double lasso offers several benefits compared to the standard lasso estimation. It namely tends to select a smaller number of parameters without compromising the prediction accuracy, which facilitates the results interpretation. The prediction accuracy is better if the signal-to-noise ratio is high [96].

2.4.4 Statistical metrics and other methods

Several statistical metrics are used in this work in order to quantify the quality of fit of the statistical analysis.

Coefficient of determination

The coefficient of determination R^2 is the most commonly used metric to measure the predictive accuracy of regression models [95]. R^2 quantifies how much variation in the output variable can be predicted by the variation in the

explanatory variables. R^2 varies between 0 (no prediction) and 1 (perfect prediction)

$$R^2 = 1 - \frac{\text{RSS}}{\text{TSS}} = 1 - \frac{\sum \epsilon}{\sum (Y - \overline{Y})^2} \qquad (2.15)$$

where: R^2 Coefficient of determination

           RSS   Residuals sum of squares

           TSS   Total sum of squares

           ϵ Residuals

           Y Predicted outcome

           $\overline{Y}$ Average value of the predicted outcome

However, R^2 should not be the only metric to analyze the regression quality of fit. Adding more and more explanatory variables to the model will lead to a constant increase of the coefficient of determination. In the end, the model will tend to overfit the data [95]. Such a problem can be solved by selecting an appropriate number of explanatory variables (see section 2.4.3) or by using cross-validation methods.

Bayesian information criterion

The Bayesian information criterion (BIC) is used to perform model selection. BIC is close to the Akaike information criterion (AIC), which is another commonly used criterion for model selection [101]. Both information criteria can be used to compare different models to determine the best-fitting one, while at the same time penalizing model complexity. This is generally done by choosing the model with the smallest BIC [102]. BIC tends to penalize complex models more than AIC, resulting in the selection of simpler models [101]. BIC is computed according to the following equation:

$$\text{BIC} = -2 \log \widehat{L} + d \ln(n) \qquad (2.16)$$

where: $\widehat{L}$ Maximized value of the likelihood function of the model

           d Number of parameters estimated by the model

           n Number of observations

k-fold cross-validation

Overfitting is a problem to be avoided in statistical predictive modeling. When too much explanatory variables are used to predict an outcome, the model becomes more complex and tend to describe random error and statistical noise instead of the underlying physical relationships.

Overfitting can be detected by using k-fold cross-validation. k-fold cross-validation splits the data set in k equally sized parts. One set is kept to test the model which was trained with the remained $k - 1$ parts. This analysis is then repeated until all parts were used as a testing set. A typical observation of overfitting is when the training error is low and the coefficient of determination is close to one while the testing results show opposite values (high testing error and low R^2).

Variance inflation factor

The variance inflation factor (VIF) is used to control one of the assumptions of the multiple linear regression. The VIF is computed for each explanatory variable in the model and describes the degree of collinearity among the explanatory variables:

$$\text{VIF}_i = \frac{1}{1 - R_i^2} \tag{2.17}$$

where: VIF_i Variance inflation factor between the explanatory variable X_i and the other explanatory variables

R_i^2 Coefficient of determination between the explanatory variable X_i and the other explanatory variables

Multicollinearity inside a multiple linear regression must be avoided, as it can have an **influence** on the estimation of the regression coefficients β_i [94]. As a rule of thumb, a VIF between 3 and 5 depicts a strong multicollinearity among the explanatory variables [95, 103]. If the VIF exceeds 10, there is an excessive collinearity between the explanatory variables.

Correlation coefficients

The Pearson correlation coefficient ρ and the Spearman's rank correlation coefficient r_s are used in this work to assess whether two variables are correlated. While a linear relationship between two variables is checked using the Pearson's correlation coefficient, the Spearman's rank correlation coefficient assesses how well a monotonic function can describe the relationship between two variables [104]. Both coefficients have values between -1 (perfect negative correlation) and +1 (perfect positive correlation) and are computed according to Eq. 2.18

$$\rho = \frac{\text{cov}(x, y)}{\sigma_x \cdot \sigma_y} \quad ; \quad r_s = \frac{\text{cov}(rg_x, rg_y)}{\sigma_{rg_x} \cdot \sigma_{rg_y}} \tag{2.18}$$

where: ρ Pearson correlation coefficient

r_s Spearman's rank correlation coefficient

(x, y) Variables

(rg_x, rg_y) Ranked variables

$\text{cov}()$ Covariance

(σ_x, σ_y) Variables standard deviation

3 Methods

3.1 Measurement procedures

3.1.1 Tire-road noise measurements

The inner drum test bench

The inner drum test bench of the Institute of Vehicle System Technology at the KIT consists of a drum with an inner diameter of 3.8 m and a rigid wheel carrying system (see Fig. 3.1). The testing facility was further developed to study the friction behavior of tires on different asphalt and concrete surfaces, which can be changed at will [105]. Other road conditions such as snow, ice or a defined water film [106–108] can be studied. The inner drum is also used for acoustic measurements [81, 109, 110] and was optimized to reduce the background noise coming from the test rig [109].

Using the wheel carrying system and its hydraulic motors, all operating parameters (driving speed, tire load, slip and camber angles) can be regulated independently and continuously. Measurements performed for this dissertation are realized in free-rolling conditions with camber and slip angles fixed to zero. Tire load is measured using a Kistler measuring hub type Z 11957. Road surface temperature is measured using an infrared thermometer optris CTlaser LTF.

Five free-field microphones MM210 were used for acoustic measurements on the test rig. The microphones oriented towards the tire sidewall are positioned according to the close-proximity-method (CPX) [113]. Due to drum curvature, microphones at the leading and the trailing edges had to be repositioned closer to the tire (see Fig. 3.2). The sampling frequency is set to 44 100 Hz. Measurements are realized using a LabVIEW program on a PXIe-4497 acqui-
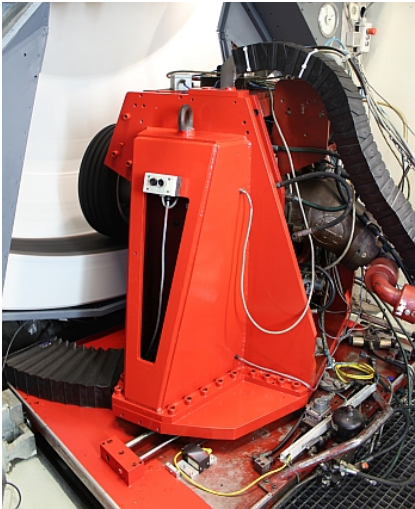
Figure 3.1: Inner drum test bench and its wheel carrying system (from [111])

(a) Side view

(b) Top view
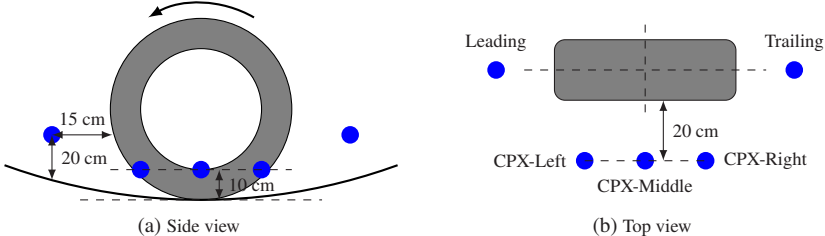
Figure 3.2: Microphone positions on the inner drum test bench. The thick arrow on the left part describes the standard direction of rotation (from [112]).

sition module and produce time signals in ".tdms" format. These data are then imported and exploited using Matlab R2018a. The measurement procedure is identical for all measurements on the inner drum test bench. The tire is warmed up for 20 minutes at the desired tire load using a speed of 90 km/h. After warm-up, inflation pressure is adjusted to 2.5 bar. The driving speed is incrementally decreased from 120 km/h down to 30 km/h using 2.5 km/h steps. Each measurement lasts ten seconds.

Coast-by measurements

To study road surface influence on TiRN, coast-by measurements were performed on standardized ISO 10844 test tracks [88] and on public roads. Coastby measurements were performed following the UNECE R117 regulation [9]. The car is to be driven in a straight line over the measuring section (AA' to BB') in such a way that the vehicle median longitudinal plane is as close as possible to the CC' line (see Fig. 2.6 for the denomination). Two microphones are positioned at 7.5 m from the CC' line at a height of 1.2 m. The car passing noise must be measured while the test car is on the measuring surface. The gearbox must be switched to neutral position and the motor must be turned off before the car front crosses the AA' line [9].

The test vehicle is a Mercedes W220. The car speed at the PP' line is measured by two photoelectric sensors spaced one meter apart. Measurements are repeated until four valid measurements are done on both vehicle sides at speeds between 70 km/h and 80 km/h, and between 80 km/h and 90 km/h. Measurements are performed according to the requirements from the R117 regulation, except for the following two points:

- Inflation pressure is set to 2.5 bar in warm conditions. This enables a comparison with the measurements on the inner drum test bench, which were done with the same inflation pressure. Such an inflation pressure is also common for passenger car tires and will be more representative of standard operating conditions.

- Only one microphone is used to make measurements on public roads easier. Measurements are therefore repeated in both driving directions in order to assess both car sides.

3.1.2 Road surface measurements

Profile roughness measurements

The spectral and scalar road surface roughness descriptors presented in section 2.2.2 and 2.2.3 are computed from measurements performed with a laser profilometer according to ISO 13473-3 [114].

The laser sensor is fixed on a portal beam and scans the road surface roughness using a laser triangulation system. The beam enables a measurement length up to one meter (see Fig. 3.3a). The sensor used for the road surface profile measurement is a MicroEpsilon ILD 2300-50 which has a measurement range of 50 mm and a vertical resolution of 0.8 μm. The laser sensor moves forward with a constant speed of 19.5 mm/s and a sampling frequency of 5000 Hz.

For field measurements, road surface roughness is measured using 16 lines, equally distributed between the left and right tire driving lanes and distributed along the longitudinal direction of the test spot. Road surfaces of the inner drum test rig are scanned completely over its circumference and width.

In-situ acoustic impedance measurements

The road surface absorption coefficient is measured and computed according to the ISO 13471-2 standard, using an impedance tube in-situ. The major advantage of this method is that core samples extraction is no longer required. However, only low-absorbing road surfaces up to an absorption coefficient of 15% can be measured with this method [115].

The impedance tube is positioned vertically on the road surface and hermetically sealed using sealant material (see Fig. 3.3b). A plane acoustic wave is then generated inside the tube and the sound pressure level is measured by two microphones. By computing the transfer function between the two microphones, it is possible to compute the road surface absorption coefficient [116].

The impedance tube used in this study is an AED 1000 - AcoustiTube®. For the field measurement, three measurements are performed on the tire driving lanes near the PP' line. For the different surfaces used in laboratory conditions, the eight segments fixed inside the inner drum test bench are also measured with the impedance tube.

Grip measurements

Skid resistance can be measured with a skid resistance tester (SRT), also known as British pendulum (see Fig. 3.3c) [117]. This pendulum measures the kinetic energy loss of a rubber body sliding over the road surface. Temperature

influence on pendulum values can be corrected in accordance with DIN EN 13036-4 [118]. Measurements are performed inside the tire driving lanes to capture the microtexture level that the tire sees while driving pass the microphone. As for the impedance measurements, three spots are measured near the microphone line during field measurements while eight spots are measured inside the inner drum test bench.

| (a) | (b) | (c) |
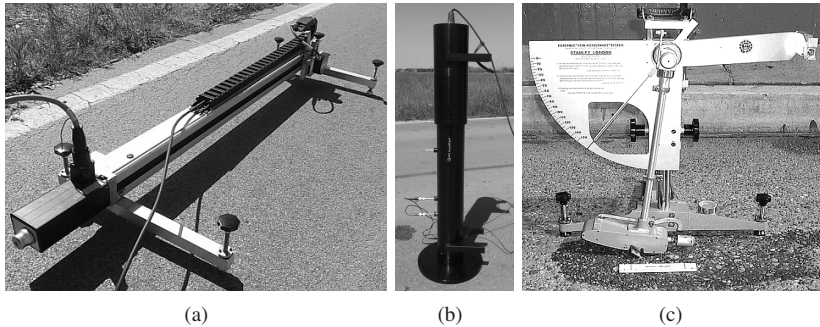
Figure 3.3: Measurement hardware used to characterize the road surface properties

3.1.3 Measurements analysis procedure

The global analysis method to study road surface influence on TiRN is depicted in Fig. 3.4. A first database contains all acoustic measurements, either in the near field using the CPX measuring method (see section 3.1.1) or in the far field using the coast-by method (see section 3.1.1). A second database collects the different road surface descriptors.

Only scalar descriptors will be used for the statistical analysis so the multi-dimensional descriptors (see section 2.2.3) are first reduced to scalars using FPCA (see section 2.4.1). A correlation analysis is then performed on the database of road surface characteristics to understand the relationships between the scalar descriptors and to understand the FPCA results. All statistic analyses depicted by gray diamonds in Fig. 3.4 are performed using the commercial software JMP Pro 14.1.
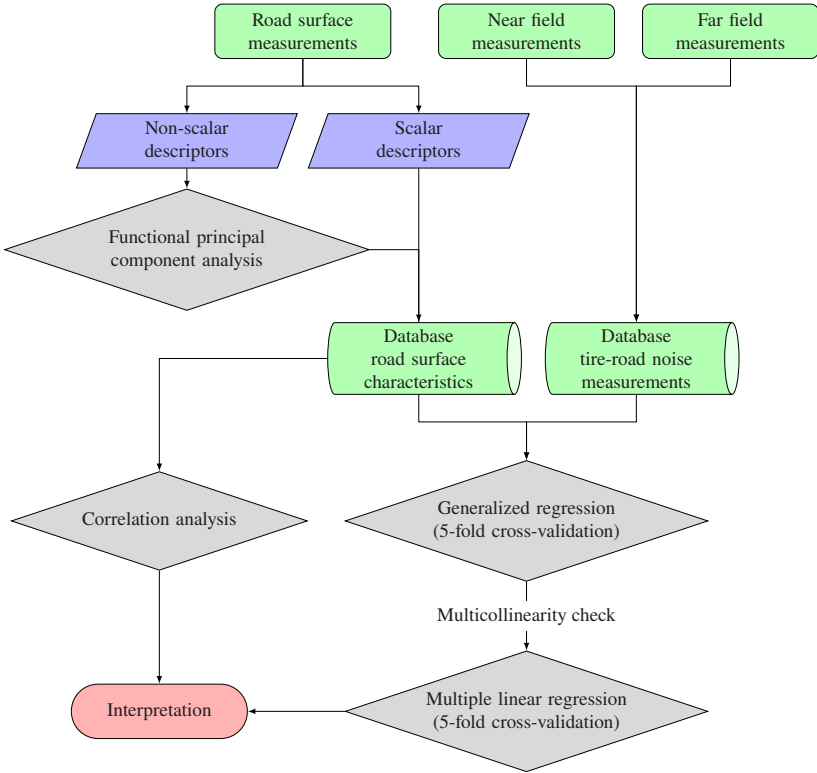
Figure 3.4: Measurement analysis procedure from field measurements to results interpretation

To quantify the interaction between TiRN, road surface characteristics and operating parameters, a statistical analysis in three steps is realized. A first generalized regression is performed to automatically select the significant variables using the adaptive double lasso as shrinkage technique (see section 2.4.3). To avoid keeping several variables with the same influence on the predicting output, a multicollinearity check is performed to identify correlated variables (see section 2.4.4). Once correlated variables are sorted out, a standard multiple linear regression is performed with the remaining variables (see section 2.4.2). To avoid overfitting, the regression algorithm is first trained with a training set and tested with a validation set. This is realized with a 5-fold cross-validation,

as presented in section 2.4.4. Residuals normality is checked using a normal quantile plot. The final intepretation step is performed by comparing the results from the multiple linear regression with these from the correlation analysis.

3.2 Tested tires and road surfaces

3.2.1 Tires

The tested tires have the dimension 205/55R16 and their tread pattern geometry can be seen in Fig. 3.5. The summer tire is a Michelin Primacy3 91W and the winter tire is a Michelin Alpin5 94H. The last tire is a slick tire in which circumferential grooves were cut with a depth of two millimeters. These grooves were required in order to perform measurements on public roads. To study the interaction between operating parameters, road surface and groove resonance noise, the grooves of the summer and winter tires were filled with acoustic foam (see Fig. 3.5d and 3.5e). Due to safety issues, these two tires were only tested on the inner drum test bench. The tires were mounted on the same rim, whose reference is Speeds 06SP (7.50 x 16 ET 46.00). To monitor inflation pressure, TPMS sensors from Schrader were used.
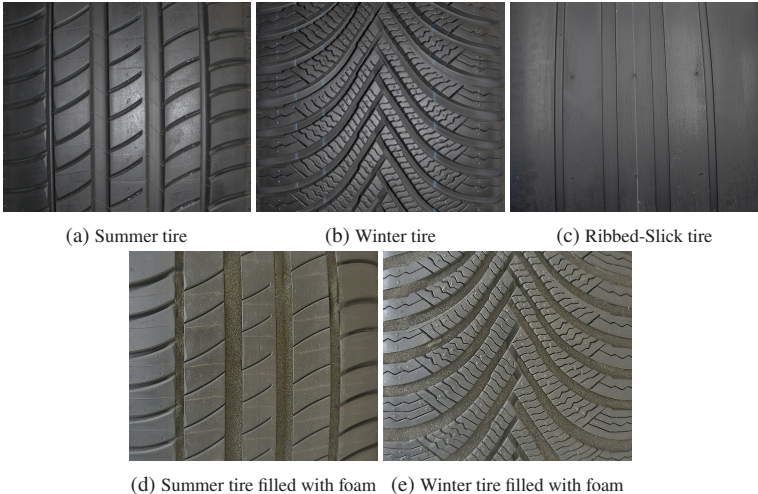

(a) Summer tire   (b) Winter tire   (c) Ribbed-Slick tire

(d) Summer tire filled with foam   (e) Winter tire filled with foam

Figure 3.5: Measured tires within this work (from [112])

3.2.2 Road surfaces

CPX measurements on the inner drum test bench

To study the road surface influence on TiRN and on groove resonance noise in the near field, five different road surfaces were used. The three asphalt surfaces are standard asphalt mixtures coming from an asphalt mixing plant. Asphalt 0/5 has chippings with a diameter between 0 mm and 5 mm, while the chipping diameter of Asphalt 0/11 follows a sieve curve between 0 mm and 11 mm. Accordingly, the stone-mastic-asphalt (SMA) 0/8 has stones between 0 mm and 8 mm and Concrete 0/16 contains pebble stones up to a diameter of 16 mm. Safety-Walk is an artificial surface from the 3M company brought directly on the steel drum surface. Its surface is made of corundum and has a granularity of 80. The MPD, the absorption coefficient α as well as a visual overview of each road surface are given in Fig 3.6. The other road surface characteristics used in the statistical analysis are detailed in appendix A.1.1

Although the mixture of Asphalt 0/5 does not follow the ISO 10844 requirements, its MPD and its absorption value are within the tolerances of the ISO 10844 standard.

Coast-by measurements

A total of 32 test tracks were used in this work. Thirteen of them are ISO 10844 certified test tracks and 19 are public roads (see Table A.6). Several road surfaces were build for the research project "Leiser Straßenverkehr 3" [80] on the NATO airbase in Geilenkirchen, Germany. These tracks were used as public roads for this work, as well as public roads located in the vicinity of Pisa in Italy. Due to confidentiality issue, the name of the ISO 10844 test tracks owner will be anonymized. One standardized test track did however not follow the standard requirements, as the driving lane was replaced with a normal asphalt mixture used on national roads and highways. This test track was therefore considered as a public road.

(a) Safety-Walk
MPD = 0.15 mm, α = 0.1%

(b) Asphalt 0/5
MPD = 0.37 mm, α = 2.7%

(c) Asphalt 0/11
MPD = 1.15 mm, α = 2.3%

(d) SMA 0/8
MPD = 1.19 mm, α = 12.2%

(e) Concrete 0/16
MPD = 1.44 mm, α = 1.0%
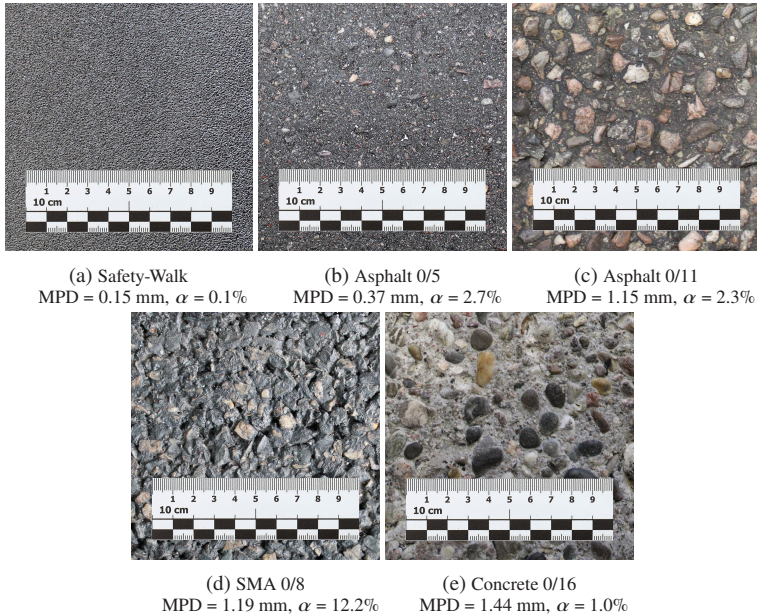
Figure 3.6: Road surface from the inner drum test bench (from [112])

3.3 FEM model of the groove resonance phenomenon

In section 4.2, a focus will be set on the groove resonance phenomenon, which will be investigated experimentally and numerically. To do so, a FEM approach is used in order to study the influence of several parameters on groove resonance. Twelve models are created in order to study all the possible interactions between groove resonance and:

- Tread pattern: summer or winter tire

- Tire load: 2400, 3600 or 4800 N

- Drum curvature: inner diameter of 3.8 m or infinite (flat track)

<div align="center">(a)   (b)   (c)</div>

Figure 3.7: Transformation process from paper and ink to CAD geometry

The groove resonance model is built from footprints made inside the inner drum test bench. The steps to transform the footprint to a CAD model is visualized in Fig. 3.7 for the summer tire. For the same tire loads used during the TiRN measurements, a footprint of each serial tire is made using ink and paper (see Fig. 3.7a). An image processing tool [119] is then applied to detect the footprint boundaries and to reduce the tread blocks edges to quadratic functions for the summer tire (see Fig. 3.7b). Due to the longer tread blocks of the winter tire, spline functions were used to model the tread block edges.

The footprint is then extruded to a profile height of 8 mm (see Fig. 3.7c) and fused to the geometry of a deformed tire under rolling condition provided by the tire manufacturer. This geometry is then subtracted from a half-sphere having a diameter of two meters in order to have the three-dimensional geometry of air surrounding the tire (see Fig. 3.8). This approach is very similar to the model presented in [40]. The model is developed using Abaqus 2017 based on the first results presented in [120]. Second-order tetrahedral acoustics elements build the air volume surrounding the tire and quadratic tetrahedral infinite elements are added on the half-sphere to simulate free-field conditions. The elements

inside the contact patch were meshed with a target element length of 4 mm. The ground and the tire are considered perfectly sound-reflecting. Air density and adiabatic bulk modulus are computed at 20 °C using the ideal gas theory. This results in an air density of 1.204 kg/m^3 and a bulk modulus of 0.142 MPa.
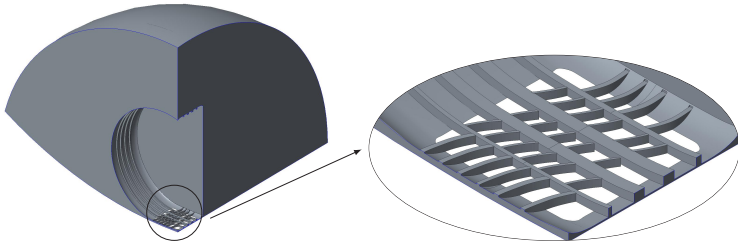
Figure 3.8: Geometry used as input for the FEM computation of groove resonance frequency. Only a quarter of the model is displayed in order to improve the visibility.

The four circumferential grooves of the summer tire are excited at the leading edge and the SPL is computed at the trailing edge. For the winter tire, each groove is excited at the footprint center and the SPL is extracted at the tire sidewalls. All grooves are excited simultaneously using a volumetric acceleration. By extracting the sound pressures at the output nodes, a transfer function can be computed. These transfer functions are obtained for each groove constituting the groove network and show the pipe network resonance frequencies.

For all transfer functions, the resonance frequencies are extracted and classified manually according to their vibration shapes. The average resonance frequency is then calculated for each vibration mode and compared to the measurements. Only the frequency location of the resonances is analyzed, not the resonance amplitude. The analysis is performed between 100 Hz and 3000 Hz with a frequency resolution of 10 Hz.

4 Results

In this chapter, the analysis procedure presented in section 3.1.3 will be applied to the different TiRN and road surface measurements.

First, the characteristics of all measured road surfaces will be analyzed. Results of curve reduction to scalar descriptors using FPCA will be studied and interpreted using a correlation analysis. These results will be used later to understand the regression results. Using a boxplot analysis, it will then be checked if standardized ISO 10844 test tracks are representative of public roads. This will help assessing the major differences between these road surfaces. This section will then be concluded by an analysis of the relevance of END_T, which is the parameter proposed in the ISO 10844 standard to correct the influence of variations in the roughness amplitude spectrum on TiRN.

A focus will also be put on the groove resonance phenomenon. An experimental analysis will help understand the influence of road surface and operating parameters on this TiRN generating mechanism. A numerical analysis will complete the picture in order to compute the influence of tire load and drum curvature on the groove resonance frequency.

The aim of this research work is to study the influence of road surface on TiRN. Due to confidentiality issues, the measured and predicted SPL values of total TiRN will not be given. This is why only the regression coefficients for the significant parameters are given afterwards, without the intercept value.

4.1 Road surface descriptors

4.1.1 Functional principal component analysis

To study the influence of road surface characteristics on TiRN using the method presented in section 3.1.3, scalar descriptors are needed. Graphical descriptors of the road surface roughness need therefore to be reduced to scalars so that they can be used as input in the generalized regression. To this end, FPCA is applied to the roughness amplitude band spectrum and to the Abbott curve of the roughness profile. The FPCA results are the eigenfunctions which describe the main modes of variation of the curve and the FPC. The influence of the FPC sign on the non-scalar roughness descriptor need to be investigated in order to ensure a physical understanding of the FPC meaning.

The cumulative percentage of variance explained is the criterion to limit the number of FPC. As long as 95 % of curve variance is not explained, eigenfunctions are added to the FPCA. For the third-octave roughness band spectrum, this results in three eigenfunctions explaining respectively 67 %, 20 % and 8 % of the spectrum variance. For the Abbott curve, only two eigenfunctions are needed. The first eigenfunction explains 91 % of the variance and the second 6 %.

The FPCA eigenfunctions are depicted in the left part of Fig. 4.2 for the Abbott curve and Fig. 4.1 for the roughness amplitude band spectrum. To demonstrate the influence of each FPC, a variation of the FPC is depicted on the right part of the same figures. These variations are a graphical representation of Eq. 2.12. The dark green curves correspond to the average value of the projected curve $\widehat{\chi_K}$, while the blue curves depict a positive FPC (i.e. $\eta = 0.2$) and the red curves illustrate a negative FPC (i.e. $\eta = -0.2$)

To facilitate the physical interpretation of the FPCA results, a comparison between the eigenfunction of the functional data and the vibration shape of a beam can be made. The first eigenfunction of the roughness band spectrum can be compared to the first flexion mode of a beam fixed at one end and simply supported at the other (see Fig. 4.1a). A positive value of the first FPC (blue curve in Fig. 4.1b) will therefore lead to a global increase of the roughness spectrum compared to the mean value. On the contrary, a negative value of the first FPC (red curve in Fig. 4.1b) will lead to a reduction of the roughness

(a) Eigenfunction 1

(b) Variation of Ltx FPC1

(c) Eigenfunction 2

(d) Variation of Ltx FPC2

(e) Eigenfunction 3

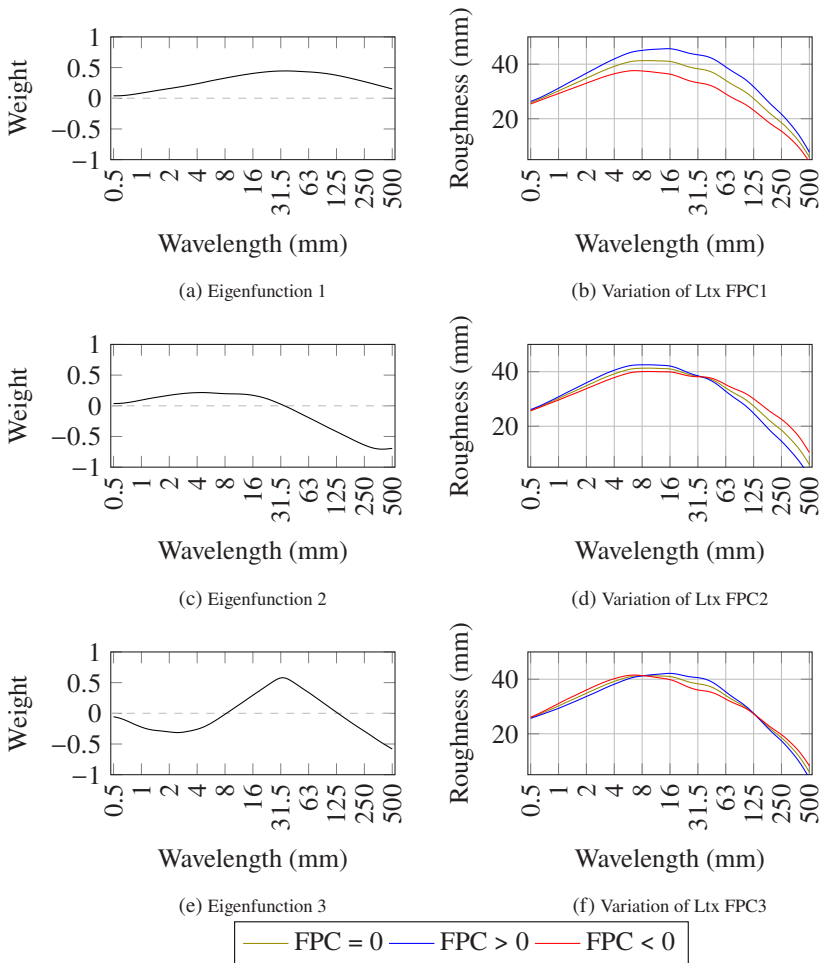(f) Variation of Ltx FPC3

FPC = 0 —— FPC > 0 —— FPC < 0

Figure 4.1: FPCA results for the texture amplitude spectrum for the field measurements. The left diagrams depict the eigenfunction of the roughness spectrum and the right diagrams show the influence of the FPC's sign on the spectrum.

band spectrum and therefore to a "smoother" road surface. The influence of

Ltx FPC1 is particularly high on the macro-roughness domain, at wavelengths between 4 mm and 31.5 mm.

The second and third eigenfunctions look like the second and third flexion modes of a beam with a fixed-free boundary condition. The second eigenfunction has a node at a wavelength of 31.5 mm (see Fig. 4.1c). This means that a positive Ltx FPC2 will lead to a road having a higher proportion of roughness in the wavelength domain below 31.5 mm compared to the average roughness band spectrum (blue curve in Fig. 4.1d). On the contrary, a negative Ltx FPC2 will lead to a road having a higher amount of mega-roughness compared to the average roughness spectrum (red curve in Fig. 4.1d).

The third eigenfunction has two nodes, one around 8 mm and another at 125 mm (see Fig. 4.1e) and splits the macro-roughness domain in two: wavelength above 8 mm and wavelength below 8 mm. As depicted in Fig. 4.1f), a positive value of Ltx FPC3 will lead to a predominance of bigger wavelengths in the macro-roughness domain (blue curve in Fig. 4.1f). A negative value of Ltx FPC3 will therefore lead to a shift of the roughness band spectrum towards the micro-roughness domain (red curve in Fig. 4.1f). As the average mega-roughness of the measured road surface is low, the influence of the third eigenfunction on mega-roughness can be neglected.

A comparison with vibration modes for the Abbott curve is also possible. The first eigenfunction is similar to a rigid body vibration mode with a node at a cumulative probability of 50 % (see Fig. 4.2a). The second eigenfunction looks like the first flexion mode of a beam having free boundary conditions at both ends. This results in two vibration nodes, one around 25 % and another at 70 %.

Interpreting variations in the Abbott curve is not an easy task. The influence of a positive or negative FPC of the Abbott curve on the probability density function is therefore computed and illustrated in Fig. 4.3. The first eigenfunction changes the spread of the roughness distribution function. A positive value of Abbott FPC1 will increase the roughness amplitude span (blue curve in Fig. 4.3a) while a negative Abbott FPC1 will compress the roughness distribution function around 0 mm (red curve in Fig. 4.3a).

The second eigenfunction of the Abbott curve has almost no influence on the distribution spread. It describes to what extent the probability density function is asymmetric and whether or not the values are concentrated around a value. A

(a) Eigenfunction 1

(b) Variation of Abbott FPC1

(c) Eigenfunction 2

(d) Variation of Abbott FPC2

FPC = 0 —— FPC > 0 —— FPC < 0
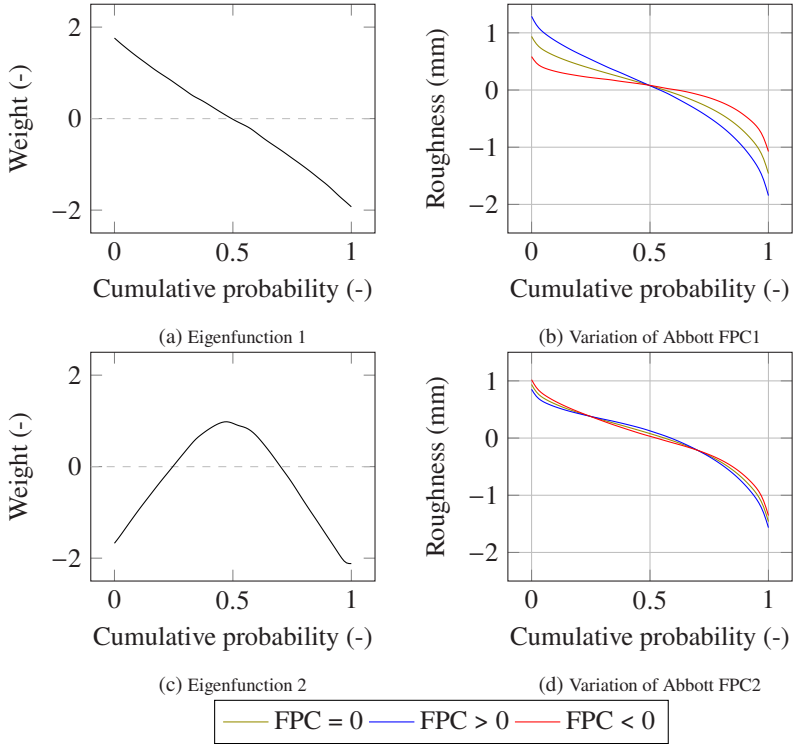
Figure 4.2: FPCA results for the Abbott curve for the field measurements. The left diagrams depict the eigenfunction of the roughness spectrum and the right diagrams show the influence of the FPC's sign on the spectrum.

positive value of Abbott FPC2 leads to a peakier distribution and to an increased negative skewness (blue curve in Fig. 4.3b). On the contrary, a negative value of Abbott FPC2 leads to a distribution function more evenly distributed along the whole roughness amplitude domain. The distribution skewness also seems to increase towards positive values by decreasing Abbott FPC2 (red curve in Fig. 4.3b).

The FPCA of road surfaces from the inner drum test bench shows similar results, which are depicted in Appendix A.2.1. The major difference is that the first eigenfunction of the texture amplitude spectrum has a standard weight

which is negative (see Fig. A.2a). This means that a positive Ltx FPC1 for real roads will correspond to a negative Ltx FPC1 on the inner drum test bench. Another major difference is the number of eigenfunctions required to explain 95 % of the texture spectrum variance. Only two FPC are required, the first one explaining 90.2 % and the second one 5.9 % of total variance. The observation made for Ltx FPC1 is also true for the second FPC of the Abbott curve (compare Fig. 4.2c with Fig. A.1c). A negative Abbott FPC2 on real roads corresponds to a positive Abbott FPC2 on the inner drum test bench.

(a) Abbott FPC 1   (b) Abbott FPC 2

—— FPC = 0 —— FPC > 0 —— FPC < 0
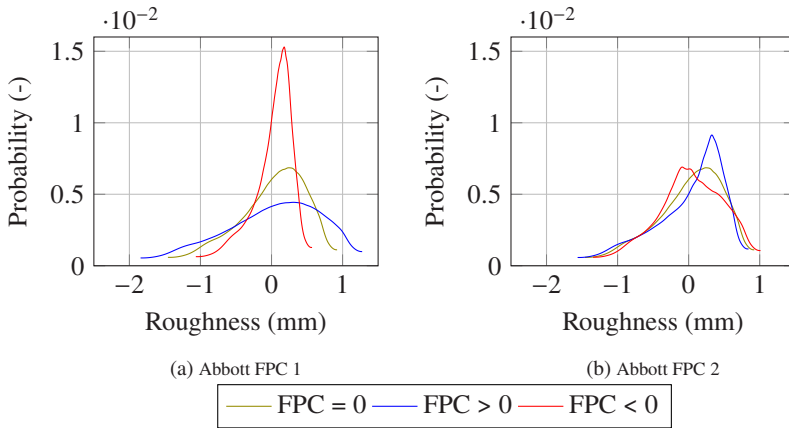
Figure 4.3: Influence of the FPCA of the Abbott curve on the roughness distribution curve

4.1.2 Correlation analysis between road surface descriptors

To understand the physical meaning of each roughness scalar descriptor, a correlation analysis is performed between all scalar descriptors by computing the Pearson's correlation coefficient. Results for the real road surfaces and for the surfaces from the inner drum test bench are depicted in Fig. 4.4. A correlation coefficient close to one indicates a positive linear relationship between two descriptors: an increase of the first variable leads to an increase of the second variable. On the contrary, a correlation coefficient close to -1 will lead a linear decrease of the second variables if the first one is increased.
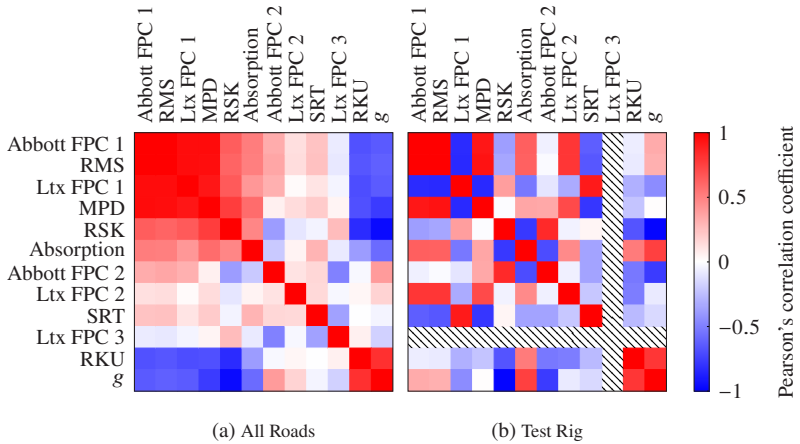
Figure 4.4: Correlation analysis between road surface descriptors for public roads and road surfaces from the inner drum test bench. Ltx FPC3 has no correlation value for the test rig's correlation map because only two FPC are required to explain 95% of the texture spectrum variation. The exact coefficients can be found in Appendix A.2.2

Several trends can be extracted from Fig. 4.4a. There seems to exist two correlation clusters:

- Texture amplitude: very strong positive correlation between Abbott FPC1, RMS, Ltx FPC1 and MPD
- Texture orientation: very strong correlation between RSK, g and RKU

Other strong correlations are observed between these two clusters. There is namely a strong positive correlation between the MPD and RSK. An increase of the MPD will e.g. lead to an increase of RSK, and therefore to a more positive orientation of the texture roughness.

Another interesting correlation is between the absorption coefficient and the correlation cluster "texture amplitude". It seems that acoustic absorption will increase with the roughness amplitude. As absorption is mainly generated by interconnected voids inside the asphalt layer, this result could be expected. Obtaining such voids is easier with a coarser asphalt mixture, which leads to an increase of surface roughness amplitude.

The influence of Abbott FPC2 on the distribution function supposed after analyzing Fig. 4.3b is partially confirmed by the correlation analysis. There is a moderate negative correlation between Abbott FPC2 and RSK. This means that a decrease of Abbott FPC2 will lead to an increase of the skewness. As Abbott FPC2 moderately correlates with the texture amplitude descriptors, an increase of Abbott FPC2 will also lead to an increase of the roughness amplitude level. It seems from the correlation analysis that Abbott FPC2 represents a balance between roughness amplitude and its orientation.

Due to the reduced amount of road surfaces on the inner drum, results from the correlation analysis differ slightly from these obtained on real roads. The correlation results inside the inner drum must be analyzed carefully because only five data points are available. These results are namely expected to be very sensitive to pure leverage points [94].

As for measurements performed on real roads, a very high correlation is also observed on the inner drum test bench between the variables describing roughness amplitude : Abbott FPC1, RMS, Ltx FPC1 and MPD. Due to the negative weighting of the first eigenfunction of the texture amplitude spectrum, the correlation coefficient sign shifts between Ltx FPC1 and the other three parameters describing the roughness amplitude. Ltx FPC2 also correlates with parameters describing texture amplitude. The almost perfect correlation between g and RSK also remains, as they both describe texture orientation. The kurtosis RKU also highly correlates with these two previous variables.

A very strong correlation is observed between SRT and the parameters describing texture amplitude. This is due to the high leverage of the Safey-Walk surface, which has a very low macro-roughness but a very high grip level compared to the other road surfaces. The same effect is seen between RSK and Absorption. Due to the relatively high Absorption and very negative RSK of the SMA 0/8 surface, this point acts as a pure leverage point on the correlation analysis. Both correlation results are however coherent, as the grip level will be higher on smooth surfaces without macro-texture (i.e. low MPD). A very negative RSK might also lead to a flat surface with interconnected voids and thus a higher absorption, if the roughness amplitude level is high enough.

The correlation analysis enables a better physical understanding of the road surface describing parameters. It also confirms the analysis of the FPCA results made in section 4.1.1. Several clusters could be identified such as rough-

ness amplitude and texture orientation. Although the correlation coefficients between some parameters are close to one, some road surface measurements deviate from a perfect regression line. The correlation map gives a global trend on the relationship between two parameters, so that one parameter cluster can therefore not be reduced to a single parameter. This is why all parameters will be used afterwards during the variable selection process. The model shape will not be influenced and the correlation analysis will help interpreting the influence of the significant parameters.

4.1.3 Representativity analysis between public roads and ISO 10844 test tracks

To see if ISO 10844 standardized test tracks are representative of public roads, a comparison of the distribution for the MPD, the absorption coefficient and the texture orientation is depicted using a boxplot in Fig. 4.5. The outer edges of the box describe the 25th and the 75th percentiles of the samples, while the line in the middle of the box describes the median value. The black points are measurements that do not fit within the boxplot whiskers. This corresponds to a sample value more than 1.5 times the interquartile range (i.e. 1.5 times the height of the box) away from the bottom or the top of the box. The whiskers extend to the minimum and maximum data points which are not considered as outliers.

It seems that standardized test tracks are much smoother than public roads. While the median MPD value lies around 0.5 mm for ISO 10844 standardized test tracks, public roads show a median MPD slightly above 1 mm. The MPD values on ISO 10844 test tracks variate – as specified in the standard – between 0.3 mm and 0.7 mm while public roads have MPD values mostly between 0.7 mm and 1.4 mm. Values outside of these limits are however observed. The two very low MPD correspond to roads #21 and #30 from Table A.6: a mastic asphalt in Geilenkirchen and a very smooth polished road surface in Italy. Usually, mastic asphalt is rubbed with sand or chippings are scattered on the freshly laid asphalt layer to increase the road surface macro-roughness. This was not the case for the mastic asphalt measured here, which can be compared to a surface used for industrial flooring or underground parking lots. These tracks can therefore not be considered as representative of public roads.
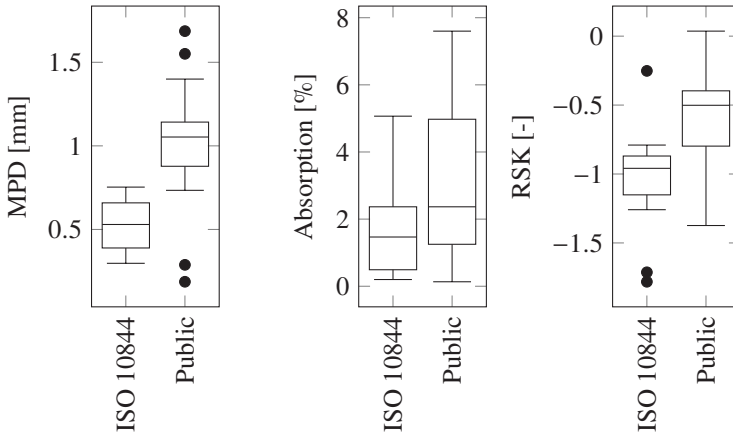
Figure 4.5: Comparison of the MPD, absorption coefficient and skewness distribution for ISO 10844 test tracks and public roads

On the other hand, absorption values of standardized test tracks do not differ greatly from these of public roads. There is namely a greater overlap of the boxplots compared to the MPD. The median absorption coefficient lies around 1.5 % for ISO 10844 test tracks and around 2.4 % for public roads. Although public roads tend to have a greater variation of the absorption coefficient, it still remains within the limits of 8 % required by the ISO 10844 standard and way below the absorption values measured on open-porous surfaces. Porous pavements can namely have an absorption peak reaching 95 % [121].This work focuses however on compact road surfaces, which induces a very low absorption coefficient. Introducing open-porous pavements into the analysis would lead to a much greater spread of the absorption coefficient values, because of high absorption capacities of this surface type.

The last comparison is made for texture orientation, by using the skewness RSK. Standardized ISO 10844 test tracks have a median skewness of -1 while public roads have -0.5. This means that public and ISO 10844 road surfaces have a texture orientation which is negative or close to a normal distribution. This could be expected, as a long-time rolling of a tire on a surface could lead to a polishing effect. With sufficient abrasion time, chippings on the upper layer will be torn off from the asphalt layer and positive oriented roughness

will therefore be polished away. As a consequence, only the negative texture will remain.

4.1.4 Relevance of the END_T

END_T was proposed in the 2011 version of the ISO 10844 standard to compute the SPL variation of coast-by measurements compared to a reference test track. This is not a normative part of the standard and aims at quantifying texture spectrum influence on belt vibration noise and air pumping noise. This computation relies only on the test track roughness band spectrum and is summarized in section 2.3.2. The relevance of this parameter will be studied using coast-by measurement results. To that end, an estimation of END_T is computed according to Eq. 4.1 using only TiRN measurements.

$$\widehat{END_{T_i}} = SPL_i - SPL_{ref} \tag{4.1}$$

where: $\widehat{END_{T_i}}$ END_T estimation from Coast-By measurements [dB]

        SPL_i Coast-By SPL of test track i [dB]

        SPL_{ref} Coast-By SPL of the test track identified as reference [dB]

Figure 4.6 depicts END_T computed according to the ISO 10844 standard for all ISO 10844 test tracks using gray columns. The road surface number corresponds to the denomination in Table A.6. It seems that test track #4 has a texture spectrum very close to the road surface used as reference in the ISO 10844 standard, as the expected noise difference is of only 0.05 dBA. This road surface will be taken as reference to judge the quality of END_T. The Coast-By SPL are computed for all ISO 10844 test tracks according to the R117 regulation at a reference speed of 80 km/h. The estimated $\widehat{END_T}$ for all tires is presented in Fig. 4.6 using black, red and blue columns.

Although the estimated END_T from Fig. 4.6 do not seem to match with the computed END_T from Fig. 4.6, this could be due to the different inflation pressure used in this work compared to the requirements from the R117 regulation. It was namely decided to use an inflation pressure of 2.5 bar in warm state, which is more representative of inflation recommendations of car manufacturers, but highly above the requirements from the regulation. If the tire were to be tested according to R117, inflation pressure should be around 1.8 bar. Even
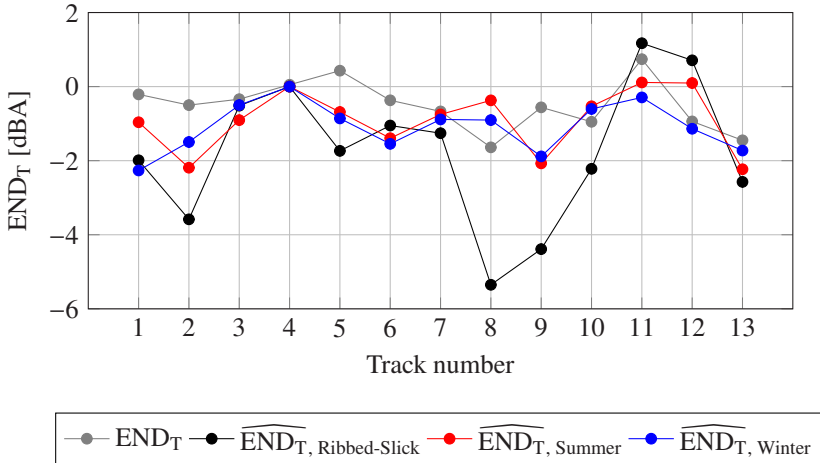
Figure 4.6: The computed END_T is calculated according to ISO 10844. The estimated $\widehat{END_T}$ is obtained by taking road surface #4 as reference track (see Table A.6).

if the absolute values of END_T do not match with the inter-site noise variation, the fluctuation should be proportional if END_T is adequate to describe road surface texture influence on TiRN variation.

To show whether END_T is adequate, a correlation analysis is performed using the Pearson's and the Spearman's correlation coefficients, respectively denoted ρ and r_s. The first one checks if the relationship between two parameters is linear while the second tests if the relationship can be explained with a monotonic function [104]. Both correlation analyses deliver the same result. There is a moderate correlation for the ribbed-slick tire and a weak correlation

for the serial tires between the END_T computation from the ISO 10844 standard and the noise variation observed between the ISO 10844 test tracks:

- Ribbed-slick: $\rho = 0.54$; $r_s = 0.55$

- Summer: $\rho = 0.30$; $r_s = 0.13$

- Winter: $\rho = 0.29$; $r_s = 0.24$

The highest correlation coefficients are observed for the ribbed-slick tire. This is logical, as END_T is supposed to model the influence of surface roughness on noise emitted by tire belt vibration and air pumping. As the ribbed-slick tire has no tread pattern and a very low groove depth, these two phenomena should be the main contributors to TiRN for this specific tire.

For serial tires with tread patterns, there is neither a linear nor a monotonic relationship between END_T and noise variation between the ISO 10844 test tracks measured in this work. END_T alone is not sufficient to explain noise variation due to texture level variation. The contribution of tread pattern and groove resonance noise to TiRN is namely neglected by END_T, which might explain this poor correlation.

However, the general evolution of the estimated END_T for serial tires is somewhat similar to the evolution of END_T directly computed from the texture spectrum. This indicates that the roughness amplitude band spectrum used to compute END_T might be a relevant acoustic descriptor for TiRN generation.

4.2 Analysis of the groove resonance phenomenon

This section is based on results previously published in [112], using measurements inside the inner drum test bench. Measurements on Safety-Walk were added to the analysis and all road surface descriptors presented in section 2.2 are used during the variable selection process. The numerical analysis is also expanded to study the influence of drum curvature on the groove resonance frequency. The physical quantity studied here is the SPL variation between TiRN measurements of the tires not filled with foam against the tires filled with foam, as explained by Eq. 4.2.

$$\Delta SPL = SPL_{serial} - SPL_{foam} \tag{4.2}$$

where : ΔSPL SPL variation due to the foam insert [dBA]

       SPL_{serial} Measured SPL of the serial tire without foam insert [dBA]

       SPL_{foam} Measured SPL of the serial tire with foam insert [dBA]

4.2.1 Contribution of groove resonance to tire-road noise

The average contribution of groove resonance to TiRN for different speeds, loads and road surfaces equals 1.5 dBA for the summer tire and 1.7 dBA for the winter tire. Figure 4.7 depicts the contribution of groove resonance to TiRN around the tire using a boxplot representation. For the summer tire with circumferential grooves, the highest SPL variation is measured at the leading and trailing edges and at the tire sidewall center. For the winter tire, the highest groove resonance SPL is observed at the microphones oriented towards the tire sidewall (CPX microphones). The rest of this analysis will focus on the microphones where the highest groove resonance noise is measured: the trailing edge for the summer tire and the CPX-middle microphone for the winter tire [112].

The distribution of the groove resonance SPL along the footprint (see Fig. 4.7) could be expected. The circumferential grooves of the summer tire will radiate

(a) Summer tire (b) Winter tire
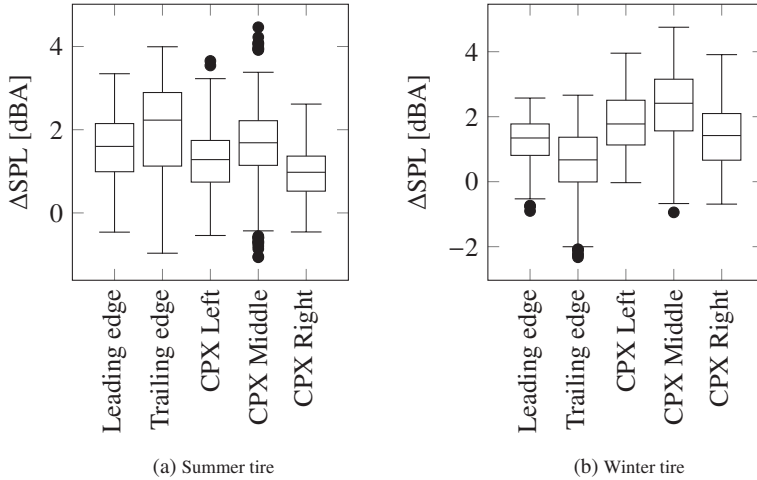
Figure 4.7: Average contribution of groove resonance to TiRN on all road surfaces. The average is computed with all measurements (speeds between 30 and 120 km/h, loads between 2400 and 4800 N).

noise at their opened ends: the leading and trailing edges. The relatively high groove resonance noise level at the CPX-middle microphone can be explained with the transversal grooves. The resonance antinode is namely located at the center of the contact patch. Groove resonance will therefore be ventilated outside the contact patch through the transversal grooves. Since the CPX-middle microphone is located at the tire sidewall towards the middle of the contact patch, observing a high contribution of groove resonance noise at this location is logical. For the winter tire with V-shaped tread pattern, the grooves open up at the tire sidewalls, which explains the high groove resonance noise level at the CPX microphones [112].

The measured contribution of groove resonance noise to TiRN is approximately half of what Saemann measured in [122]. However, the comparison in Saemann's study was made between a slick and a ribbed tire so the tread pattern influence is not taken into account. Furthermore, only one road surface was tested in [122] while the results from Fig. 4.7 are averaged over five different road surfaces. Although this is not specified in the paper, Saemann's measurements are supposed to have been performed on the same test rig presented

in [79], which uses a smooth asphalt replica. The equivalent of a smooth asphalt in this research work would be Asphalt 0/5. The results on Asphalt 0/5 show an average contribution of groove resonance noise to TiRN of 2.9 dBA. These results are therefore in agreement with Saemann's [112].

4.2.2 Driving speed and tire load influence on groove resonance noise

This chapter aims at finding the possible interactions between groove resonance noise, operating parameters (tire load and driving speed) and the road surface parameters. First, a qualitative analysis is performed to estimate the influence of operating parameters on the groove resonance SPL and spectrum. This will help with the interpretation of the statistical analysis which will give a quantitative insight about the interaction between groove resonance noise, operating parameters and road surface descriptors.

The combined influence of tire load and driving speed on the groove resonance SPL for measurements on Asphalt 0/5 is depicted in Fig. 4.8. For the summer tire (Fig. 4.8a), the slope of the groove resonance SPL declines as the driving speed increases. For speeds above 80 km/h, the groove resonance SPL decreases for all tire loads. The non-linear increase of groove resonance noise over the speed in Fig. 4.8a can be explained by the left part of Fig. 4.9 around 80 km/h and 100 km/h. It seems that there is a discontinuity along the speed of the groove resonance contribution. This is especially visible on Fig. 4.9e at 100 km/h. This could be explained by a relative higher contribution of tread impact noise to TiRN [112]. Increasing the driving speed for the summer tire will namely increase the excitation coming from the tread blocks impact and release phenomena. In the meantime, excitation of the groove resonances should remain constant, as the circumferential grooves are parallel to the driving direction. If groove resonance noise lies in the same frequency domain as tread impact noise, the contribution of tread pattern noise to TiRN could be much higher than the groove resonance's. This could explain the reduction of the groove resonance SPL for the summer tire around 100 km/h [112].

For the winter tire (Fig. 4.8b), the groove resonance SPL increases linearly with driving speed. In this case, the grooves are transversal and diagonal to the driving direction. As the driving speed increases, the force variation in

the driving direction will increase which will lead to a higher excitation of the groove resonances, as well as the tread impact and release phenomena. The latter should however radiate more towards the leading and trailing edges, while groove resonance will radiate towards the groove openings at the sidewalls. As the winter tire has very long tread blocks, noise related to their impact and release should also contribute less to TiRN compared to the summer tire.

(a) Summer - Trailing   (b) Winter - CPX-middle

— 2400 N — 3600 N — 4800 N
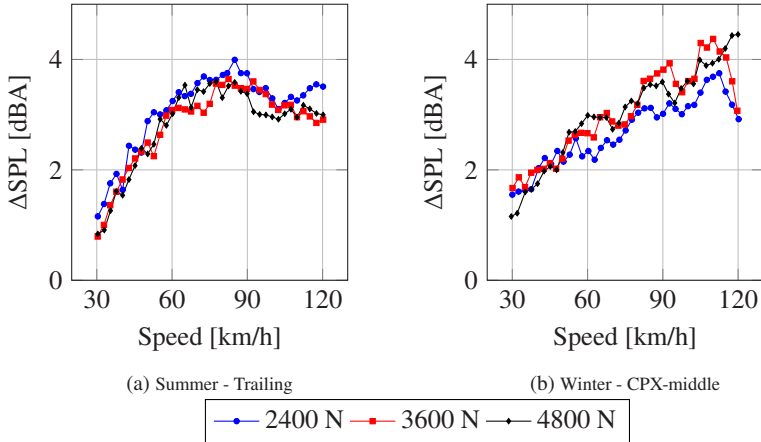
Figure 4.8: Tire load and driving speed influence on groove resonance noise on Asphalt 0/5 (from [112])

Tire load influence on the groove resonance SPL is not clear. It seems that a lower tire load will increase groove resonance noise for the summer tire, while no clear tendency can be seen for the winter tire. The curve slopes in Fig. 4.8b seem to be depending upon tire load, which could lead to an interaction between tire load and driving speed for the winter tire [112]. Although tire load seems to have a relatively low influence on the groove resonance SPL, it has an influence on the spectral content of groove resonance noise. For the summer tire with circumferential grooves (see left part of Fig. 4.9), a higher tire load will result in a decreased groove resonance frequency. This fundamental frequency lies around 1040 Hz for a tire load of 2400 N and around 840 Hz when doubling tire load. A higher tire load also leads to a more defined excitation of the second groove resonance harmonic (see second vertical line around 1700 Hz in Fig. 4.9e) [112].

The influence of tire load on the groove resonance spectrum of the winter tire is similar (see right part of Fig. 4.9). The fundamental groove resonance frequency is reduced from 1000 Hz to 800 Hz by increasing tire load from 2400 N to 4800 N. Due to the complex V-shaped geometry of the winter tread pattern (see Fig. 3.5b), different groove lengths contribute to groove resonance noise. This explains the complexity of the groove spectrum which shows spectral components above 3000 Hz [112]. For both tires, the reduction of the groove resonance frequency with increasing tire load is also logical. For the summer tire, a higher load leads to a longer contact patch and therefore to a longer groove length. For the winter tire with V-shaped tread pattern, an increase of tire load also leads to a slightly wider contact patch (see Fig. 1.1) which also increases the groove length [112].

The previous observations and physical interpretations need to be confirmed using the statistical procedure presented in section 3.1.3. The parameters retained by the double lasso are listed in descending order of significance in Table 4.1 for the winter tire and in Table 4.2 for the summer tire, as well as the prediction error and the quality of fit. The regression equation can be computed by summing the product of the "Variable" and "Coefficient" columns over the table lines.

For both tires, the coefficient of determination R^2 converges towards 80 % and the RMSE lies around 0.5 dBA. The evolution of the prediction error and quality of fit with the number of parameters used inside the model is depicted in Fig. 4.10. Although the best model is achieved with nine parameters for the winter tire and seven parameters for the summer tire, R^2 and RMSE already converge to an acceptable solution for a smaller amount of parameters. The results will be interpreted only for parameters which reduce the validation error by more than 5 %. This corresponds to the first five parameters for the summer tire and the first six variables for the winter tire.

The regression results agrees well with the observations presented in Fig. 4.8 for the operating parameters influence on the groove resonance SPL. The driving speed is the operating parameter having the highest significance on groove resonance noise. Its influence is linear for the winter tire and on a diminishing scale (negative estimate of $Speed^2$ in Table 4.2) for the summer tire. Although tire load influence on groove resonance noise is negligible, a load increase will lead to a small reduction of groove resonance noise for the summer tire (see parameter #7 in Table 4.2). Increasing tire load will lead to a

(a) Summer - 2400 N

(b) Winter - 2400 N

(c) Summer - 3600 N

(d) Winter - 3600 N

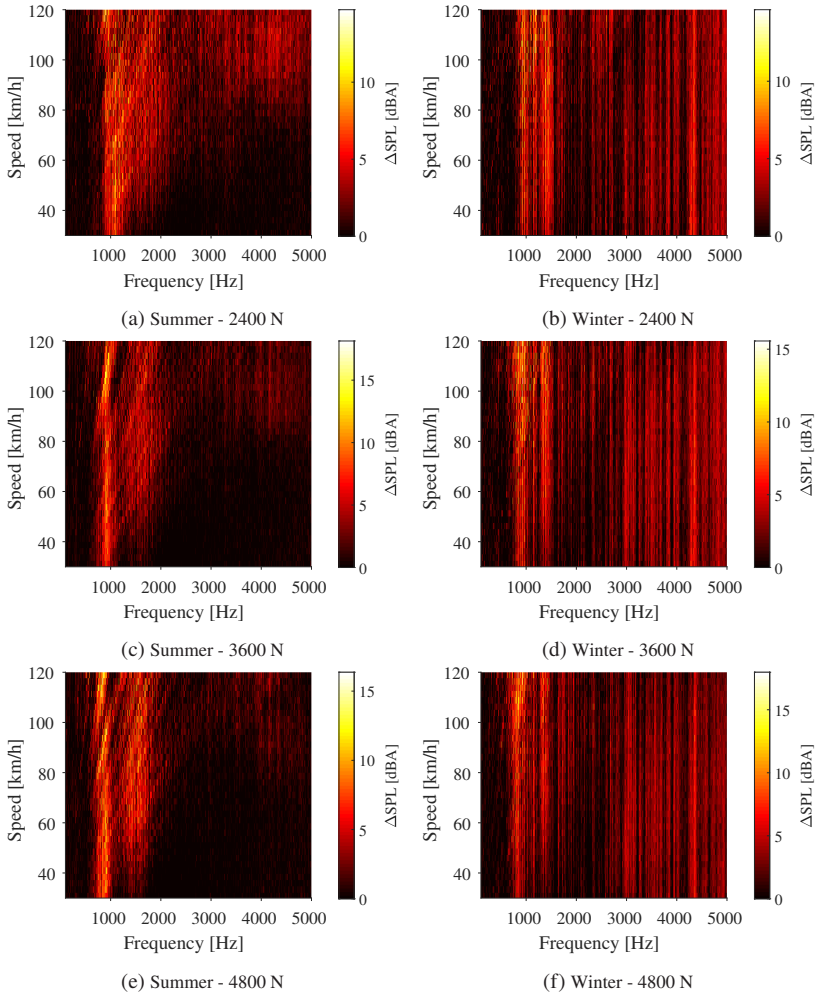(e) Summer - 4800 N

(f) Winter - 4800 N

Figure 4.9: Spectral analysis of groove resonance noise on Asphalt 0/5 of the summer tire at the trailing edge and for the winter tire at the CPX-middle microphone (from [112])

reduced groove resonance frequency. This SPL reduction could be explained by the A-weighting which is applied to noise measurements in order to account
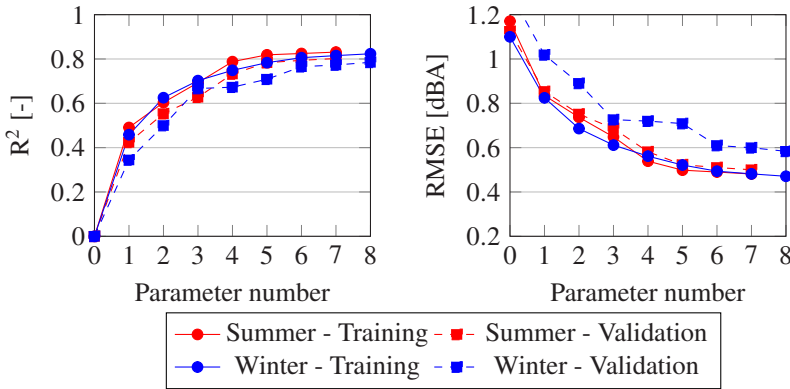
Figure 4.10: Influence of the number of parameters on the multiple linear regression goodness of fit and prediction error. The parameter number corresponds to the first column of Tables 4.2 and 4.1.

for the frequency-dependent sensitivity of the human ear. The lower the noise frequency, the more it is penalized by the A-weighting curve, resulting in fine to a reduction of the A-weighted SPL. However, such an influence should also be observed for the winter tire, which is not the case. Another possibility would be a reduction of the horn effect amplification at lower frequencies. As shown in [123], its amplification is highest for frequencies between 1000 Hz and 2000 Hz. As tire load increases and the groove resonance frequency decreases below 800 Hz, a reduced amplification of groove resonance noise can therefore be expected. As the winter tire will radiate groove resonance noise at the groove openings near the sidewalls, the horn effect should play here a negligible role. It seems that groove resonance noise of the winter tire is much more sensitive to tire load variation, as five out of the nine significant parameters show a dependency with tire load. Increasing tire load will lead to a longer contact patch and therefore to a bigger number of potentially resonating grooves. Although adding the interaction between tire load and driving speed for the winter tire does not drastically improve the prediction quality, it helps explaining the slope difference in Fig. 4.8b [112].

This section focused on the influence of operating parameters on groove resonance noise. Road surface influence and its interaction with groove resonance noise will be studied next.

Table 4.1: Regression results of the groove resonance measurements for the winter tire. The variables are sorted in descending significance order.

#	Variable	Coefficient	Std. Error	t-Ratio	Prob>|t|
1	(MPD-0.86)*(RSK+0.5)	3.39	0.10	33.7	<.0001
2	Speed	0.017	0.001	20.9	<.0001
3	(Speed-75.4)*Ltx FPC1	-3.2e-4	2.5e-5	-12.8	<.0001
4	Load	2.4e-4	2.3e-5	10.2	<.0001
5	(Load-3600)^2	-3.0e-7	3.2e-8	-9.5	<.0001
6	(Load-3600)*Ltx FPC1	-4.7e-6	6.7e-7	-7.0	<.0001
7	(Speed-75.4)*(Load-3600)	4.2e-6	8.7e-7	4.9	<.0001
8	(Load-3600)*Abbott FPC2	1.2e-3	2.6e-4	4.5	<.0001
0	Intercept	0.49	0.11	4.4	<.0001
9	(Speed-75.4)*(RKU-4.43)	3.2e-3	7.4e-4	4.3	<.0001

	R^2	RMSE [dBA]
Training Set	0.83	0.46
Validation Set	0.80	0.57

4.2.3 Road surface influence on groove resonance noise

The following section is also based on the measurements performed inside the inner drum with foam insert glued inside the grooves [112]. After focusing on the influence of operating parameters inside the previous section, the influence of road surface characteristics and interactions summarized in Tables 4.1 and 4.2 will be interpreted.

Interaction between texture amplitude and texture orientation

An interesting result is that the MPD itself has no influence on groove resonance noise (see Table 4.1). This parameter is used with the acoustic absorption to describe the test tracks used for tire approval tests [88]. The most significant road surface parameters are not identical for both tires but they have the same physical meaning. They both represent the interaction between roughness

Table 4.2: Regression results of the groove resonance measurements for the summer tire. The variables are sorted in descending significance order.

#	Variable	Coefficient	Std. Error	t-Ratio	Prob>|t|
1	(RMS-0.52)*(g-0.69)	-19.1	0.56	-34.3	<.0001
2	Speed	0.016	0.001	18.3	<.0001
0	Intercept	1.71	0.11	15.5	<.0001
3	(Speed-75.4)^2	-5.2e-4	3.6e-5	-14.5	<.0001
4	(Speed-75.4)*Ltx FPC1	-3.3e-4	2.5e-5	-13.3	<.0001
5	(Load-3600)*Abbott FPC2	2.4e-3	2.7e-4	9.1	<.0001
6	(Speed-75.4)*(RKU-4.43)	3.3e-3	8.1e-4	4.1	<.0001
7	Load	-9.5e-5	2.3e-5	-4.0	<.0001

	R^2	RMSE [dBA]
Training Set	0.83	0.48
Validation Set	0.80	0.50

amplitude and texture orientation: either MPD*RSK for the winter tire or RMS*g for the summer tire. This interaction is also the most significant parameter of both regressions. The influence of this interaction is shown in Fig. 4.11. Groove resonance noise is increased on:

- a smooth negative oriented surface;

- a rough positive oriented surface.

The first case (lower-left part of Fig. 4.11b) can be explained by a better sealing of the tire on the road. The road surface is too fine to offer connected voids and the resonance is more likely to take place. It is hard to explain the groove resonance increase on a rough positive oriented surface (upper-right part of Fig. 4.11b). One could expect the opposite because the pipe network is not completely closed due to the high macro-roughness level. This should lead to a reduced contribution of pipe resonance to TiRN, as the boundary conditions are not defined well [112]. The measurements show however an opposite behavior. A high positive macro-roughness could lead to a higher excitation of tire structural vibrations. Road impact noise would therefore become the major

contributor to TiRN, leading to a reduction of tread impact noise contribution. This will consequently shift the TiRN frequency peak to lower frequencies and groove resonance becomes in the end the main noise contributor between 800 Hz and 1500 Hz. It is also possible that tire structural vibrations act as a major source of groove resonance excitation.

(a) Summer

(b) Winter
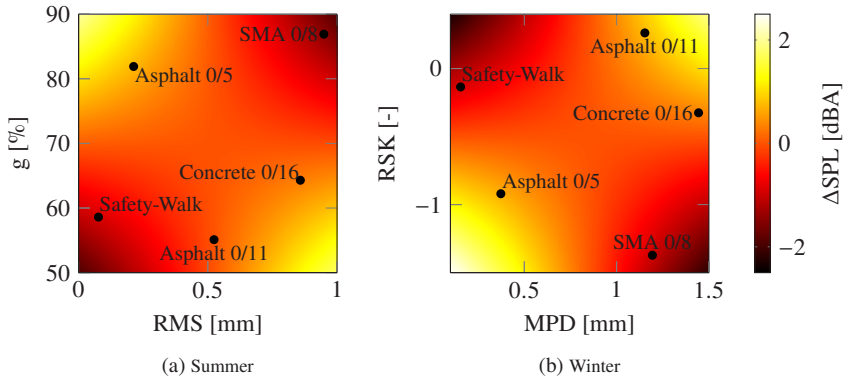
Figure 4.11: Influence of the interaction between roughness amplitude and texture orientation on groove resonance noise

On the other hand, groove resonance decreases on:

- a smooth positive oriented surface;

- a rough negative oriented surface.

A rough negative texture (lower-right corner of Fig. 4.11b) corresponds to a flat road surface with deep voids, which might be connected with one another. This will consequently lead to a non-hermetic seal between the tire and the road, which explains a lesser excitation of groove resonance [112]. It is difficult to interpret the last texture/orientation combination which corresponds to the measurements on Safety-Walk. Although the pipe network shape on this type of surface is perfectly defined, roughness amplitude might be too low to excite groove resonance. On such a smooth surface, road impact noise should be negligible and tread impact noise should be one of the major contributor to TiRN. From the measurement results on Safety-Walk, it seems that the tread

impact phenomenon is not very efficient at exciting groove resonances. A certain amount of macro-roughness might be needed for that.

Interaction between texture amplitude and driving speed

Several interactions are common to both tires and highly significant. The interaction between the driving speed and the roughness amplitude Ltx FPC1 is one of them and is depicted in the upper part of Fig. 4.12. As explained in section 4.1.1, Ltx FPC1 on the inner drum test bench has a strong negative correlation with the roughness amplitude descriptors. A negative Ltx FPC1 therefore leads to an increase of the roughness amplitude.

This influence is mainly due to the high leverage of the measurement point on Safety-Walk, which explains why this interaction was not significant in [112]. The smoother the road, the closer to zero the linear influence of speed on groove resonance noise. This means (e.g. for the winter tire) that groove resonance noise on Safety-Walk is more constant over all speeds while groove resonance on rougher roads such as SMA 0/8 will steeply increase with the driving speed. A similar observation can be made for the summer tire. As depicted in the upper part of Fig. 4.12a, the contribution of groove resonance noise to TiRN for the summer tire is maximum around 90 km/h for all surfaces except for Safety-Walk. This correlates well with the observations on Asphalt 0/5 from Fig. 4.8a. Groove resonance contribution to TiRN seems to be more constant over the speed range on this artificial surface compared to measurements performed on real asphalt and concrete surfaces.

This can be explained by two reasons: the excitation frequency from the road texture and the ratio between groove resonance and tread pattern noise. On the one hand, an extremely positive Ltx FPC1 will lead to a smooth surface with a macro-roughness concentration at wavelengths between 0.5 mm and 2 mm (see Fig. A.1b). On the other hand, a negative Ltx FPC1 (i.e. all roads except the Safety-Walk) will concentrate the roughness spectrum level at wavelengths between 4 mm and 63 mm.

If the road impact phenomenon is considered as a potential excitation source for groove resonance noise, the excitation frequency should lie between 800 Hz and 2000 Hz for the summer tire and above 800 Hz for the winter tire. This excitation frequency is computed by dividing the driving speed with the tex-

(a) Summer   (b) Winter
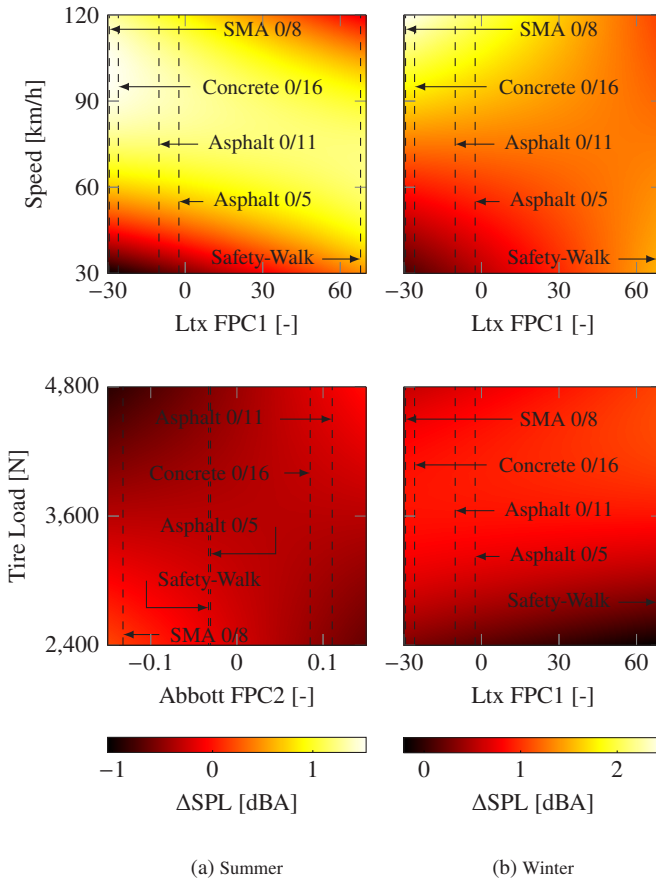
Figure 4.12: Influence of the interaction between driving speed, tire load and road surface parameters on groove resonance noise

ture wavelength. The computed excitation frequency due to the road impact phenomenon is presented in Fig. 4.13. For a smooth road surface (i.e. with a positive Ltx FPC1, see red area from Fig. 4.13), the road impact phenomenon is too high-frequent to be able to excite groove resonance. On the contrary, a rough road surface with a negative Ltx FPC1 (see blue area in Fig. 4.13) will lead to an excitation of the tire exactly inside the frequency range of groove res-

onance. This confirms the suppositions made to explain the low contribution of groove resonance to TiRN observed on Safety-Walk.

Figure 4.13: Texture wavelength influence on the excitation frequency of the groove resonance phenomenon. The red area covers wavelengths between 0.5 mm and 2 mm. The blue area covers wavelengths from 4 mm to 63 mm

The second point is the relative contribution of groove resonance and tread impact noise to TiRN. As mentioned before, a positive Ltx FPC1 will lead to a smooth surface with its macro-texture conce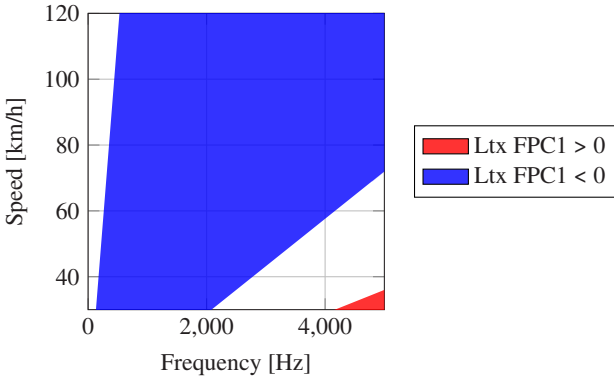ntrated at small wavelengths between 0.5 mm and 2 mm. On the contrary, all surfaces except the Safety-Walk have a negative Ltx FPC1 which shifts the roughness amplitude spectrum from the lower part of the macro-roughness domain towards the upper part of the macro-roughness and the mega-roughness domains. A positive Ltx FPC1 would reduce noise due to the road impact mechanism and increase tread pattern noise. Tread impact would therefore be the major generation mechanism of TiRN at frequencies 800 Hz to 1500 Hz. On the other hand, a negative Ltx FPC1 could lead to a higher excitation of the tire structural vibrations. Road impact noise will therefore become the main contributor to TiRN and will "kill" tread pattern noise. The noise spectrum will be consequently shifted towards lower frequencies. Groove resonance can then be seen as the major noise contributor at frequencies between 800 Hz to 1500 Hz, especially if the roughness spectrum of the road surface coincides with the resonance frequencies of the pipe network.

Interaction between texture amplitude, orientation and tire load

Another significant interaction is between tire load and the road surface characteristics: Abbott FPC2 for the summer tire and Ltx FPC1 for the winter tire. These interactions are shown in the lower part of Fig. 4.12. These figures must however be analyzed carefully due to the relative low number of tire loads and road surfaces analyzed.

According to Fig. 4.4b, Abbott FPC2 has a high negative correlation with the absorption coefficient and the shape factor g. The influence of Abbott FPC2 on the roughness probability distribution function is the same as in Fig. 4.3b, except that the sign of the FPC inside the legend must be switched for both curves. A negative Abbott FPC2 leads to a road surface with a higher absorption and a negative texture orientation. For the summer tire, a positive oriented texture leads to an increase of groove resonance noise if tire load increases. This can be explained by an increase of tire excitation coming from the road. As tire load increases, the contact area increases but with a sub-proportional slope [16]. The averaged contact pressure will therefore increase with an increased tire load and lead to higher excitation of the tire. As depicted in Fig 4.13, road surface excitation lies across the frequency domain of groove resonance, therefore leading to an increase of groove resonance noise.

On the contrary, if the road surface is negatively oriented, absorption will be higher and tire excitation will be reduced. Groove resonance will be less excited and air might not be trapped between the tire and the road due to a higher void content of the road surface. The decrease in groove resonance noise in such conditions can also be explained by a reduced amplification of the horn effect. As the groove resonance frequency decreases with increasing tire load, the groove resonance frequency will become closer to the cutting frequency of the horn, therefore reducing the amplification of groove resonance noise.

The winter tire reacts differently to an increase of tire load. Texture orientation has here no influence on groove resonance noise. The trend is that a reduced tire load will lead to a reduced contribution of groove resonance to TiRN. The smoother the road surface, the steeper this reduction is. This can be explained again by the excitation coming from the road surface. A rough road surface will lead to a higher excitation of groove resonance. Another point is the importance of the contact patch length. A reduced tire load induces a reduction of the contact patch length and therefore to a reduced amount of

resonating grooves. The pipe network is also expected to be better sealed on a smooth compact surface than on a rough surface, which should lead to better boundary conditions for the grooves to resonate. Increasing tire load on a very smooth surface would improve again the contact sealing of the tire on the ground and therefore increase groove resonance noise.

4.2.4 Influence of the deformed tire shape on the groove resonance frequency

A great attention must be paid to the possible interaction between tread pattern noise and groove resonance noise. The statistical analysis showed that groove resonance is increased on smooth surfaces that are negatively oriented. Such a texture orientation would also increase tread pattern noise. A design guideline proposed by Sandberg in [8] was to avoid an overlap of the tread impact harmonics with the groove resonance frequencies.

While the groove resonance frequency is not depending on the driving speed, the tread impact frequency increases linearly with the driving speed. There is therefore a critical driving speed where groove resonance lies on the same frequency domain as tread pattern noise. To ensure that the tire emits as little noise as possible, the computation of the groove resonance frequencies and the critical speeds is needed. The experimental method presented previously is adequate to study the groove resonance contribution to TiRN. However, the measurements were performed inside an inner drum test bench with a certain surface curvature.

It was shown in [16] that the footprint length obtained inside the same inner drum is in average 10 % longer than on a flat road surface. The drum curvature also has an influence on the geometry of the deformed tire and therefore on the efficiency of the horn effect. The influence of drum curvature must be known in order to estimate the groove resonance frequency on a flat track, and thus estimate the critical speed, where groove resonance noise crosses tread pattern noise in the frequency domain.

Computed groove resonance frequencies and corresponding vibration shapes

For both tires, a computed SPL curve is depicted in Fig. 4.14, with an illustration of the corresponding vibration shapes. The vibration shapes can be better observed in Fig. 4.15.

The summer tire footprint can be divided into two parts, each of them consisting of two circumferential grooves connected through transversal grooves and ventilated towards the tire sidewall. The upper part of the footprint has sub-resonators while the lower part does not. Each part has a resonance frequency in the longitudinal direction (see the first two peaks in Fig. 4.14a) [112]. This flexion mode also has a second harmonic (see the third and fourth peaks from Fig. 4.14a). For both resonance modes, the upper half of the footprint with the resonators has a lower resonance frequency compared to the lower half without resonators.

For the winter tire, it consists in a flexion mode of the complete footprint in the transversal direction (Fig. 4.15c for the first harmonic and Fig. 4.15e for the

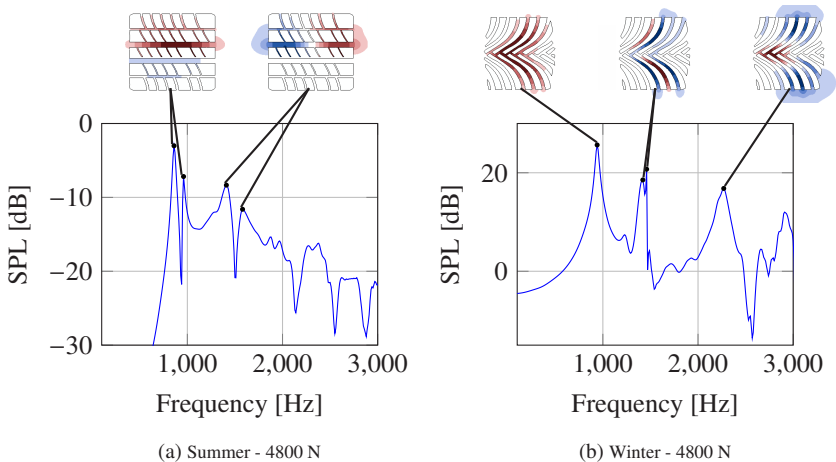(a) Summer - 4800 N   (b) Winter - 4800 N

Figure 4.14: Transfer function obtained using FEM computation with corresponding vibration modes. Resonance shapes are taken over from [112]

second) which respectively correspond to the first and last peaks in Fig. 4.14b [112]. In between lies different resonance frequencies corresponding to the resonance of each individual groove (see Fig. 4.15d). The further away from the footprint center, the shorter the groove length. This leads to a wider spread of the resonance frequencies and therefore to a wide resonance peak or to many resonance peaks in the computed groove resonance SPL of the winter tire.

Model validation

The tire geometry provided by the tire manufacturer comes from a validated thermo-mechanical FEM model rolling in stationary conditions at 80 km/h. The process of reconstructing the groove network from footprints needs to be validated. This is performed by identifying the main resonance modes contributing to groove resonance noise and by extracting their frequencies for all tire loads. Quantifying the error between the measured and computed resonance frequencies will help assessing the prediction quality of the model. As there is no measurement on a flat track to validate the model, the numerical results on a flat surface will be considered valid if the results with the influence of drum curvature fit with the measurements.
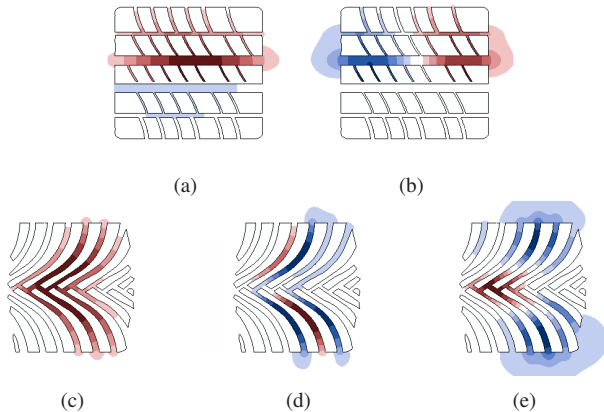
Figure 4.15: Main resonances of the winter tire's footprint inside the inner drum test bench with a tire load of 4800 N (from [112])

As shown in the groove resonance noise maps (see Fig. 4.9), the frequency content of groove resonance noise is not depending on the driving speed. To compare the simulation results with the experimental results, the spectrogram is averaged over the driving speed and the SPL peaks are compared to the computed resonance frequencies [112]. This is depicted in Fig. 4.16 and Fig. 4.17, respectively for the summer and the winter tire. For the summer tire under all tire loads, the computed frequency location of the first and the second groove resonances corresponds perfectly to the measured SPL peaks [112]. Although the simulation method takes place in static conditions, it seems that the groove resonance phenomenon is adequately built for the summer tire. This also confirms the hypothesis that the foam insert has an influence mainly on the groove resonance phenomenon, at least for the summer tire [112].

For the winter tire, the simulation model tends to overestimate the groove resonance frequencies by 175 Hz for the lowest tire load and by 95 Hz for tire loads of 3600 N and 4800 N [112]. This could be due to the simplifications realized to obtain the numerical model. Comparing the winter tire tread pattern from Fig. 3.5b and the corresponding resonance modes of Fig. 4.15 shows that the lamellae are not taken into account during FEM calculation. Including the lamellae into the model would lead to a higher connectivity between the
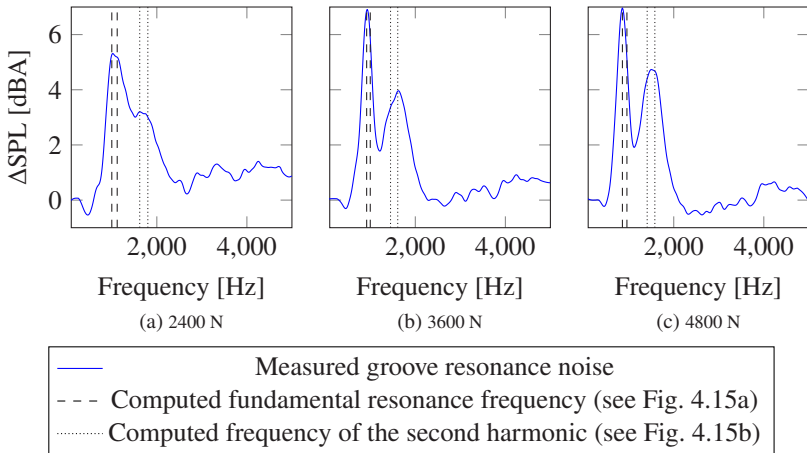
Figure 4.16: Comparison between measured and computed groove resonance frequencies of the summer tire (from [112])
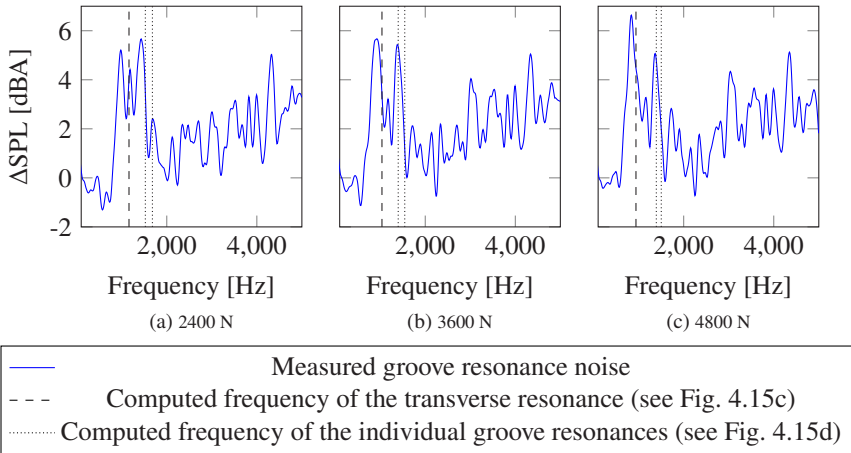
Figure 4.17: Comparison between measured and computed groove resonance frequencies of the winter tire (from [112])

different grooves and therefore reduce the groove resonance frequencies of the winter tire [112]. The experimental results show a high influence of the foam insert on the noise above 2000 Hz. The frequency location of this noise variation does not match with the simulated results and can therefore not be attributed to groove resonance noise [112]. The second harmonic of the footprint transversal resonance does not fit with any of the peaks observed in the measurements.

The previously presented FEM results fit quantatively well the measurement results for the summer tire. For the winter tire, a qualitative trend could also be achieved for the low-frequency domain. Therefore, the developed method is considered adequate enough to compute the influence of several parameters on the groove resonance frequencies, such as tire load and drum curvature. This will be presented in the next section.

Tire load influence on the groove resonance frequency

First the influence of tire load on the groove resonance frequency is analyzed. As depicted in Fig. 4.18a, the groove resonance frequencies of the summer

tire tend to decrease linearly with tire load. According to the pipe resonance theory, the resonance frequency of a groove opened at both ends can be easily computed by dividing the speed of sound by twice the pipe length, as presented in Eq. 2.1. On the inner drum, the footprint length of the summer tire increases linearly with tire load, which agrees with the findings from [16]. This should lead to a non-linear decrease of the groove resonance frequency according to the inverse function. This is true for the central lower groove without quarter wavelength resonator (see red curve from Fig. 4.18a) but the trend for the central upper groove with quarter wavelength resonators seems to be linear.
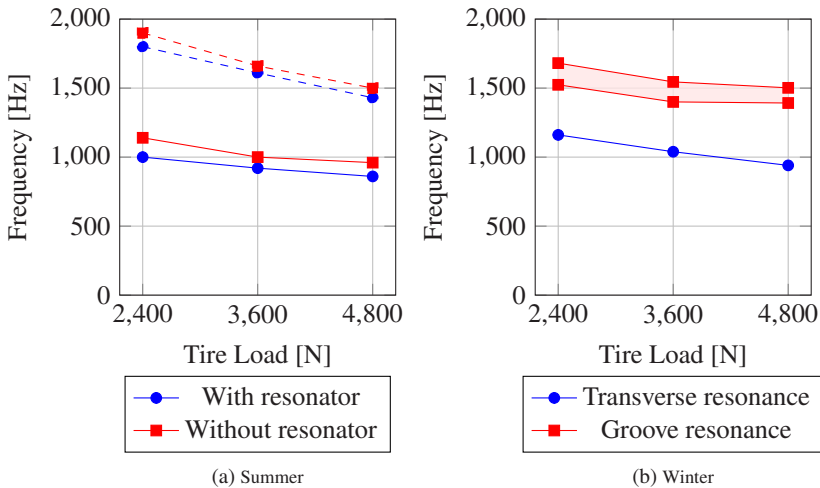
(a) Summer

(b) Winter

Figure 4.18: Tire load influence on the computed groove resonance frequencies of the summer and the winter tires on the inner drum. The dashed lines represent the second harmonic of the fundamental resonance frequency for the summer tire. The corresponding vibration shapes can be seen in Fig. 4.15.

As depicted in Tables 4.3 and 4.4, the pipe resonance theory greatly overestimates the resonance frequencies of tires with circumferential grooves. This can be explained by the boundary conditions modeling. Although end corrections are usually applied to compensate for the finite groove width [17], it still does not account for the influence of the tire deformed geometry. The horn shape between the tire and the road at the trailing and leading edges lead to an extension of the groove length and therefore to a reduction of the groove

resonance frequency. For the summer tire with circumferential grooves, a correction length between 5.8 cm and 8.0 cm is to be applied to account for the influence of the tire geometry on the groove resonance frequency.

The frequency of the winter tire transverse resonance (see blue curve from Fig. 4.18b) decreases linearly with tire load. This constant frequency reduction can be due to an increase of width and length of the contact patch. The decrease of the individual grooves resonance frequencies is not linear and tends to reach a certain plateau (see red curves from Fig. 4.18b). This can be explained by the non-linear increase of the tire width with increasing tire load. As presented in [16], increasing tire load will lead at first to a simultaneous increase in the contact patch length and width. After reaching a certain tire load, the footprint keeps growing only in the longitudinal direction. As the footprint width determines the resonance frequency of each individual groove, this phenomenon explains the non-linear decrease of the groove resonance frequency with increasing tire load.

Table 4.3: Comparison between the pipe resonance theory and the FEM computation of the summer tire groove resonance frequencies on the inner drum

	With resonator			Without resonator		
Tire Load [N]	2400	3600	4800	2400	3600	4800
Pipe theory [Hz]	1937	1525	1287	1998	1574	1291
FEM model [Hz]	1000	920	860	1140	1000	960
Length correction [cm]	8.0	7.3	6.7	6.8	6.9	5.8

Table 4.4: Comparison between the pipe resonance theory and the FEM computation of the summer tire's groove resonance frequencies on the flat track

	With resonator			Without resonator		
Tire Load [N]	2400	3600	4800	2400	3600	4800
Pipe theory [Hz]	2238	1784	1459	2237	1821	1478
FEM model [Hz]	1060	1000	930	1240	1100	1020
Length correction [cm]	8.0	7.1	6.6	6.4	6.5	5.8

Drum curvature influence on the groove resonance frequency

As the frequency locations of the measured groove resonance frequencies matched the simulated ones for the summer tire, the FEM model is now used to study the influence of drum curvature on the groove resonance frequency. The frequency shift of the main fundamental resonances (see resonance shapes in Fig. 4.15) between the model on the flat track and on the inner drum is used to study the influence of drum curvature. As depicted in Fig. 4.19, the resonance frequencies on the flat track are always higher than the frequencies on the inner drum because drum curvature increases the contact patch length. There is however no clear trend for the summer tire and for the winter tire transverse resonance. In average, the fundamental groove resonance frequency of the summer tire decreases by 78 Hz because of the drum curvature.
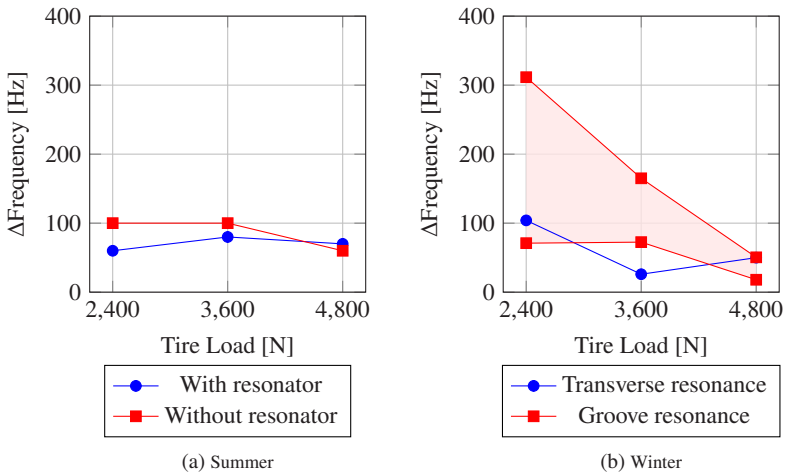
Figure 4.19: Drum curvature influence on the frequency shift of the computed groove resonance frequencies of the summer and the winter tires. The corresponding vibration shapes can be seen in Fig. 4.15.

With increasing tire load, the winter tire footprint will change its shape from an ellipsoidal to a square form (see Fig. 1.1). The higher the tire load, the longer the grooves will be. As the contact patch length increases with tire load, the ratio between the number of long grooves and number of short grooves

also increases. The resonance contribution of the short grooves is therefore not seen on the computed groove resonance spectrum. On the contrary, for a low tire load of 2400 N, the number of short grooves is equivalent to the number of long grooves, leading therefore to a relative higher contribution of the high-frequency groove resonances on the flat track. The influence of drum curvature counteracts this effect, as it prolongs the footprint at both sides and therefore extends the length of the shorter grooves. This explains the funnel evolution of the red curve in Fig. 4.19b.

The frequencies of the transverse groove resonance and of the longest grooves, just like the summer tire fundamental resonances, show no clear dependency upon tire load. In average, drum curvature decreases these resonance frequencies by 57 Hz. The testing conditions for tire approval tests according to R117 require an average tire load equal to 75 % of the tire load index. For the tires tested in this research work, this represents a tire load of 4525 N for the summer tire and 4930 N for the winter tire. According to Fig. 4.19, this corresponds to a tire load domain where the smallest span of frequency shift due to drum curvature is observed, which suggests a good transferability of the results from the inner drum to measurements on a flat track. With acoustic measurements in laboratory conditions inside an inner drum coupled with a FEM model of the groove resonance phenomenon, drum curvature influence on the groove resonance frequency can be computed and corrected. The groove resonance frequency of different tread pattern can therefore be estimated as if rolling on a flat track.

An appropriate estimation of the groove resonance frequency of a tire rolling on a flat track is essential to optimize noise performance of tread patterns for tire approval tests. As the tread pattern excitation frequency increases linearly with the speed, there are critical speeds at which the tread pattern harmonics will cross the groove resonance frequency, which could lead to a higher level of TiRN [8]. This interaction is depicted in Fig. 4.20 for the summer tire on the inner drum only. The tread blocks of the summer tire have a length varying between 15 mm and 25 mm, which leads to a broadband tread impact noise depicted with the red shaded area on Fig. 4.18a. The computed groove resonance frequencies at a tire load of 4800 N do not depend on the speed and are depicted using the blue shaded areas.

The driving speeds where these two shaded areas cross each other is considered as critical. A summary of the critical speeds is given in Fig. 4.20b. The most

(a) Drum - 4800 N
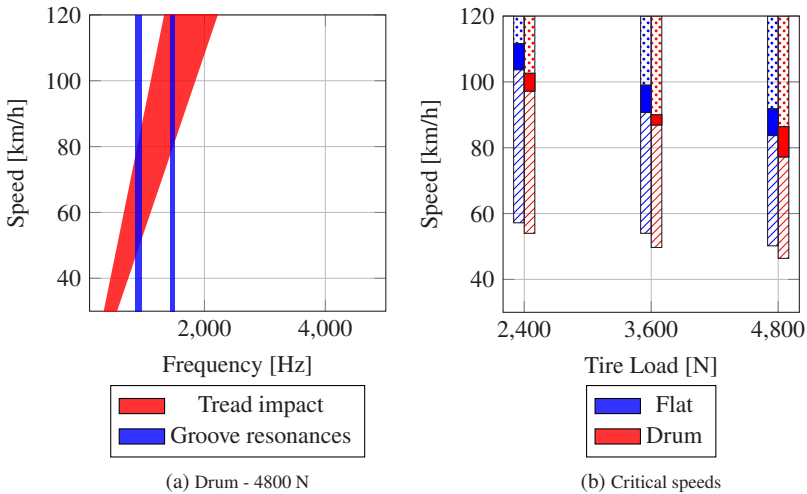
(b) Critical speeds

Figure 4.20: Drum curvature influence on the critical speeds for the summer tire. The dashed area corresponds to an interaction between the fundamental groove resonance and the tread pattern noise. The dotted area corresponds to an interaction between the second harmonic of the groove resonance and tread pattern noise. The filled area corresponds to an interaction between both groove resonance harmonics and tread pattern noise.

critical speed domain is when the fundamental groove resonance and its second harmonic coincide with the tread pattern noise frequencies. This is illustrated in Fig. 4.20b with the filled areas. As the groove resonance frequencies are underestimated inside the inner drum due to drum curvature, the critical speeds are also underestimated. In average, simulations performed with drum curvature (diameter of 3.8 m) lead to an underestimation of the critical speeds by 7.4 % compared to the simulation results on a flat track.

4.2.5 Summary and consequences for a low-noise tire-road pairing

The contribution of groove resonance to TiRN depends mainly on the texture roughness orientation. As shown in Fig 4.5, standardized ISO 10844 test tracks

must have a MPD between 0.3 mm and 0.7 mm and a skewness between −1.3 and −0.8. On the contrary, public roads have a MPD mainly concentrated between 0.7 mm and 1.4 mm. The texture orientation is negative but varies greatly between −1.4 and 0, with 50 % of the roads having a skewness between −0.8 and −0.4. If these values would have been reported in Fig. 4.11, results obtained on ISO 10844 test tracks would lie around the point Asphalt 0/5, where a significant increase of groove resonance noise is observed. On the contrary, measurements on public roads would lie between the points Concrete 0/16 and SMA 0/8, where the relative contribution of groove resonance to TiRN is neutral or decreased due to increasing voids inside the road surface. By extrapolating measurement results from the inner drum to real road surfaces, the contribution of groove resonance to TiRN might be higher on ISO 10844 test tracks than on public roads.

An efficient way to mitigate groove resonance noise would be to build roads with a high texture amplitude oriented negatively. This could lead to interconnected voids which would prevent a good sealing of air between the tire and the road and therefore reduce groove resonance noise. Increasing tire load seems also to be effective to decrease the contribution of groove resonance to TiRN on such tracks. For very smooth roads such as ISO 10844 test tracks, a positive orientation is beneficial to reduce groove resonance noise. Although groove resonance noise of tires with circumferential grooves does not seem to be strongly affected by tire load, tires with V-shaped tread pattern should have the smallest possible number of resonating grooves inside the contact patch. For a given tire load, this could be achieved by reducing the contact patch length and therefore by choosing a tire with a load index much higher than the effective tire load.

Computing the groove resonance frequency should be done for each iteration of the tread optimization process in order to avoid that critical speeds are created in the speed domain of interest. For a reduction of traffic noise in urban areas and its surroundings, this would cover a speed range between 30 km/h and 90 km/h. This can be done by using a static FEM model of the air volume surrounding the tire. This model delivered very adequate results for tires with circumferential grooves. The pipe resonance theory greatly underestimates the groove resonance frequencies because of the influence of the horn built between the tire and the road surface. This is generally realized using length corrections. However, the FEM results showed that these length corrections

greatly depend on tire load. The computation of the tire deformed geometry is therefore needed for each tire load, which should be realized prior to each iteration of the tread pattern optimization.

If measurements are performed inside a drum during the development process to validate a tread pattern design regarding its acoustic performance, the critical speeds might be underestimated by approximately 7.4 %. An opposite effect should also be observed with measurements on outer drums. Drum curvature should there lead to a reduction of the contact patch length and therefore to an overestimation of the critical speeds. The influence of drum curvature and tire deformation on the groove resonance frequency can be quantified easily using a FEM model based on footprints. The tread pattern and groove design can therefore be easily optimized numerically and tested in controlled laboratory conditions. Obtained results can then be transferred to field measurements using this curvature correction.

4.3   Road surface influence on tire-road noise

The influence of the road surface and the operating parameters on groove resonance noise has been studied in the previous section. The same analysis will now be repeated for the total TiRN, in the near field range as well as in the far field range.

4.3.1 Near field measurements on the inner drum test bench

Measurements in the near field using the CPX method enable a sound analysis around the tire. In this section and due to the high number of regressions performed, only the interpretation of the statistical results are presented. All statistical results can be seen in Appendix A.2.3.

The first result is the consistency of the retained parameters and of the goodness of fit. The average coefficient of determination equals 98 % and the prediction error oscillates between 0.7 dBA and 1.3 dBA. The significant parameters retained by the generalized regression are almost identical for all tires and for all microphones (see Table 4.5). For different tires and different microphones, the regression coefficients have the same sign and the same order of magnitude which is a sign that the results were robustly predicted and that overfitting was avoided. Using the correlation analysis presented in section 4.1.2, these parameters can be clustered in three groups:

- Operating parameters: nonlinear increase of TiRN noise with increasing speed

- Roughness amplitude: TiRN increases when the MPD increases

- Interaction between roughness amplitude and texture orientation: g*Ltx FPC1 or MPD*Absorption

As presented in section 1.2.1, the influence of driving speed is modeled using a logarithm function. The non-linear increase of TiRN with increasing speed is modeled here using a positive slope for its linear influence and a negative slope for its quadratic influence. Results obtained through the double lasso algorithm

Table 4.5: Significant parameters retained by the double lasso for measurements inside the inner drum test bench

	Parameter	Leading	Trailing	CPX-middle
Ribbed-Slick	Speed & Speed^2	x	x	x
	g*Ltx FPC1	x	x	
	MPD	x	x	x
	Ltx FPC1^2		x	x
Summer	Speed & Speed^2	x	x	x
	g*Ltx FPC1	x	x	x
	MPD	x		x
Winter	Speed & Speed^2	x	x	x
	g*Ltx FPC1	x		
	Absorption*MPD		x	x
	MPD			x
	Load		x	

are therefore consistent with literature results, as the logarithm function also has a degressive gradient.

Concerning the interaction between roughness amplitude and texture orientation, the correlation analysis presented in section 4.1.2 indicates that absorption coefficient and RSK are almost perfectly correlated (see Fig. 4.4b). This explains that either *g*Ltx FPC1 or MPD*Absorption are retained by the algorithm. This interaction is seen as not significant only for the ribbed-slick tire at the CPX-middle microphone. Otherwise, the interaction between roughness amplitude and texture orientation has a very significant influence on TiRN in the near field range.

The influence of this interaction is depicted in Fig 4.21. The increase of TiRN for a smooth road with a negative orientation (upper right part of Fig. 4.21a) or with a high absorption (upper left part of Fig. 4.21b) is a consequence of the statistical results extrapolation. As no tracks with these specific characteristics could be built inside the inner drum test bench, the analysis will focus around the measurement points depicted in Fig. 4.21.

(a) Interaction Roughness/Orientation   (b) Interaction Roughness/Absorption
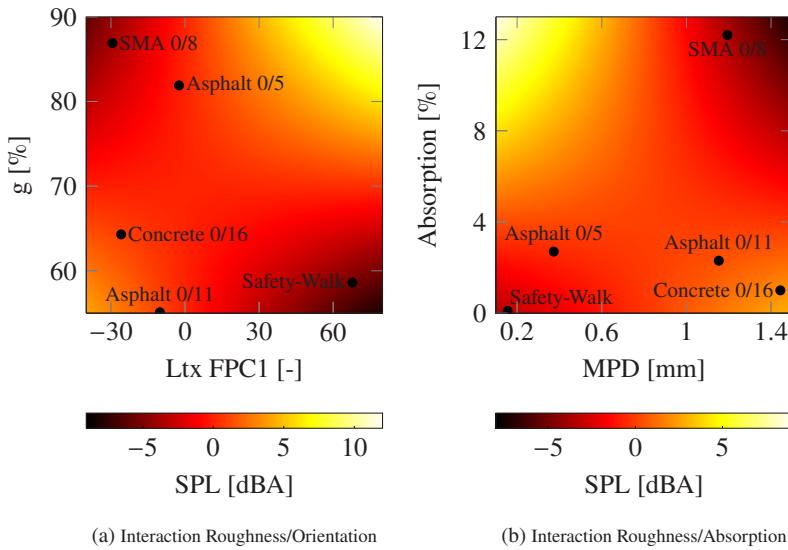
Figure 4.21: Influence of the interaction between the road surface roughness and its orientation on TiRN measurements inside the inner drum test bench

Increasing the shape factor g towards one is a very efficient measure to reduce TiRN, especially if the road surface has a high roughness level. Increasing g will lead to a negative oriented texture, which is very useful to reduce the road impact mechanism. Combined with a high MPD (or a low Ltx FPC1), this induces connected voids and therefore a higher absorption level which is also beneficial to mitigate TiRN.

If texture orientation goes toward positive values, then it is beneficial to reduce the texture roughness level. The influence of texture orientation on a surface with a low roughness level is however not clear because only the measurement points on Safety-Walk are there to support this theory. Texture orientation might play an important role in TiRN generation when the roughness level is above a certain threshold. This minimum roughness level would define the transition point where the road impact phenomenon takes over as the main TiRN generation mechanism. According to Fig. 4.21a, this transition point would correspond to the vertical line where Ltx FPC1 equals zero. This

corresponds almost to the measurement point Asphalt 0/5, which has a MPD of 0.37 mm. For the winter tire, the interaction between the MPD and the absorption coefficient sometimes replace the interaction between the shape factor g and Ltx FPC1 (see Fig. 4.21b). The turning point is here observed at a MPD of 0.87 mm.

The tires react differently to the roughness level. The regression coefficients at the leading edge for the MPD and for the interaction between roughness amplitude and its orientation are always greater for the ribbed slick tire (see Tables A.41, A.44 and A.47). The ribbed-slick tire is therefore much more sensitive to variations of the roughness amplitude than the summer and the winter tires. As the ribbed-slick tire has no tread pattern, the major contributor to TiRN should be road impact noise and air pumping noise. It is therefore logical to see a stronger relationship between the MPD and TiRN for the ribbed-slick tire. Road surface influence is lessened for the serial tires because of the contribution of tread impact noise. Although the roughness amplitude/orientation interaction is very significant for the winter tire, the MPD alone has a significant influence on noise emission of the winter tire only at its sidewalls. This could be explained by the relative softer rubber compound which transmits less vibrations to the tire structure and therefore reduce the contribution of road impact to TiRN.

From these results, it must be clarified whether this turning point lies within the MPD tolerances set in the ISO 10844 standard. If this is the case, this would mean that the road impact phenomenon would be the main TiRN contributor above this critical roughness value. TiRN could be mitigated by keeping the texture orientation negative. According to the results from the groove resonance analysis, this would also be beneficial to reduce groove resonance noise. Below this critical roughness level, tread pattern and air pumping noise would be the main noise source contributors. These results need to be confirmed and refined using measurements in the far field with a larger measurement database. This will be presented in the following section.

4.3.2 Far field measurements on public roads and ISO 10844 test tracks

Within this section, several questions need to be answered. First, it must be stated whether the parameters used in the ISO 10844 standard are suitable to explain noise variation measured on a sufficient number of standardized test tracks. If not, complementary parameters are to be found and their influence on TiRN generation have to be explained. The roughness transition point presented in section 4.3.1 needs to be further investigated, for ISO 10844 test tracks and for public roads. Finally, significant road surface parameters for the mitigation of TiRN on public roads need to be identified. The statistical results need to be physically explained in term of TiRN generation and propagation.

This will be realized using a four-step analysis. The method presented in Fig. 3.4 will be repeated by performing the statistical analysis on the ISO 10844 test tracks only or on the entire TiRN measurements data set. As characterizing parameters, either the MPD and the absorption coefficient or the complete parameters database will be used. If the retained parameters by the double lasso are different, this means that the parameters used in the ISO 10844 standard fail to explain most of the noise variation. They would therefore not be adequate to explain the road surface influence on TiRN emission.

Comparing and interpreting the four models will help to confirm or infirm the results obtained in the near field range. To facilitate the results presentation, the database containing only the MPD and the absorption coefficient will be denoted as "ISO parameters". The group containing all the road surface parameters will be abbreviated to "All parameters". An exhaustive overview of the statistical results for the measurements on ISO 10844 test tracks only is given in Appendix A.2.4, while the regression results of all field measurements are detailed in Appendix A.2.5.

Results on ISO 10844 test tracks only

The influence of the chosen parameter database on the prediction error and the goodness of fit is presented in Fig. 4.22. By using all parameters, the prediction error is constant for all tires and oscillates around 0.5 dBA. If only the ISO parameters are retained, the prediction error is different if the tire is a serial tire

or not. For the ribbed-slick tire, the prediction error lies around 0.9 dBA while it varies between 0.6 dBA and 0.7 dBA for the summer and the winter tires. By using all parameters, the coefficient of determination increases in average by 10 %.

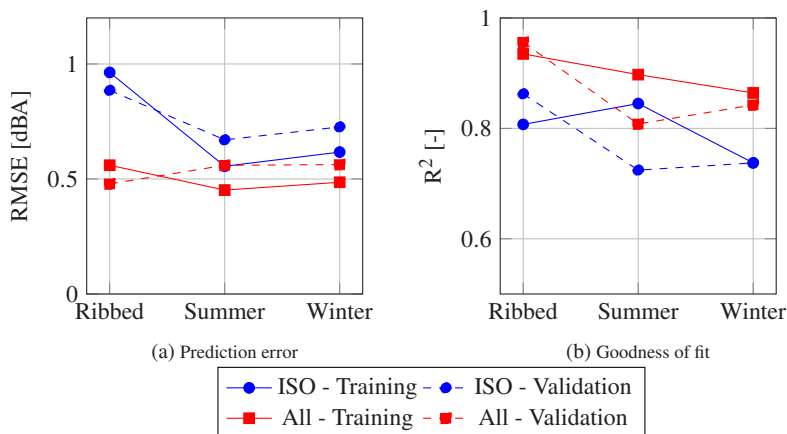(a) Prediction error   (b) Goodness of fit

Figure 4.22: Comparison of the parameters data set on the goodness of fit and the prediction error on ISO 10844 test tracks. The drawn lines have no mathematical meaning and are used as guide to the eye

The influence of the ISO parameters for all tires is depicted on Fig. 4.23. The results are plausible for the ribbed-slick and the summer tires. For the ribbed-slick-tire, an increase of MPD will lead to an increase of TiRN. For a free-rolling tire without tread pattern, air pumping and road impact noise are expected to be the main noise source contributors. Air pumping noise could be a major contributor at very low MPD values, where the ribbed-slick tire is able to seal all air cavities from the road surface. By further increasing the MPD, this noise source should mitigate in favor of road impact noise.

For the summer tire, it seems there is a turning point at a MPD around 0.5 mm, where the noise level increases again by reducing the road surface roughness. This could be due to a higher contribution of air pumping and tread pattern noise, while road impact noise becomes the predominant TiRN contributor for MPD values above 0.5 mm. For both tires, the noise increase at low MPD and absorption values above 5 % is a consequence of the extrapolation of the
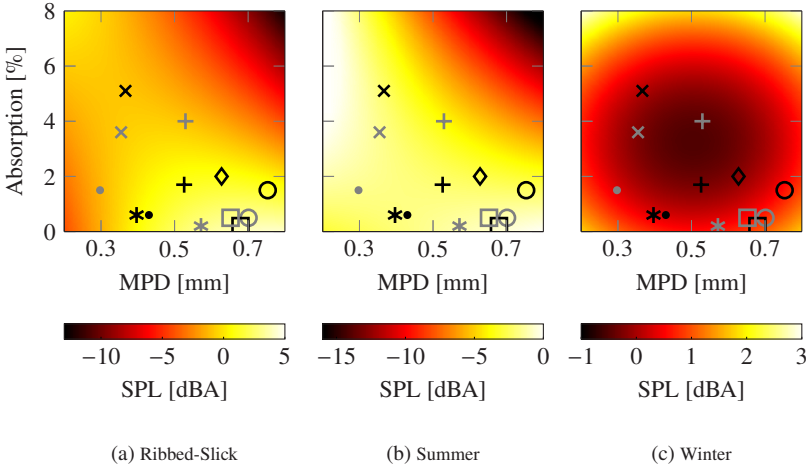
105

(a) Ribbed-Slick (b) Summer (c) Winter

Figure 4.23: Influence of the significant road surface parameters interactions on TiRN on ISO 10844 test tracks using parameters from the ISO 10844 standard only. The relationship between the symbols and the test track number is given in Table A.6

statistical model. A further reduction of TiRN would be expected by increasing the road surface absorption. However, no measurement points are available to support this theory.

For the winter tire, the results are not conclusive. Although the MPD and the absorption are retained by the double lasso, the results can not be physically interpreted. The TiRN fluctuations of the winter tire can not be explained by the variation of MPD and the absorption coefficient.

The influence of all parameters on TiRN emission on ISO 10844 test tracks is shown in Fig. 4.24. As a perfect correlation exists between RMS and Abbott FPC1, the effective value of the surface roughness was replaced by Abbott FPC1 for the winter tire in Fig. 4.24c. Two interactions with the roughness amplitude are highly significant. The parameter describing the roughness amplitude is either the MPD or the first FPC of the Abbott curve. Results from Fig. 4.24 show the same pattern for all tires, which is an improvement compared to the model presented from Fig. 4.23 where only the ISO parameters where used.
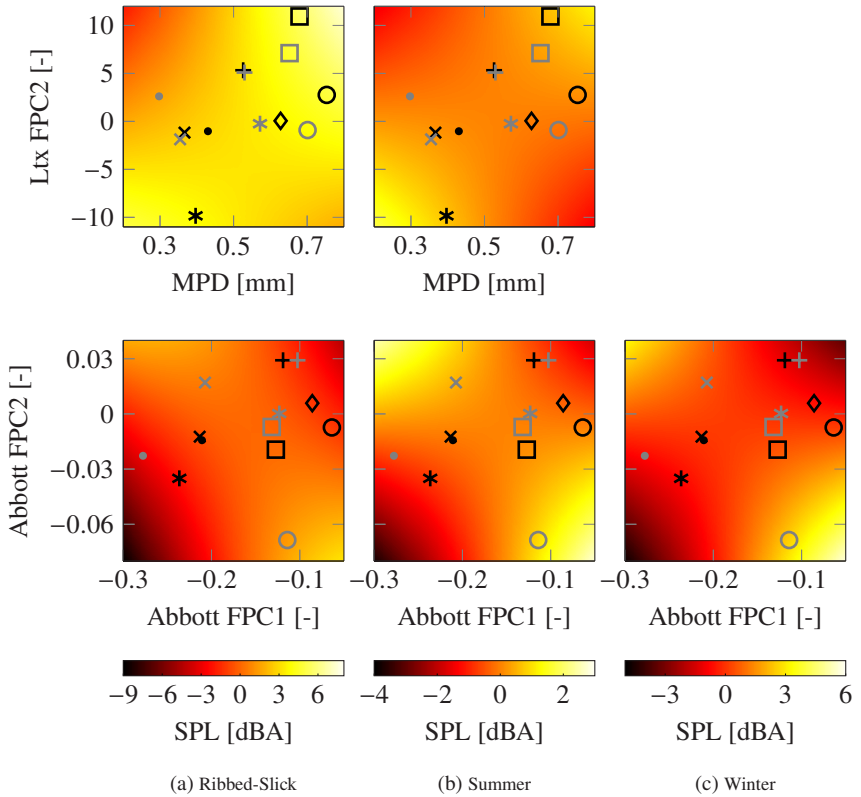
Figure 4.24: Influence of the significant road surface parameters interactions on TiRN on ISO 10844 test tracks using all parameters from the global road surface descriptors set. The relationship between the symbols and the test track number is given in Table A.6

Some results from the model with ISO parameters are confirmed, and other relevant road surface descriptors appear. Here again, there is a critical roughness value where the roughness distribution function (Abbott FPC2) and the texture spectrum (Ltx FPC2) play an important role in TiRN generation. This turning point is found when MPD equals 0.53 mm or when Abbott FPC1 reaches 0.15. As there is a very strong linear relationship between these two parameters (r

= 0.96), the equivalent MPD value can be estimated with a linear regression. This equates to a MPD of 0.54 mm.

Design guidelines for a low-noise ISO 10844 test track

Several goals can be set for the design of an ISO 10844 test tracks. For a scientific purpose in order to optimize the tread pattern design, it is interesting when slight differences in the tread design or in the tread compound can be detected using coast-by measurements on a standardized test track. To do so, the span of the measured SPL values between each tire design must be maximized. This will not be done in this section as only three tires were tested in this work, which is not representative enough. Understanding interactions between road surface properties and the different mechanisms contributing to TiRN is also important. The following interpration aims at designing a low-noise standardized test track by reducing different sub-components of TiRN. A similar approach might be used to design a standardized test track for a specific purpose, such as enhancing groove resonance noise.

According to the results from Fig. 4.24 and from Tables A.51, A.53 and A.55, a quiet ISO 10844 test track should have:

- An absorption coefficient near the ISO 10844 limit of 8 %

- Either a low MPD with a negative Abbott FPC2 and a positive Ltx FPC2

- Or a high MPD with a positive Abbott FPC2 and a negative Ltx FPC2

- A low SRT value

The influence of absorption could be expected, as an absorption increase will disturb the causal loop between noise generation and noise propagation.

A high MPD with a negative Abbott FPC2 (lower right part of Fig. 4.24b) corresponds to a rough texture with a texture orientation less negative than the average of all other test tracks. This will tend to increase the road impact phenomenon. On the contrary, a low MPD with a positive Abbott FPC2 (upper left part of Fig. 4.24b) depicts a smooth road surface oriented negatively. This will tend to increase tread pattern noise. As the roughness level is very low, the probability that air pockets inside the asphalt layer are connected with each

other is very low. This could lead to an increase of groove resonance and air pumping noise.

By keeping the roughness amplitude at a low level and by shifting the roughness distribution function towards positive values (reduction of Abbott FPC2), a reduction of TiRN can be achieved (see lower left part of Fig. 4.24b). This can be explained by a reduction of air pumping and groove resonance noise, which confirms the results on Safety-Walk obtained in section 4.2.5. The benefits of a combination smooth texture/positive orientation is not as high for the ribbed-slick tire as it is for the serial tires. This further indicates that groove resonance noise could be a major noise source on ISO 10844 test tracks.

The last possible combination is a high roughness oriented negatively (upper right part of Fig. 4.24b). As expected, this combination leads to a reduction of noise emission because the surface roughness is oriented negatively. This leads to a reduction of road impact noise while potentially increasing the absorption coefficient by increasing the void content. According to the results from the groove resonance analysis, this amplitude/orientation combination leads to a neutral influence on groove resonance noise.

For small MPD values around 0.3 mm, a positive value of Ltx FPC2 leads to a reduction of TiRN. This corresponds to a spectra with more macro-roughness than mega-roughness, with a cut-off wavelength at 31.5 mm. For MPD values close to the upper tolerance limit from the standard, it could be also beneficial to have a flatter roughness spectrum. Although increasing the mega-roughness level could lead to an increase of the tire vibrations, it seems that a high MPD with a high texture level at wavelengths between 4 mm and 8 mm is a poor combination in term of TiRN generation.

To see whether such a test track can be built, another correlation analysis is performed between these relevant parameters. The correlation between the MPD and Abbott FPC2 is very weak ($r = -0.13$) and the correlation between the MPD and Ltx FPC2 is moderate ($r = 0.47$). The highest potential for reducing the road surface contribution to TiRN is therefore to design the Abbott curve, so that the first two FPC are negative (lower left corner of Fig. 4.24). A further reduction possibility is to tune the roughness spectrum so that the roughness profile has most of its spectrum concentrated at wavelengths between 14 mm and 16 mm.

Results on all roads

The analysis presented before on the ISO 10844 test tracks only is now repeated with the measurements on all roads. The prediction quality is fairly unrelated to the parameters for the ribbed-slick tire (see Figure 4.25). Prediction error oscillates between 1 dBA and 1.1 dBA while the coefficient of determination equals 85 %. For the serial tires, using all parameters enables an average reduction of prediction error of approximately 0.1 dBA while the coefficient of determination improves by 7 % in average.

(a) Prediction error   (b) Goodness of fit

ISO - Training - ISO - Validation
All - Training - All - Validation
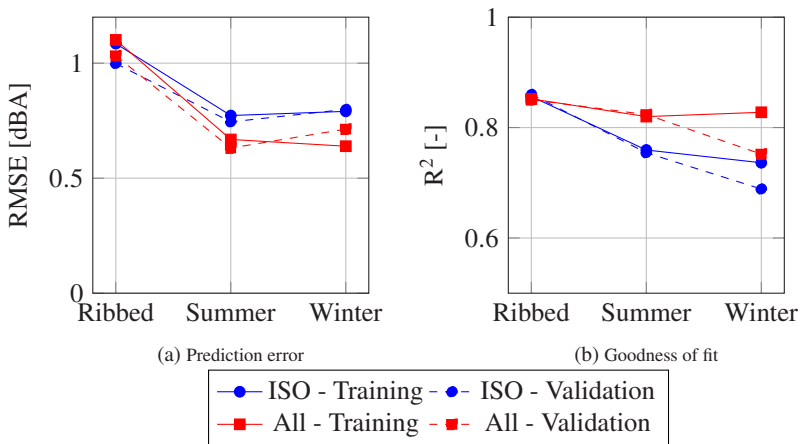
Figure 4.25: Comparison of the parameters data set on the goodness of fit and the prediction error on all roads. The drawn lines have no mathematical meaning and are used as guide to the eye

Although the statistical model using all parameters seems to better fit the measurements for the serial tires, the number of parameters retained by the algorithm needs to be taken into account. While the model with the ISO parameters uses three variables related to the road surface (MPD, Absorption and MPD^2) to describe the variation in TiRN for both serial tires, the model using all parameters needs ten parameters for the summer tire and nine parameters for the winter tire to achieve a slightly better prediction. Moreover, the MPD or the absorption coefficient always are the most significant parameters for all tires (see Tables A.56, A.58 and A.60). This shows that for the given data set,

the parameters from the ISO 10844 standard are adequate enough to predict TiRN variation with a prediction error of 0.8 dBA for serial tires and 1 dBA for the ribbed-slick tire.

The influence of ISO 10844 parameters on TiRN emission of the three tires is depicted in Fig. 4.26. The evolution for both tires are very similar. The main difference for the ribbed-slick tire is the significance of Absorption[2] which induces a curvature in the contour lines of Fig. 4.26a. This quadratic effect is mainly due to road surface #15 which is the road surface with the highest absorption coefficient. If the analysis is repeated without the measurement points realized on this test track, the leverage of Absorption[2] is reduced so that the turning point of the contour line for the ribbed-slick tire is moved outside the measured absorption values. This leads to a monotonic reduction of TiRN with increasing absorption coefficient.
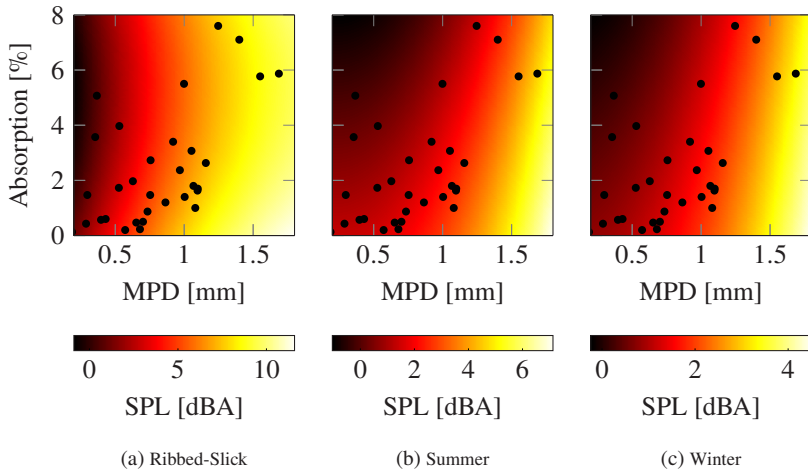
Figure 4.26: Influence of the significant road surface parameters interactions on TiRN on ISO 10844 test tracks. The retained parameters are the parameters from the ISO 10844 standard: the MPD and the absorption coefficient.

An explanation for the similar evolution of TiRN over the MPD for all tires is that noise due to the road impact phenomenon is predominant from a certain level of roughness on. It was supposed from the results from Fig. 4.24 on the ISO 10844 test tracks that there is a critical roughness level, where the

road impact influence prevails over the other TiRN contributors (e.g. tread pattern, groove resonance and air pumping noises). According to the results from the analysis on groove resonance noise presented in section 4.2.3, groove resonance noise would contribute more to TiRN on smooth negative or rough positive road surfaces. Figure 4.5 shows that public roads have a median MPD around 1 mm with a negative texture orientation (median RSK of −0.5). Standardized test tracks have a smoother and more negative oriented texture (MPD around 0.5 mm and RSK around −1). Such a roughness/orientation interaction leads to a reduced contribution of groove resonance noise to TiRN on public roads compared to ISO 10844 test tracks. This is confirmed here again for all tires.

For the ribbed-slick tire, MPD influence on TiRN emission is first linear from the low to medium MPD range and then declines for very high MPD values. On the contrary, MPD influence on TiRN for the serial tires has a slope which increases with the MPD. For the summer tire, there is also a turning point at a MPD value of 0.2 mm. This comforts the hypothesis that other phenomena such as tread impact noise and groove resonance noise are predominant at low MPD while road impact noise becomes the predominant contributor to TiRN above a particular roughness amplitude.

4.3.3 Summary and discussion

Results have been presented in the near field range and the far field range to describe road surface influence on TiRN. For groove resonance noise, the interaction between texture orientation and roughness amplitude plays a major role in TiRN emission.

The main advantage of the inner drum test bench compared to field measurements is that every parameter can be controlled so that road surface influence on TiRN and its interaction with the operating parameters can be isolated. Compared to the road surfaces from the field measurements which mainly have a negative orientation, the inner drum surfaces enabled the study of rough surfaces with positive and negative orientation. Although the number of tested surfaces is not sufficient to generalize this observation, measurements performed inside the inner drum showed that total TiRN as well as groove resonance noise depends on texture orientation. This interaction is more im-

portant for the ribbed-slick tire than for the serial tires, because TiRN of a tire without tread pattern is dominated by road impact noise and air pumping noise. A smooth road texture will globally reduce road impact noise but could increase air pumping noise if the texture is oriented negatively because the tire would roll over non connected cavities. On the contrary, a rough negative texture could lead to connected cavities, a higher absorption and to a reduction of air pumping noise, while keeping road impact noise at a low level because the texture is not oriented towards the tire.

It seems there is always a critical roughness level, where texture orientation can be used to mitigate TiRN. For groove resonance noise, this critical point corresponds to a MPD around 1 mm. For total TiRN, the transition point is not clearly defined, as it depends upon the parameters retained by the double lasso algorithm. If the first FPC of the texture spectrum and the shape factor g are retained, this corresponds to a negated Ltx FPC1 (i.e. a MPD around 0.4 mm). If MPD and the absorption coefficient are used, a transition point is observed at a MPD of 0.87 mm. These transition points are observed at critical values, as they overlap with the MPD-tolerances from the ISO 10844 standard. Tuning the orientation of the road surface texture might be an effective way to mitigate TiRN. For a very smooth road surface, a positive texture orientation seems to be beneficial while a negative orientation is needed if the road has a high roughness level.

These results are confirmed by the analysis of the far field measurements. The double lasso algorithm shows that others parameters than MPD and the absorption coefficient are required to explain the noise variance between different ISO 10844 standardized test tracks. The shape of the roughness distribution function and the texture roughness spectrum seem namely to have a great influence on TiRN on standardized test tracks. A possible explanation is the road surface influence on the trade-off between different TiRN generation mechanisms. A low roughness amplitude will tend to favor the generation of tread impact, groove resonance and air pumping noise. By tuning the texture orientation, it is possible to reduce some of them and therefore reduce globally TiRN.

Above a certain roughness level, it seems that road impact noise becomes the main contributor to TiRN, which would be the case for most public roads. According to the statistical analysis performed in this research work, the parameters from the ISO 10844 standard are namely adequate enough to describe

road surface influence on TiRN. It can be concluded that the influence of texture orientation is high mainly on smoother roads, where road impact noise is not the only major generation mechanism of TiRN. Public roads and standardized test tracks have globally a negatively oriented texture, so that the influence of a positive texture could not be studied. The results presented in section 4.2.5 also showed that texture orientation has a very significant influence on the contribution of groove resonance to TiRN.

Based on the measurement data used in this research work, additional parameters are needed besides the MPD and the absorption coefficient to describe the relevant road surface characteristics of standardized test tracks for tire approval tests. Reducing the inter-site noise variation is important to ensure results reproducibility and the consistency of noise levels depicted on the tire labeling. It should be possible to use a correction factor to correct the influence of texture spectrum and roughness distribution function on TiRN.

5 Summary

This research work focuses on the quantification of road surface influence on tire-road noise emission. Due to the constant increase of people affected by traffic noise, the European regulation R117 that deals with the required tire characteristics found on the tire label has decreased the maximum authorized noise level emitted by tires in two stages between 2014 and 2018. For the nominal tire width used in this work, this corresponds to a further reduction of 4 dBA compared to the previous version. Developing quieter and quieter tires will become more and more important for automotive manufacturers. Noise limits for the homologation of passenger cars (where tire-road noise is one of the main contributors, especially for electrified vehicles) will also be reduced by 3 dBA between 2016 and 2026. This work aims at generating more knowledge to understand which road surface characteristics are relevant to reduce noise emission of tires. Increasing road surface absorption is a well known-possibility. This work focuses on road surfaces with a low absorption coefficient, which is the type of surface used for tire approval tests. A second goal was to see whether the test tracks used for tire approval tests are representative of real road surfaces and if the parameters used to describe their characteristics are adequate enough to explain the inter-site noise variation.

After an introduction to present the state of the art, the theoretical background required to understand this work is summarized in the second chapter. The different mechanisms contributing to TiRN generation and propagation are presented, as well as the different road surface descriptors used in this research work. The most important information about the ISO 10844 standard are then summarized. Several statistical methods are used to study the influence of the road surface on TiRN emission. Statistical basics are given in order to understand the analysis procedure developed in this work. First the reduction of multidimensional data to scalars using FPCA is detailed, followed by the automatic variable selection algorithm used during the multiple linear regression.

The next chapter deals with the different methods used to acquire measurement data and to exploit them. The acoustic measurements were performed either in the near field inside an inner drum test bench or in the far field using coast-by measurements on standardized test tracks and public roads. The different measuring devices used to measure the road surface roughness, absorption and grip level are also presented. After detailing the measurement analysis procedure from the raw measurements to the statistic results, a short overview of the studied tires and road surfaces is given.

The last chapter presents the main results from experimental, numerical and statistical analyses that quantify the influence of the operating parameters and the road surface on tire road noise and some of its generation mechanisms. Other phenomena such as tire abrasion, rolling resistance, wet grip or dynamic handling are hereby not studied. First the results from the function principal component analysis are presented. This method enables the reduction of amplitude roughness spectra and Abbott curves to two or three scalar descriptors that describe the main modes of variations of the curves. A better understanding of the physical meaning of each parameter is achieved with a correlation analysis between all road surface scalar descriptors. This pool of parameters is then used to identify the significant road surface parameters and to quantify their influence on tire-road noise emission. The first analysis is performed on groove resonance noise. Filling the grooves with acoustic foam enables the isolation of this tire-road noise generation mechanism. The influence of driving speed, tire load and road surface on the groove resonance noise spectrum and noise level was analyzed for two tires with usual tread pattern shapes: a summer tire with circumferential grooves and a winter tire with a V-shaped tread pattern. In average, groove resonance contributes to 1.7 dBA to TiRN. This contribution increases with the driving speed and varies between 2 dBA and 4 dBA at speeds between 50 km/h and 90 km/h. Although filling the grooves with foam is not a viable industrial way to reduce tire-road noise, innovative solutions in tread pattern design and groove ventilation could help to drastically reduce noise emission of tires and fulfill the requirements from the R117 and R51.3 regulations.

To ensure that the measured noise variation does correspond to groove resonance noise, a FEM model was developed using footprints to compute the groove resonance frequencies and compare it to the measured ones. This method showed excellent results for the summer tire with circumferential

grooves and enabled the quantification of the drum curvature influence on the groove resonance frequency. This also confirmed that the foam glued between the tread blocks mainly affected groove resonance noise and not the other mechanisms generating tire-road noise. This model enabled the identification of the groove resonance vibration shapes and the quantification of the tire load and the drum curvature influence on the groove resonance frequencies. With this approach, the critical speeds at which the tread impact harmonics cross the groove resonance frequencies can be identified. In average, the curvature of the inner drum used in this work will lead to an underestimation of the groove resonance frequency and the critical speeds of 7.4 %.

The shape of the roughness amplitude spectrum also has an influence on groove resonance noise. If the roughness is concentrated on the macro-roughness domain, groove resonance noise increases because the excitation spectrum of the road impact coincides with the groove resonance frequencies. The most important road surface descriptor influencing groove resonance is the interaction between roughness amplitude and texture orientation. Although groove resonance excitation is influenced by the roughness spectrum, texture orientation can prevent the resonance to take place if interconnected voids are present in the road surface. This can be achieved with high roughness level coupled with a negative texture orientation. A smooth negative road surface will on the other hand offer a better sealing of the tire on the road and therefore better resonating conditions for the pipe network. The influence of this interaction is also very significant for global tire-road noise in the near field range and can be tuned to mitigate noise emission. Tuning the texture orientation will enable a balancing between road impact noise and other mechanisms generating tire rolling noise. According to the statistical results, a low-noise road surface design would be achieved with a negative-oriented rough surface or with a smooth surface oriented towards the tire.

The results obtained in laboratory conditions can be transferred to field measurements in the far field. In such conditions, texture orientation also has an important influence on noise emission of tires, especially on smooth surfaces like standardized ISO 10844 test tracks. In terms of tire-road noise emission, the regression performed on these tracks showed that several parameters not mentioned in the standard were identified as significant. A first parameter was proposed in the 2011 version of the ISO 10844 standard to explain the inter-site variation between different standardized ISO 10844 test tracks: the

END_T. A correlation analysis between the observed inter-site noise variation and the computed END_T showed that there is no clear relationship between the END_T and the measured inter-site noise variation. The inter-site variation can be further reduced by adding other parameters than the standard parameters used in the ISO 10844 standard (mean profile depth and absorption coefficient), some of which are used to compute the END_T. By using additional information from the roughness amplitude spectrum and the Abbott curve, the achieved prediction quality oscillates around 0.5 dBA. This corresponds to a reduction of the prediction error by 44 % for the ribbed-slick tire and by 20 % for the serial tires compared to the regression with the ISO parameters only. On the other hand it seems that parameters from the ISO 10844 standard are adequate enough to model the road surface influence on noise emission of tires rolling on public roads. The road impact is here the dominating generation mechanism of tire rolling noise.

With the statistical analyses of the relationships between tire-road noise and road surface characteristics presented in this work, a basis has been created towards a better understanding of the relevant road surface characteristics for tire-road noise mitigation. These results can be used to improve the design of standardized ISO 10844 test tracks in order to reduce inter-site noise variation, but also to optimize the road surface design in order to reduce noise in urban and rural areas. As the contribution of groove resonance to tire-road noise is quite high, especially at high speeds, the numeric and experimental methods presented in this work could be used to test prototype tread patterns and optimize it in order to reduce groove resonance noise.

6 Prospects

The measurements performed for this work focused on one point: finding the relevant road surface descriptors to reduce noise emission of rolling tires, especially on standardized test tracks. Maximizing the variance of coast-by noise levels between different tread patterns might be another objective for tire developers. A slight difference in tread pattern optimization or in tread compound could lead to a significant noise reduction on a specific ISO 10844 test track, but might also lead to almost identical SPL values on another standardized test track. To enable a better acoustic differentiation between different tread pattern designs, a further step would be to repeat the analysis performed during this work, but with a greater amount of tires. By predicting the standard deviation of tire-road noise based on the road surface descriptors, it would be possible to identify the relevant road surface parameters that highlights the tread pattern influence on tire-road noise and help choose the best tire design.

It was shown using measurements in the near and far field that the main contributors to tire-road noise might depend on the road surface roughness. A high roughness can for example lead to a predominance of road impact noise with a high contribution of groove resonance noise. On the contrary, a very smooth surface will enhance tread pattern noise and air pumping noise. These are however only interpretations from statistical results based upon the scientific literature. A better physical understanding of the coupling between these sub-components and the road surface properties might help designing low-noise tread pattern and road surfaces.

By tuning the cumulative probability distribution function, the roughness amplitude level and the roughness spectrum in a certain way, it was statistically shown that a quiet ISO 10844 test track could be built. Although all these parameters are rather uncorrelated, it would be interesting to study if building such a road surface profile is possible. This could be done by developing a road surface profile generator that can create different combinations of roughness

amplitude level, distribution function and texture spectrum. Using this profile as an input to a physical tire-road noise prediction model could help validating the statistic results obtained in this work.

Another approach would be to produce another data set to validate the results obtained in this work. The previously generated profiles could also be built on an outer drum test bench by using synthetic resin or through milling, to see in controlled laboratory conditions if the statistical results can be validated by another measurement data set. As every parameters can be controlled in such testing conditions, repeatability should be much higher than for field measurements. Such conditions should allow for a larger amount of tires tested and a broader analysis of parameters (controlled tire load, inflation pressure, temperature, etc.).

Unlike measurements performed in laboratory conditions, field measurements always induce a certain amount of uncertainty mostly due to weather or to driving reproducibility of the test driver. Based on the results from this work, it would be interesting to design a road surface that could be used for simulated coast-by measurements in semi-anechoic chambers. The ISO 362-3 standard suggests an indoor testing method to simulate accelerated pass-by measurements. By defining a standardized road surface which could be easily reproduced, all parameters could be monitored on the test bench and the problem of inter-site noise variation would be eliminated. Moreover, car or tire manufacturers would not be dependent on the weather to perform its approval tests. More research work is however needed in order to have a simulated pass-by noise procedure for free-rolling pass-by measurements.

Only the acoustic properties of roads were studied within this work. The design proposals to reduce noise on public roads and on standardized ISO 10844 test tracks might lead to a conflict of objectives between noise emission, rolling resistance and wet grip. A systematic analysis could be done to variate one parameter at a time and test its influence on tire-road noise. For example using the imprint method presented in [124] to keep the macro-texture constant but change the contact properties by using different materials for the road surface (e.g. concrete, different asphalt mixes, synthetic resin, etc.).

List of Figures

List of Tables

References

[1] Statista. Number of registered passenger cars in Europe (EU-28) from 1990 to 2017. https://www.statista.com/statistics/452447/europe-eu-28-number-of-registered-passenger-cars/. Accessed: 06.12.2019.

[2] European Environment Agency. Exposure of Europe's population to environmental noise. https://www.eea.europa.eu/data-and-maps/indicators/exposure-to-and-annoyance-by-2/assessment-4. Accessed: 06.12.2019.

[3] D. Ouis. Annoyance from road traffic noise: a review. *Journal of Environmental Psychology*, 21(1):101–120, 2001.

[4] W. Babisch. Road traffic noise and cardiovascular risk. *Noise and Health*, 10(38):27, 2008.

[5] G. Bluhm, E. Nordling, and N. Berglind. Road traffic noise and annoyance–an increasing environmental health problem. *Noise & health*, 6(24):43–49, 2004.

[6] J. Selander, M. E. Nilsson, G. Bluhm, M. Rosenlund, M. Lindqvist, G. Nise, and G. Pershagen. Long-term exposure to road traffic noise and myocardial infarction. *Epidemiology*, 20(2):272–279, 2009.

[7] M. Dittrich, F. de Roo, S. van Zyl, S. Jansen, E. de Graaff, and J. Sliggers. Triple a tyres for cost-effective noise reduction in europe. In *EuroNoise 2015 – 10th European Congress and Exposition on Noise Control Engineering*, Maastricht, The Netherlands, 2015.

[8] U. Sandberg and J. A. Ejsmont. *Tyre/Road Noise – Reference Book*. Informex, Kisa, 2002.

[9] UNECE. Regulation no. 117: Uniform provisions concerning the approval of tyres with regard to rolling sound emissions and/or to adhesion on wet surfaces and/or to rolling resistance, February 2016.

[10] U. Sandberg. Calibrating the iso 10844 test surfaces used for vehicle and tyre noise testing. In *Inter-Noise 2017 – International Congress and*

Exposition on Noise Control Engineering: Taming Noise and Moving Quiet, Hong Kong, China, 2017.

[11] T. Klesen. Literature review: Impact of a vehicle tire on tire road noise emission. Bachelor-thesis, Karlsruher Institut für Technologie (KIT), Karlsruhe, 2017.

[12] T. Gütschow. Literature review on the road pavement influence on the tire road noise. Bachelor-thesis, Karlsruher Institut für Technologie (KIT), Karlsruhe, 2017.

[13] S. Heinz. Investigations on noise emission of motor vehicles in road traffic. Technical Report UBA-FB 200 54 135, TÜV Nord Mobilität – RWTÜV Fahrzeug GmbH, 2005.

[14] W. van Keulen and M. Duškov. Inventory study on basic knowledge on tyre/road noise. Technical Report DWW-2005-022, Road and Hydraulic Engineering. Division of Rijkswaterstaat, Delft, Netherlands, 2005.

[15] W. A. Leasure and E. K. Bender. Tire–road interaction noise. *The Journal of the Acoustical Society of America*, 58(1):39–50, 1975.

[16] P. Riehm, H.-J. Unrau, F. Gauterin, S. Torbrügge, and B. Wies. 3D brush model to predict longitudinal tyre characteristics. *Vehicle System Dynamics*, 57(1):17–43, 2019.

[17] U. Sandberg. A closer look at the tread groove resonance in tyre/road noise. In *ICA 2004 – International Congress on Acoustics*, Kyoto, Japan, 2004.

[18] J. A. Ejsmont. Comparison of road and laboratory measurements and influence of some tire parameters on generation of sound. Technical Report 224A, Swedish Road and Transport Research Institute, Linköping, Sweden, 1982.

[19] R. Cao and J. S. Bolton. Loading effect on tire noise radiation. In *Inter-Noise 2016 – International Congress and Exhibition on Noise Control Engineering*, Hamburg, Germany, 2016.

[20] K. Iwao and I. Yamazaki. A study on the mechanism of tire/road noise. *JSAE Review*, 17(2):139–144, 1996.

[21] D. C. Stevenson. Some effects of tyre tread and road surface on road noise. *Journal of Sound and Vibration*, 48(4):561–564, 1976.

[22] P. Mioduszewski, S. Taryma, and R. Wozniak. Temperature influence on tyre/road noise frequency spectra. In *Inter-Noise 2016 – International*

Congress and Exhibition on Noise Control Engineering, Hamburg, Germany, 2016.

[23] P. Mioduszewski, S. Taryma, and R. Wozniak. Temperature influence on tire road noise of selected tires. In *Inter-Noise 2014 – International Congress and Exhibition on Noise Control Engineering*, Melbourne, Australia, 2014.

[24] F. Anfosso-Lédée and Y. Pichaud. Temperature effect on tyre–road noise. *Applied Acoustics*, 68(1):1–16, 2007.

[25] M. Bueno, J. Luong, U. Viñuela, F. Terán, and S. E. Paje. Pavement temperature influence on close proximity tire/road noise. *Applied Acoustics*, 72(11):829–835, 2011.

[26] G. Liao, M. Heitzman, R. West, S. Wang, and C. Ai. Temperature effects on the correlations between tire-pavement noises and pavement surface characteristics. In *International Symposium on Frontiers of Road and Airport Engineering*, Shanghai, China, 2015.

[27] F. G. Praticò and R. Vaiana. A study on the relationship between mean texture depth and mean profile depth of asphalt pavements. *Construction and Building Materials*, 101(1):72–79, 2015.

[28] P. M. Nelson. Rubber tyre noise generation. *Wear*, 113(1):171–174, 1986.

[29] A. Köllmann. Ermittlung des Standes der Technik der Geräuschemission von Pkw-Reifen. Technical Report 105 05 144, Forschungsinstitut Geräusch und Erschütterungen, Berlin, 1993.

[30] A. Kumar, A. Tandon, S. Paul, A. Singla, S. Kumar, P. Vijay, and U. D. Bhangale. Influence of tyre's dimensional characteristics on tyre-pavement noise emission. *Physical Review and Research International*, 1(4):124–137, 2011.

[31] T. Watanabe, N. Tomita, S. Kishinami, H. Yamaguchi, S. Konishi, and A. Kawana. The noise generation mechanism of cross-bar tyres and countermeasures against it. *International Journal of Vehicle Design*, 9(6):641–653, 1988.

[32] Q. van Doan. Influence of tire construction and tire mold profile on coast by noise. *Tire Technology International 1996, The Annual Review of Tire Materials and Tire Manufacturing Technology*, pages 28–35, 1996.

[33] W. Kropp, K. Larsson, and S. Barrelet. The influence of belt and tread band stiffness on the tire noise generation mechanisms. *The Journal of the Acoustical Society of America*, 103(5):2919, 1998.

[34] H. Zhou, G. Wang, Y. Zhang, J. Yang, and Z. Zheng. Study of the influence of tire belt structure on vibration noise. *Recent Patents on Mechanical Engineering*, 10(4), 2018.

[35] P. R. Willett. Tire tread pattern sound generation. *Tire Science and Technology*, 3(4):252–266, 1975.

[36] K. Hoffmeister and J. Bernard. Tread pitch arrangement optimization through the use of a genetic algorithm. *Tire Science and Technology*, 26(1):2–22, 1998.

[37] F. Stalter, M. Frey, and F. Gauterin. Einfluss des Antriebsmoments auf das Reifengeräusch. *ATZ – Automobiltechnische Zeitschrift*, 115(6):528–533, 2013.

[38] J. A. Ejsmont, U. Sandberg, and S. Taryma. Influence of tread pattern on tire/road noise. *SAE Transactions*, 93:632–640, 1984.

[39] K. Liljegren. Visual and acoustic tyre tread design. Master thesis, Chalmers University of Technology, Gothenburg, Sweden, 2008.

[40] S. Fujiwara, K. Yumii, T. Saguchi, and K. Kato. Reduction of tire groove noise using slot resonators. *Tire Science and Technology*, 37(3):207–223, 2009.

[41] Y. Nakajima. Theory on pitch noise and its application. *Journal of Vibration and Acoustics*, 125(3):252, 2003.

[42] U. Sandberg and J. A. Ejsmont. The influence of tire age and wear on tire/road noise emission. In *Inter-Noise 2002 – International Congress and Exhibition on Noise Control Engineering*, Dearborn, Michigan, USA, 2002.

[43] U. Sandberg and J. A. Ejsmont. Influence of tyre rubber hardness on tyre/road noise emission. In *Inter-Noise 2007 – International Congress and Exhibition on Noise Control Engineering*, Istanbul, Turkey, 2007.

[44] E.-U. Saemann. Contribution of the tyre to further lowering tyre/road noise. In *Acoustics'08*, Paris, France, 2008.

[45] U. Sandberg and J. A. Ejsmont. Noise emission, friction and rolling resistance of car tires – summary of an experimental study. In *Noise-Con*

2000 – National Conference on Noise Control Engineering, Newport Beach, California, USA, 2000.

[46] W. Gardziejczyk and P. Gierasimiuk. Influence of texturing method on tyre/road noise of cement concrete pavement. *International Journal of Pavement Engineering*, 9(3):1–16, 2017.

[47] U. Sandberg. Low noise road surfaces. A state-of-the-art review. *Journal of the Acoustical Society of Japan*, 20(1):1–17, 1999.

[48] M. A. Staiano. Tire–pavement noise and pavement texture. *Journal of Transportation Engineering, Part B: Pavements*, 144(3):1–10, 2018.

[49] DIN ISO 13473-1. Characterization of pavement texture by use of surface profiles – Part 1: Determination of mean profile depth, August 2017.

[50] K. K. McGhee and G. W. Flintsch. High-speed texture measurement of pavements. Technical report, Virginia Center for Transportation Innovation and Research, 2003.

[51] S. Å. Storeheier. Investigation on road surface texture levels in tyre/road noise mitigation. In *Inter-Noise 2004 – International Congress and Exhibition on Noise Control Engineering*, Prague, Czech Republic, 2004.

[52] L. Zhang, G. P. Ong, and T. F. Fwa. Analyzing the influence of pavement texture on tire-pavement noise generation. In *94th Transportation Research Board Annual Meeting*, Washington, D.C., USA, 2014.

[53] N. Pouliot, A. Carter, and P. Langlois. Close-proximity measurement of tire-pavement noise on the ministry of transportation of quebec's road network. In *Annual Conference of the Transportation Association of Canada*, Charlottetown, Canada, 2006.

[54] M. Sakhaeifar, A. Banihashemrad, G. Liao, and B. Waller. Tyre-pavement interaction noise levels related to pavement surface characteristics. *Road Materials and Pavement Design*, 19(5):1044–1056, 2017.

[55] Schweizerischer Verband der Strassen- und Verkehrsfachleute. Correlation between road texture and skid resistance of pavement and influences on noise. Technical Report VSS 2009/703, 2014.

[56] T. Beckenbauer. *Einfluss der Fahrbahntextur auf das Reifen-Fahrbahn-Geräusch*, volume 847 of *Forschung Straßenbau und Straßenverkehrstechnik*. Bundesministerium für Verkehr, Bau- und Wohnungswesen, Abteilung Straßenbau, Straßenverkehr, Bonn, 2002.

[57] T. Beckenbauer. Physik der Reifen-Fahrbahn-Geräusche: Geräuschentstehung, Wirkungsmechanismen und akustische Wirkung unter dem Einfluss von Bautechnik und straßenbetrieb. In *Informationstage Geräuschmindernde Fahrbahnbeläge in der Praxis–Lärmaktionsplanung*, Gelsenkirchen, Germany, 2008.

[58] M. Männel and T. Beckenbauer. Characterisation of road surfaces by means of texture analysis. *VDI-Berichte*, 2014:223–239, 2007.

[59] G. Kneib, D. Belcher, T. Beckenbauer, and H.-P. Beyeler. Continuous road traffic noise monitoring and aging of asphalt surfaces. In *Inter-Noise 2016 – International Congress and Exhibition on Noise Control Engineering*, Hamburg, Germany, 2016.

[60] F. Anfosso-Lédée and M.-T. Do. Geometric Descriptors of Road Surface Texture in Relation to Tire-Road Noise. *Transportation Research Record: Journal of the Transportation Research Board*, 1806(1):160–167, 2002.

[61] T. Fujikawa, H. Koike, Y. Oshino, and H. Tachibana. Definition of road roughness parameters for tire vibration noise control. *Applied Acoustics*, 66(5):501–512, 2005.

[62] T. Fujikawa, Y. Oshino, T. Mikami, and H. Tachibana. Examination of road roughness parameters for abating tire vibration and radiated noise. *Noise Control Engineering Journal*, 57(2):77–83, 2009.

[63] B. Peeters and A. Kuijpers. The effect of porous road surfaces on radiation and propagation of tyre noise. *Journal of the Acoustical Society of America*, 123(5):3673, 2008.

[64] B. Peeters, I. Ammerlaan, and A. Kuijpers. Noise reduction by absorbing road surfaces—destroying the horn effect. In *ISMA 2010 – International Conference on Noise and Vibration Engineering*, Leuven, Belgium, 2010.

[65] M. Oeser, A. Meyer, A. Ueckermann, and A. Schacht. Design von Straßenoberflächen: Zielkonflikte zwischen akustischen Eigenschaften, Griffigkeit, Rollwiderstand, Dauerhaftigkeit und Fahrkomfort. *VDI-Berichte*, 2241:193–223, 2015.

[66] M. Bezemer-Krijnenn, Y. Wijnant, and A. de Boer. Tyre-road noise measurements: influence of tyre tread and road characteristics. In *Inter-Noise 2016 – International Congress and Exhibition on Noise Control Engineering*, Hamburg, Germany, 2016.

[67] A. Ongel, E. Kohler, and J. Nelson. Acoustical absorption of open-graded, gap-graded, and dense-graded asphalt pavements. Technical Report UCPRC-RR-2007-13, University of California Pavement Research Center, 2007.

[68] T. Beckenbauer. Reifen-Fahrbahn-Geräusche – Minderungspotenziale der Straßenoberfläche. In *DAGA 2003, Fortschritte der Akustik, 29. Jahrestagung für Akustik, Plenarvorträge und Fachbeiträge*, Aachen, Germany, 2003.

[69] S. Alber. *Veränderung des Schallabsorptionsverhaltens von offenporigen Asphalten durch Verschmutzung*, volume 46 of *Veröffentlichungen aus dem Institut für Straßen- und Verkehrswesen*. Univ. Inst. für Straßen- und Verkehrswesen, Stuttgart, 2013.

[70] P. M. Morse and K. U. Ingard. *Theoretical acoustics*. Princeton University Press, Princeton, 1986.

[71] L. E. Kinsler. *Fundamentals of acoustics*. Wiley, New York, 4th edition, 2000.

[72] T. D. Rossing. *Springer Handbook of Acoustics*. Springer New York, New York, NY, 2014.

[73] S. K. Clark. *Mechanics of pneumatic tires*. US Government Printing Office, 1981.

[74] A. N. Gent and J. D. Walter. *The Pneumatic Tire*. Mechanical Engineering Faculty Research, The University of Akron, 2006.

[75] G. Leister. *Passenger Car Tires and Wheels*. Springer International Publishing, Cham, 2018.

[76] P. Kindt. *Structure-Borne Tyre/Road Noise Due to Road Surface Discontinuities*. PhD thesis, Department of Mechanical Engineering, Katholieke Universiteit Leuven, 2009.

[77] S. Ullrich, K.-P. Glaeser, and K. Sander. *Der Einfluß der Textur auf Reifen/Fahrbahngeräusch und Rollwiderstand: Untersuchungen im Prüfstand Fahrzeug/Fahrbahn*, volume 11 of *Berichte der Bundesanstalt für Straßenwesen S, Straßenbau*. Wirtschaftsverl. NW Verl. für neue Wiss, Bremerhaven, 1996.

[78] R. E. Hayden. Roadside noise from the interaction of a rolling tire with the road surface. *The Journal of the Acoustical Society of America*, 50(1A):113, 1971.

[79] Bundesanstalt für Straßenwesen. *Verbundprojekt "Leiser Straßenverkehr 2": Reduzierte Reifen-Fahrbahn-Geräusche*, volume 74 of *Berichte der Bundesanstalt für Strassenwesen S, Strassenbau*. Techn. Informationsbibl. und Univ.-Bibl and Wirtschaftsverl. NW Verl. für neue Wiss, Hannover and Bremerhaven, 2012.

[80] Bundesanstalt für Straßenwesen. Verbundprojekt "leiser Straßenverkehr 3": Gemeinsamer Schlussbericht. https://bast.opus.hbz-nrw.de/opus45-bast/frontdoor/deliver/index/docId/2056/file/LeiStra3_Gemeinsamer_Schlussbericht.pdf. Accessed: 09.12.2019.

[81] O. Krauss. *Experimentelle Untersuchungen zum Innengeräusch von Fahrzeugluftreifen*, volume 68 of *Karlsruher Schriftenreihe Fahrzeugsystemtechnik*. KIT Scientific Publishing, Karlsruhe, Baden, 2019.

[82] Z. Mohamed, X. Wang, and R. Jazar. A survey of wheel tyre cavity resonance noise. *International Journal of Vehicle Noise and Vibration*, 9(3/4):276–293, 2013.

[83] DIN ISO 13473-5. Characterization of pavement texture by use of surface profiles – Part 5: Determination of megatexture, 2009.

[84] DIN ISO 13473-2. Characterization of pavement texture by use of surface profiles – Part 2: Terminology and basic requirements related to pavement texture profile analysis, 2002.

[85] A. Schacht. *Entwicklung künstlicher Straßendeckschichtsysteme auf Kunststoffbasis zur Geräuschreduzierung mit numerischen und empirischen Verfahren*, volume 63 of *Aachener Mitteilungen Straßenwesen, Erd- und Tunnelbau*. Aachen : Materialprüfstelle für Straßenbau, RWTH Aachen University, 2015.

[86] I. Müller. *Untersuchung der Messunsicherheit und der Klassifizierungsfähigkeit von Straßenbelägen: Erfassung von Straßenoberflächentexturen und Untersuchung der Klassifizierungsfähigkeit von Straßenbelägen mittels (akustisch) relevanter Texturkenngrößen*, volume 69 of *Berichte der Bundesanstalt für Straßenwesen S, Straßenbau*. Wirtschaftsverl. NW, Verl. für neue Wiss, Bremerhaven, 2011.

[87] E. J. Abbott and F. A. Firestone. Specifying surface quality: a method based on accurate measurement and comparison. *Mechanical Engineering*, 55:569–572, 1933.

[88] DIN ISO 10844. Acoustics – Specification of test tracks for measuring noise emitted by road vehicles and their tyres, 2014.

[89] R. Sohaney, R. Rasmussen, A. Seybert, and P. Donovan. New iso test track specification for measuring tire and vehicle noise. *Sound And Vibration*, 46(8):9–14, 2012.

[90] D. Moore. Revised iso 10844 test surface: Technical principles. *SAE International Journal of Passenger Cars – Mechanical Systems*, 4(2):1126–1131, 2011.

[91] DIN ISO 10844. Acoustics – Specification of test tracks for measuring noise emitted by road vehicles and their tyres, 2014.

[92] P. Klein and J.-F. Hamet. ENDT, Expected pass-by noise level difference from texture level variation of the road surface. Technical report, SILVIA Project Report, 2005.

[93] J. O. Ramsay and B. W. Silverman. *Functional Data Analysis*. Springer Series in Statistics. Springer Science+Business Media Inc, New York, NY, 2nd edition, 2005.

[94] D. C. Montgomery, E. A. Peck, and G. G. Vining. *Introduction to linear regression analysis*, volume 821 of *Wiley series in probability and statistics*. Wiley, Hoboken, NJ, 5th edition, 2012.

[95] J. F. Hair, B. J. Babin, R. E. Anderson, and W. C. Black. *Multivariate data analysis*. Pearson custom library. Pearson, Harlow, Essex, 7th edition, 2014.

[96] N. Meinshausen. Relaxed lasso. *Computational Statistics & Data Analysis*, 52(1):374–393, 2007.

[97] H. Zou. The adaptive lasso and its oracle properties. *Journal of the American Statistical Association*, 101(476):1418–1429, 2006.

[98] T. Hesterberg, N. H. Choi, L. Meier, and C. Fraley. Least angle and l1 penalized regression: A review. *Statistics Surveys*, 2(0):61–93, 2008.

[99] P. H. C. Eilers and B. D. Marx. Flexible smoothing with b-splines and penalties. *Statistical Science*, 11(2):89–102, 1996.

[100] SAS Institute. *JMP® version 14: Fitting linear models*. Cary, NC, 2018.

[101] T. Hastie, R. Tibshirani, and J. Friedman. *The Elements of Statistical Learning*. Springer New York, New York, NY, 2009.

135

[102] H. Akaike. A new look at the statistical model identification. *IEEE Transactions on Automatic Control*, 19(6):716–723, 1974.

[103] C. B. García, J. García, M. M. López Martín, and R. Salmerón. Collinearity: revisiting the variance inflation factor in ridge regression. *Journal of Applied Statistics*, 42(3):648–661, 2015.

[104] J. Hauke and T. Kossowski. Comparison of values of pearson's and spearman's correlation coefficients on the same sets of data. *Quaestiones Geographicae*, 30(2):87–93, 2011.

[105] R. Gnadler, H.-J Unrau, Michael Frey, and M. Fertig. *Grundsatzuntersuchung zum quantitativen Einfluß von Reifenbauform und -ausführung auf die Fahrstabilität von Kraftfahrzeugen bei extremen Fahrmanövern*, volume 192 of *FAT-Schriftenreihe*. Forschungsvereinigung Automobiltechnik e.V., Frankfurt, M., 2005.

[106] M. Gießler. *Mechanismen der Kraftübertragung des Reifens auf Schnee und Eis*, volume 11 of *Karlsruher Schriftenreihe Fahrzeugsystemtechnik*. KIT Scientific Publishing, Karlsruhe, Baden, 2012.

[107] B. Wassertheurer. *Reifenmodellierung für die Fahrdynamiksimulation auf Schnee, Eis und nasser Fahrbahn*, volume 75 of *Karlsruher Schriftenreihe Fahrzeugsystemtechnik*. KIT Scientific Publishing, Karlsruhe, Baden, 2019.

[108] P. Riehm, M. Greiner, K.-L. Bückle, H.-J. Unrau, and F. Gauterin. A measuring system for continuous friction monitoring on wet track surfaces. *Tire Science and Technology*, 46(4):259–275, 2018.

[109] F. Stalter. *Ansätze zur akustischen Optimierung von Reifen und Fahrbahnen für Elektrofahrzeuge unter Antriebsmoment*, volume 55 of *Karlsruher Schriftenreihe Fahrzeugsystemtechnik*. KIT Scientific Publishing, Karlsruhe, Baden, 2017.

[110] J. Pinay, F. Gauterin, and H.-J Unrau. Experimental sudy of the tire cavity noise and its correlation with the exterior tire-road noise emission. In *16. Internationale VDI-Tagung, Reifen-Fahrwerk-Fahrbahn 2017*, Hanover, Germany, 2017.

[111] Institut für Fahrzeugsystemtechnik, Teilinstitut Fahrzeugtechnik, Reifen-Innentrommel-Prüfstand. https://www.fast.kit.edu/lff/1251.php. Accessed: 18.08.2019.

[112] J. Pinay, Y. Saito, C. Mignot, and F. Gauterin. Understanding the contribution of groove resonance to tire-road noise on different surfaces under various operating conditions. *Acta Acustica*, 4(2):6, 2020.

[113] DIN ISO 11819-2. Acoustics – Measurement of the influence of road surfaces on traffic noise – Part 2: The close-proximity method, 2017.

[114] DIN ISO 13473-3. Characterization of pavement texture by use of surface profiles – Part 3: Specifications and classification of profilometers, 2004.

[115] DIN ISO 13472-2. Acoustics – Measurement of sound absorption properties of road surfaces in situ – Part 2: Spot method for reflective surfaces (iso 13472-2:2010).

[116] DIN EN ISO 10534-2. Acoustics – Determination of sound absorption coefficient and impedance in impedance tubes – Part 2: Transfer-function method, 1998.

[117] C. G. Giles, B. E. Sabey, and K. H. F. Cardew. Development and performance of the portable skid resistance tester. *Rubber Chemistry and Technology*, 38(4):840–862, 1965.

[118] DIN EN 13036-4. Road and airfield surface characteristics – test methods – Part 4: Method for measurement of slip/skid resistance of a surface – the pendulum test, 2011.

[119] X. Cao. Development of an evaluation tool for tire footprints analysis using image processing. Master thesis, Karlsruher Institut für Technologie (KIT), Karlsruhe, 2017.

[120] V. Hittinger. Modelisation of the pipe resonances using tire-footprints. Master-thesis, Karlsruher Institut für Technologie (KIT), Karlsruhe, 2017.

[121] S. Mun. Sound absorption characteristics of porous asphalt concrete pavements. *Canadian Journal of Civil Engineering*, 37(2):273–278, 2010.

[122] E.-U. Saemann and H. Schmidt. Schallmessungen bei der Entwicklung von Reifen mit geringem Vorbeifahrtpegel. *Zeitschrift für Lärmbekämpfung*, 49(2):59–62, 2002.

[123] W. Kropp, F.-X. Bécot, and S. Barrelet. On the sound radiation from tyres. *Acta Acustica united with acustica*, 86(5):769–779, 2000.

[124] M. Bürckert. *Realitätsnahe Bewertung des Einflusses der Oberflächenspannung flüssiger Zwischenmedien auf den maximalen Reibschluss zwischen Reifen und Fahrbahn*, volume 70 of *Karlsruher Schriftenreihe Fahrzeugsystemtechnik*. KIT Scientific Publishing, Karlsruhe, Baden, 2019.

A   Appendix

A.1   Characteristics of the measured road surfaces

A.1.1 Inner drum test bench

Table A.1: Characteristics of Asphalt 0/5

Description	Scalar descriptors			
Inner Drum	MPD [mm]	0.37	SRT [-]	58
Asphalt 0/5	Absorption [%]	2.7	Ltx FPC1 [-]	-2.44
	RMS [mm]	0.21	Ltx FPC2 [-]	-18.46
	RSK [-]	-0.92	Ltx FPC3 [-]	n.a.
	RKU [-]	6.21	Abbott FPC1 [-]	-0.30
	g [%]	81.93	Abbott FPC2 [-]	-0.03

Table A.2: Characteristics of Asphalt 0/11

Description	Scalar descriptors			
Inner Drum	MPD [mm]	1.15	SRT [-]	51
Asphalt 0/11	Absorption [%]	2.30	Ltx FPC1 [-]	-10.16
	RMS [mm]	0.52	Ltx FPC2 [-]	0.42
	RSK [-]	0.26	Ltx FPC3 [-]	n.a.
	RKU [-]	4.21	Abbott FPC1 [-]	-0.03
	g [%]	55.13	Abbott FPC2 [-]	0.11

Table A.3: Characteristics of SMA 0/8

Description	Scalar descriptors			
Inner Drum	MPD [mm]	1.19	SRT [-]	56
SMA 0/8	Absorption [%]	12.20	Ltx FPC1 [-]	-29.37
	RMS [mm]	0.95	Ltx FPC2 [-]	11.96
	RSK [-]	-1.37	Ltx FPC3 [-]	-3.73
	RKU [-]	5.29	Abbott FPC1 [-]	0.43
	g [%]	86.87	Abbott FPC2 [-]	-0.13

Table A.4: Characteristics of Safety-Walk
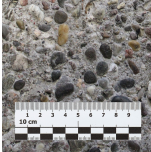
Description	Scalar descriptors			
Inner Drum	MPD [mm]	0.15	SRT [-]	70
Safety-Walk	Absorption [%]	0.10	Ltx FPC1 [-]	67.85
	RMS [mm]	0.08	Ltx FPC2 [-]	-1.55
	RSK [-]	-0.14	Ltx FPC3 [-]	n.a.
	RKU [-]	3.37	Abbott FPC1 [-]	-0.43
	g [%]	58.57	Abbott FPC2 [-]	-0.03

Table A.5: Characteristics of Concrete 0/16

Description	Scalar descriptors			
Inner Drum	MPD [mm]	1.44	SRT [-]	56
Concrete 0/16	Absorption [%]	1.00	Ltx FPC1 [-]	-25.87
	RMS [mm]	0.86	Ltx FPC2 [-]	7.67
	RSK [-]	-0.33	Ltx FPC3 [-]	n.a.
	RKU [-]	3.08	Abbott FPC1 [-]	0.32
	g [%]	64.30	Abbott FPC2 [-]	0.09

A.1.2 Field measurements

Table A.6: Road surfaces used for coast-by measurements

#	Location	Longitude, latitude	Pavement type	Symbol
1	Confidential	Confidential	ISO 10844:2011	+
2	Confidential	Confidential	ISO 10844:2011	+
3	Confidential	Confidential	ISO 10844:2011	○
4	Confidential	Confidential	ISO 10844:2011	○
5	Confidential	Confidential	ISO 10844:2011	✳
6	Confidential	Confidential	ISO 10844:2011	✳
7	Confidential	Confidential	ISO 10844:2011	•
8	Confidential	Confidential	ISO 10844:2011	•
9	Confidential	Confidential	ISO 10844:2011	×
10	Confidential	Confidential	ISO 10844:2011	×
11	Confidential	Confidential	ISO 10844:1998	□
12	Confidential	Confidential	ISO 10844:1998	□
13	Confidential	Confidential	ISO 10844:2011	◇
14	Confidential	Confidential	Unknown	
15	Geilenkirchen	50.96281, 6.05303	SMA 0/5	
16	Geilenkirchen	50.96281, 6.05303	SMA 0/5	
17	Geilenkirchen	50.96281, 6.05303	SMA 0/5	
18	Geilenkirchen	50.96277, 6.05171	SMA 0/5	
19	Geilenkirchen	50.96277, 6.05171	SMA 0/5	
20	Geilenkirchen	50.96277, 6.05171	SMA 0/5	
21	Geilenkirchen	50.96301, 6.03041	Mastic Asphalt	
22	Geilenkirchen	50.96301, 6.03041	SMA 0/8	
23	Geilenkirchen	50.96289, 6.0466	NOA 0/5	
24	Geilenkirchen	50.96287, 6.04825	NOA 0/5	
25	Geilenkirchen	50.96293, 6.04812	NOA 0/5	
26	Geilenkirchen	50.96295, 6.0466	PMA 0/5	
27	Geilenkirchen	50.96291, 6.04748	PMA 0/5	
28	Via Vecchia Pietrasantina	43.747550, 10.361915	Unknown	
29	Via die Torreta	43.671169, 10.314263	Unknown	
30	Via Ulisse Dini Gello	43.740270, 10.414024	Unknown	
31	Via Titignano	43.670352, 10.443394	Unknown	
32	Junction Strade Statali 12	43.756556, 10.437167	Unknown	

ISO 10844 test tracks

Table A.7: Characteristics of road surface #1 (see Table A.6)

Description		Scalar descriptors		
Confidential	MPD [mm]	0.53	SRT [-]	52
ISO 10844:2011	Absorption [%]	1.73	Ltx FPC1 [-]	-8.50
	RMS [mm]	0.40	Ltx FPC2 [-]	5.33
	RSK [-]	-1.26	Ltx FPC3 [-]	-3.13
	RKU [-]	4.66	Abbott FPC1 [-]	-0.12
	g [%]	81.99	Abbott FPC2 [-]	0.03

Table A.8: Characteristics of road surface #2 (see Table A.6)

Description		Scalar descriptors		
Confidential	MPD [mm]	0.53	SRT [-]	56
ISO 10844:2011	Absorption [%]	3.97	Ltx FPC1 [-]	-8.25
	RMS [mm]	0.41	Ltx FPC2 [-]	5.09
	RSK [-]	-1.06	Ltx FPC3 [-]	-6.30
	RKU [-]	3.54	Abbott FPC1 [-]	-0.10
	g [%]	77.63	Abbott FPC2 [-]	0.03

Table A.9: Characteristics of road surface #3 (see Table A.6)

Description		Scalar descriptors		
Confidential	MPD [mm]	0.75	SRT [-]	41
ISO 10844:2011	Absorption [%]	1.47	Ltx FPC1 [-]	3.09
	RMS [mm]	0.44	Ltx FPC2 [-]	2.76
	RSK [-]	-0.79	Ltx FPC3 [-]	1.97
	RKU [-]	3.78	Abbott FPC1 [-]	-0.06
	g [%]	78.53	Abbott FPC2 [-]	-0.01

Table A.10: Characteristics of road surface #4 (see Table A.6)

Description				
	Scalar descriptors			
Confidential	MPD [mm]	0.70	SRT [-]	17
ISO 10844:2011	Absorption [%]	0.50	Ltx FPC1 [-]	-3.99
	RMS [mm]	0.38	Ltx FPC2 [-]	-0.91
	RSK [-]	-0.25	Ltx FPC3 [-]	2.83
	RKU [-]	2.79	Abbott FPC1 [-]	-0.11
	g [%]	63.57	Abbott FPC2 [-]	-0.07

Table A.11: Characteristics of road surface #5 (see Table A.6)

Description				
	Scalar descriptors			
Confidential	MPD [mm]	0.40	SRT [-]	46
ISO 10844:2011	Absorption [%]	0.57	Ltx FPC1 [-]	-11.99
	RMS [mm]	0.26	Ltx FPC2 [-]	-9.84
	RSK [-]	-0.88	Ltx FPC3 [-]	2.99
	RKU [-]	3.35	Abbott FPC1 [-]	-0.24
	g [%]	72.55	Abbott FPC2 [-]	-0.04

Table A.12: Characteristics of road surface #6 (see Table A.6)

Description				
	Scalar descriptors			
Confidential	MPD [mm]	0.57	SRT [-]	49
ISO 10844:2011	Absorption [%]	0.20	Ltx FPC1 [-]	-4.80
	RMS [mm]	0.38	Ltx FPC2 [-]	-0.25
	RSK [-]	-0.92	Ltx FPC3 [-]	-6.07
	RKU [-]	3.50	Abbott FPC1 [-]	-0.12
	g [%]	72.72	Abbott FPC2 [-]	0.00

Table A.13: Characteristics of road surface #7 (see Table A.6)

Description	Scalar descriptors			
Confidential	MPD [mm]	0.43	SRT [-]	60
ISO 10844:2011	Absorption [%]	0.60	Ltx FPC1 [-]	-11.04
	RMS [mm]	0.29	Ltx FPC2 [-]	-1.03
	RSK [-]	-1.12	Ltx FPC3 [-]	-0.78
	RKU [-]	4.12	Abbott FPC1 [-]	-0.21
	g [%]	78.11	Abbott FPC2 [-]	-0.01

Table A.14: Characteristics of road surface #8 (see Table A.6)

Description	Scalar descriptors			
Confidential	MPD [mm]	0.30	SRT [-]	56
ISO 10844:2011	Absorption [%]	1.47	Ltx FPC1 [-]	-21.87
	RMS [mm]	0.23	Ltx FPC2 [-]	2.61
	RSK [-]	-1.71	Ltx FPC3 [-]	1.91
	RKU [-]	6.95	Abbott FPC1 [-]	-0.28
	g [%]	91.31	Abbott FPC2 [-]	-0.02

Table A.15: Characteristics of road surface #9 (see Table A.6)

Description	Scalar descriptors			
Confidential	MPD [mm]	0.37	SRT [-]	43
ISO 10844:2011	Absorption [%]	5.07	Ltx FPC1 [-]	-15.45
	RMS [mm]	0.29	Ltx FPC2 [-]	-1.17
	RSK [-]	-0.96	Ltx FPC3 [-]	-0.81
	RKU [-]	3.01	Abbott FPC1 [-]	-0.21
	g [%]	74.24	Abbott FPC2 [-]	-0.01

Table A.16: Characteristics of road surface #10 (see Table A.6)

Description	Scalar descriptors			
Confidential	MPD [mm]	0.35	SRT [-]	51
ISO 10844:2011	Absorption [%]	3.57	Ltx FPC1 [-]	-13.67
	RMS [mm]	0.32	Ltx FPC2 [-]	-1.87
	RSK [-]	-1.78	Ltx FPC3 [-]	-1.35
	RKU [-]	7.18	Abbott FPC1 [-]	-0.21
	g [%]	89.88	Abbott FPC2 [-]	0.02

Table A.17: Characteristics of road surface #11 (see Table A.6)

Description	Scalar descriptors			
Confidential	MPD [mm]	0.68	SRT [-]	45
ISO 10844:2011	Absorption [%]	0.23	Ltx FPC1 [-]	-3.50
	RMS [mm]	0.38	Ltx FPC2 [-]	10.93
	RSK [-]	-0.91	Ltx FPC3 [-]	6.67
	RKU [-]	4.66	Abbott FPC1 [-]	-0.13
	g [%]	82.75	Abbott FPC2 [-]	-0.02

Table A.18: Characteristics of road surface #12 (see Table A.6)

Description	Scalar descriptors			
Confidential	MPD [mm]	0.65	SRT [-]	50
ISO 10844:2011	Absorption [%]	0.47	Ltx FPC1 [-]	-13.56
	RMS [mm]	0.38	Ltx FPC2 [-]	7.11
	RSK [-]	-1.01	Ltx FPC3 [-]	-2.96
	RKU [-]	4.68	Abbott FPC1 [-]	-0.13
	g [%]	83.61	Abbott FPC2 [-]	-0.01

Public roads

Table A.19: Characteristics of road surface #13 (see Table A.6)

Description	Scalar descriptors			
Confidential	MPD [mm]	0.63	SRT [-]	37
ISO 10844:2011	Absorption [%]	1.97	Ltx FPC1 [-]	-5.01
	RMS [mm]	0.42	Ltx FPC2 [-]	0.06
	RSK [-]	-0.84	Ltx FPC3 [-]	-0.13
	RKU [-]	3.16	Abbott FPC1 [-]	-0.09
	g [%]	75.28	Abbott FPC2 [-]	0.01

Table A.20: Characteristics of road surface #14 (see Table A.6)

Description	Scalar descriptors			
Confidential	MPD [mm]	1.08	SRT [-]	50
Unknown	Absorption [%]	1.00	Ltx FPC1 [-]	15.38
	RMS [mm]	0.75	Ltx FPC2 [-]	-4.21
	RSK [-]	-0.94	Ltx FPC3 [-]	-5.15
	RKU [-]	3.50	Abbott FPC1 [-]	0.22
	g [%]	76.08	Abbott FPC2 [-]	0.11

Table A.21: Characteristics of road surface #15 (see Table A.6)

Description	Scalar descriptors			
Geilenkirchen	MPD [mm]	1.25	SRT [-]	48
SMA 0/5	Absorption [%]	7.60	Ltx FPC1 [-]	6.29
	RMS [mm]	0.67	Ltx FPC2 [-]	1.69
	RSK [-]	-0.18	Ltx FPC3 [-]	-2.25
	RKU [-]	2.46	Abbott FPC1 [-]	0.17
	g [%]	59.77	Abbott FPC2 [-]	-0.04
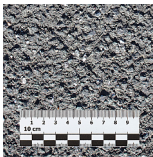
Table A.22: Characteristics of road surface #16 (see Table A.6)
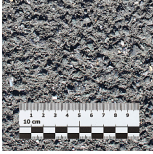
Description		Scalar descriptors		
Geilenkirchen	MPD [mm]	1.40	SRT [-]	57
SMA 0/5	Absorption [%]	7.10	Ltx FPC1 [-]	12.29
	RMS [mm]	0.73	Ltx FPC2 [-]	-2.99
	RSK [-]	0.01	Ltx FPC3 [-]	0.29
	RKU [-]	2.37	Abbott FPC1 [-]	0.22
	g [%]	54.17	Abbott FPC2 [-]	-0.07

Table A.23: Characteristics of road surface #17 (see Table A.6)
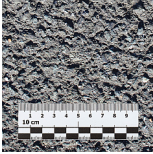
Description		Scalar descriptors		
Geilenkirchen	MPD [mm]	1.55	SRT [-]	53
SMA 0/5	Absorption [%]	5.77	Ltx FPC1 [-]	11.85
	RMS [mm]	0.78	Ltx FPC2 [-]	4.87
	RSK [-]	0.04	Ltx FPC3 [-]	1.96
	RKU [-]	2.51	Abbott FPC1 [-]	0.27
	g [%]	52.50	Abbott FPC2 [-]	-0.07

Table A.24: Characteristics of road surface #18 (see Table A.6)
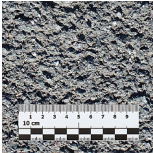
Description		Scalar descriptors		
Geilenkirchen	MPD [mm]	1.69	SRT [-]	56
SMA 0/5	Absorption [%]	5.87	Ltx FPC1 [-]	19.01
	RMS [mm]	0.86	Ltx FPC2 [-]	-3.41
	RSK [-]	0.03	Ltx FPC3 [-]	4.84
	RKU [-]	2.52	Abbott FPC1 [-]	0.35
	g [%]	51.12	Abbott FPC2 [-]	-0.07

Table A.25: Characteristics of road surface #19 (see Table A.6)
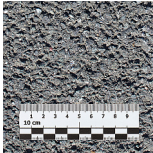
Description	Scalar descriptors			
Geilenkirchen	MPD [mm]	0.92	SRT [-]	51
SMA 0/5	Absorption [%]	3.40	Ltx FPC1 [-]	3.04
	RMS [mm]	0.56	Ltx FPC2 [-]	8.12
	RSK [-]	-0.43	Ltx FPC3 [-]	1.64
	RKU [-]	2.53	Abbott FPC1 [-]	0.06
	g [%]	65.78	Abbott FPC2 [-]	-0.01

Table A.26: Characteristics of road surface #20 (see Table A.6)
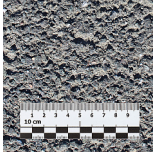
Description	Scalar descriptors			
Geilenkirchen	MPD [mm]	0.97	SRT [-]	62
SMA 0/5	Absorption [%]	2.37	Ltx FPC1 [-]	6.02
	RMS [mm]	0.59	Ltx FPC2 [-]	-2.13
	RSK [-]	-0.43	Ltx FPC3 [-]	-1.23
	RKU [-]	2.55	Abbott FPC1 [-]	0.09
	g [%]	64.93	Abbott FPC2 [-]	-0.01

Table A.27: Characteristics of road surface #21 (see Table A.6)
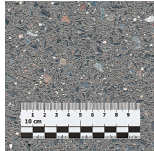
Description	Scalar descriptors			
Geilenkirchen	MPD [mm]	0.19	SRT [-]	42
Mastic Asphalt	Absorption [%]	0.13	Ltx FPC1 [-]	-19.74
	RMS [mm]	0.10	Ltx FPC2 [-]	-19.24
	RSK [-]	-0.46	Ltx FPC3 [-]	7.70
	RKU [-]	4.58	Abbott FPC1 [-]	-0.38
	g [%]	69.07	Abbott FPC2 [-]	-0.10

Table A.28: Characteristics of road surface #22 (see Table A.6)
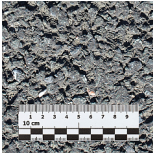
Description		Scalar descriptors		
Geilenkirchen	MPD [mm]	1.16	SRT [-]	51
SMA 0/8	Absorption [%]	2.63	Ltx FPC1 [-]	14.88
	RMS [mm]	0.86	Ltx FPC2 [-]	-5.42
	RSK [-]	-0.76	Ltx FPC3 [-]	-1.30
	RKU [-]	2.82	Abbott FPC1 [-]	0.33
	g [%]	72.17	Abbott FPC2 [-]	0.12

Table A.29: Characteristics of road surface #23 (see Table A.6)
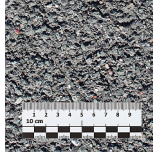
Description		Scalar descriptors		
Geilenkirchen	MPD [mm]	1.05	SRT [-]	55
NOA 0/5	Absorption [%]	3.07	Ltx FPC1 [-]	9.88
	RMS [mm]	0.65	Ltx FPC2 [-]	-2.94
	RSK [-]	-0.47	Ltx FPC3 [-]	-0.76
	RKU [-]	2.63	Abbott FPC1 [-]	0.14
	g [%]	67.47	Abbott FPC2 [-]	0.01

Table A.30: Characteristics of road surface #24 (see Table A.6)
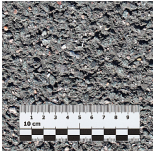
Description		Scalar descriptors		
Geilenkirchen	MPD [mm]	1.00	SRT [-]	55
NOA 0/5	Absorption [%]	1.40	Ltx FPC1 [-]	-0.35
	RMS [mm]	0.62	Ltx FPC2 [-]	13.31
	RSK [-]	-0.57	Ltx FPC3 [-]	0.88
	RKU [-]	2.83	Abbott FPC1 [-]	0.11
	g [%]	70.72	Abbott FPC2 [-]	0.02

Table A.31: Characteristics of road surface #25 (see Table A.6)
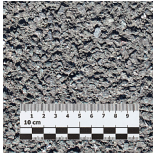
Description		Scalar descriptors		
Geilenkirchen	MPD [mm]	1.00	SRT [-]	51
NOA 0/5	Absorption [%]	5.50	Ltx FPC1 [-]	8.57
	RMS [mm]	0.63	Ltx FPC2 [-]	0.22
	RSK [-]	-0.50	Ltx FPC3 [-]	-1.07
	RKU [-]	2.64	Abbott FPC1 [-]	0.12
	g [%]	69.00	Abbott FPC2 [-]	0.01

Table A.32: Characteristics of road surface #26 (see Table A.6)
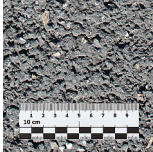
Description		Scalar descriptors		
Geilenkirchen	MPD [mm]	0.86	SRT [-]	50
PMA 0/5	Absorption [%]	1.20	Ltx FPC1 [-]	-1.00
	RMS [mm]	0.58	Ltx FPC2 [-]	0.31
	RSK [-]	-0.79	Ltx FPC3 [-]	2.83
	RKU [-]	3.12	Abbott FPC1 [-]	0.06
	g [%]	74.14	Abbott FPC2 [-]	0.04

Table A.33: Characteristics of road surface #27 (see Table A.6)
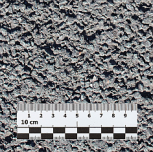
Description		Scalar descriptors		
Geilenkirchen	MPD [mm]	1.10	SRT [-]	53
PMA 0/5	Absorption [%]	1.70	Ltx FPC1 [-]	13.95
	RMS [mm]	0.75	Ltx FPC2 [-]	10.17
	RSK [-]	-0.67	Ltx FPC3 [-]	1.28
	RKU [-]	2.85	Abbott FPC1 [-]	0.23
	g [%]	71.81	Abbott FPC2 [-]	0.07

Table A.34: Characteristics of road surface #28 (see Table A.6)
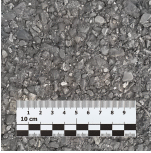
Description			Scalar descriptors	
Via Vecchia Pietrasantina	MPD [mm]	1.07	SRT [-]	34
Unknown	Absorption [%]	1.80	Ltx FPC1 [-]	16.12
	RMS [mm]	0.69	Ltx FPC2 [-]	-5.60
	RSK [-]	-0.80	Ltx FPC3 [-]	-0.67
	RKU [-]	3.33	Abbott FPC1 [-]	0.17
	g [%]	73.88	Abbott FPC2 [-]	0.06

Table A.35: Characteristics of road surface #29 (see Table A.6)
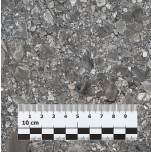
Description			Scalar descriptors	
Via die Torreta	MPD [mm]	1.10	SRT [-]	36
Unknown	Absorption [%]	1.63	Ltx FPC1 [-]	12.76
	RMS [mm]	0.66	Ltx FPC2 [-]	-2.45
	RSK [-]	-0.39	Ltx FPC3 [-]	6.98
	RKU [-]	2.80	Abbott FPC1 [-]	0.15
	g [%]	65.83	Abbott FPC2 [-]	-0.01

Table A.36: Characteristics of road surface #30 (see Table A.6)

Description			Scalar descriptors	
Via Ulisse Dini Gello	MPD [mm]	0.29	SRT [-]	37
Unknown	Absorption [%]	0.43	Ltx FPC1 [-]	-15.26
	RMS [mm]	0.23	Ltx FPC2 [-]	2.47
	RSK [-]	-1.37	Ltx FPC3 [-]	3.20
	RKU [-]	5.25	Abbott FPC1 [-]	-0.28
	g [%]	84.50	Abbott FPC2 [-]	-0.03

Table A.37: Characteristics of road surface #31 (see Table A.6)
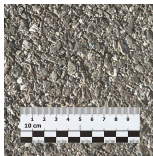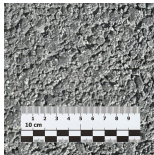
Description	Scalar descriptors			
Via Titignano	MPD [mm]	0.73	SRT [-]	56
Unknown	Absorption [%]	0.87	Ltx FPC1 [-]	0.54
	RMS [mm]	0.47	Ltx FPC2 [-]	-5.91
	RSK [-]	-0.82	Ltx FPC3 [-]	-10.34
	RKU [-]	3.22	Abbott FPC1 [-]	-0.04
	g [%]	72.98	Abbott FPC2 [-]	0.02

Table A.38: Characteristics of road surface #32 (see Table A.6)

Description	Scalar descriptors			
Junction Strade Statali	MPD [mm]	0.76	SRT [-]	52
Unknown	Absorption [%]	2.73	Ltx FPC1 [-]	4.31
	RMS [mm]	0.58	Ltx FPC2 [-]	-5.68
	RSK [-]	-0.87	Ltx FPC3 [-]	-3.67
	RKU [-]	2.94	Abbott FPC1 [-]	0.06
	g [%]	74.60	Abbott FPC2 [-]	0.07

A.2 Statistical analysis results

A.2.1 Functional principal component analysis on the inner drum test bench's surfaces

(a) Eigenfunction 1

(b) Eigenmode variation 1

(c) Eigenfunction 2

(d) Eigenmode Variation 2

FPC = 0 —— FPC > 0 —— FPC < 0
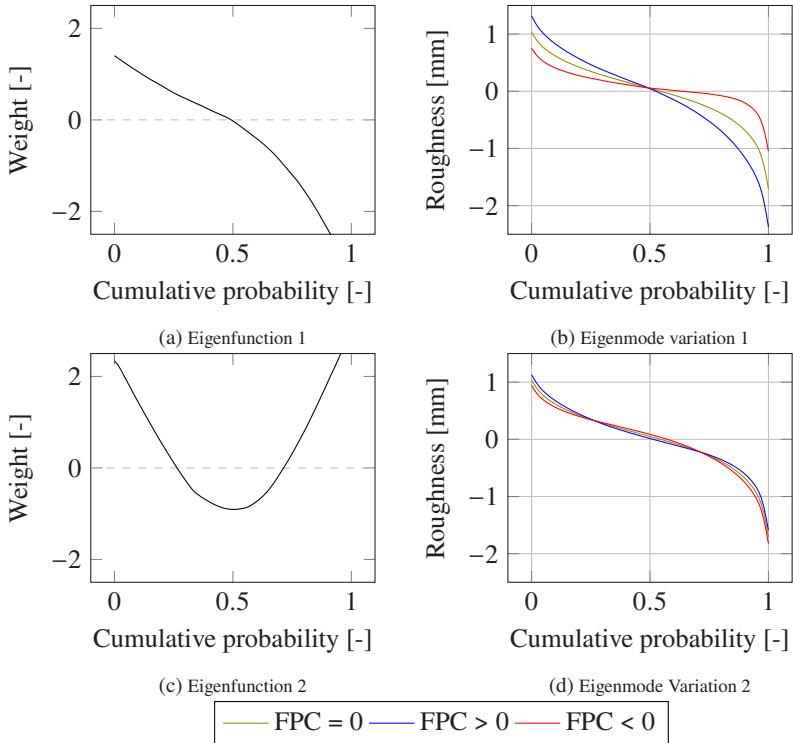
Figure A.1: Eigenfunctions of the principal components for the Abbott curve

(a) Eigenfunction 1

(b) Eigenmode Variation 1

(c) Eigenfunction 2

(d) Eigenmode Variation 2
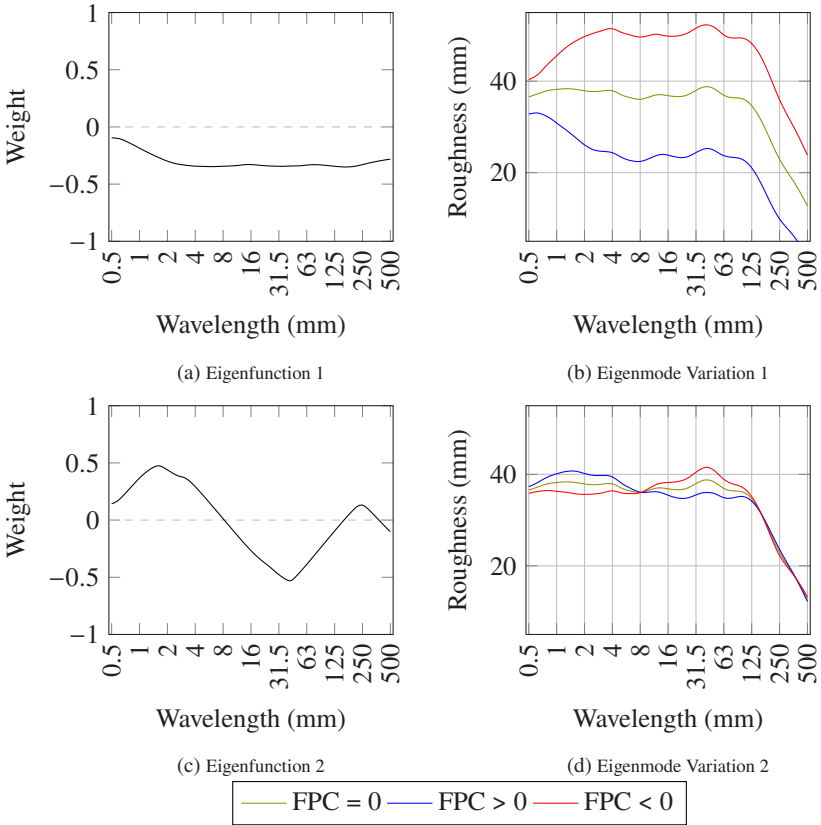
Figure A.2: Eigenfunctions of the principal components for the third-octave band spectra of the road surface roughness

A.2.2 Correlation analysis of the road surface descriptors

Table A.39: Correlation coefficients between road surfaces descriptors for the surfaces from the inner drum test bench

	Abbott FPC1	RMS	Ltx FPC1	MPD	RSK	Absorption	Abbott FPC2	Ltx FPC2	SRT	RKU	g
Abbott FPC1	1										
RMS	0.999	1									
Ltx FPC1	-0.829	-0.836	1								
MPD	0.913	0.929	-0.836	1							
RSK	-0.380	-0.346	0.382	-0.012	1						
Absorption	0.635	0.618	-0.528	0.352	-0.777	1					
Abbott FPC2	-0.060	-0.023	-0.103	0.342	0.841	-0.705	1				
Ltx FPC2	0.787	0.787	-0.334	0.710	-0.052	0.458	-0.057	1			
SRT	-0.633	-0.658	0.896	-0.787	0.040	-0.356	-0.362	-0.219	1		
RKU	-0.069	-0.081	-0.310	-0.231	-0.673	0.519	-0.527	-0.510	-0.269	1	
G	0.335	0.306	-0.446	0.006	-0.982	0.751	-0.774	-0.076	-0.148	0.788	1

Table A.40: Correlation coefficients between road surfaces descriptors for all real roads

	Abbott FPC1	RMS	Ltx FPC1	MPD	RSK	Absorption	Abbott FPC2	Ltx FPC2	SRT	Ltx FPC3	RKU	g
Abbott FPC1	1											
RMS	0.999	1										
Ltx FPC1	0.955	0.953	1									
MPD	0.958	0.951	0.917	1								
RSK	0.636	0.610	0.649	0.763	1							
Absorption	0.512	0.504	0.409	0.578	0.477	1						
Abbott FPC2	0.325	0.351	0.312	0.058	-0.386	-0.210	1					
Ltx FPC2	0.121	0.133	0.019	0.137	-0.097	0.048	0.112	1				
SRT	0.236	0.243	0.106	0.206	-0.046	0.296	0.158	0.150	1			
Ltx FPC3	-0.077	-0.091	-0.042	0.044	0.264	-0.083	-0.495	-0.030	-0.368	1		
RKU	-0.683	-0.663	-0.699	-0.685	-0.833	-0.388	-0.027	0.034	-0.005	0.061	1	
g	-0.648	-0.624	-0.642	-0.770	-0.960	-0.581	0.393	0.173	-0.044	-0.180	0.812	1

A.2.3 Multiple linear regression on the inner drum test bench's surfaces

Ribbed-slick

Table A.41: Results for the ribbed-slick tire on the inner drum test bench at the leading edge

Variable	Coefficient	Std. Error	t-Ratio	Prob>|t|
Speed	0.23	0.002	128.2	<.0001
(g-0.69)*Ltx FPC1	0.93	0.02	57.9	<.0001
MPD	4.65	0.11	41.2	<.0001
$(Speed-75.4)^2$	-0.002	7.4e-5	-27.2	<.0001

	R^2		RMSE [dBA]	
Training set	0.99		0.97	
Validation Set	0.98		1.03	

Table A.42: Results for the ribbed-slick tire on the inner drum test bench at the trailing edge

Variable	Coefficient	Std. Error	t-Ratio	Prob>|t|
Speed	0.23	0.002	123.7	<.0001
MPD	4.44	0.12	36.1	<.0001
(g-0.69)*Ltx FPC1	0.59	0.02	23.9	<.0001
$(Speed-75.4)^2$	-1.6e-3	7.7e-5	-20.3	<.0001
$Ltx\ FPC1^2$	-7.5e-4	5.3e-5	-14.1	<.0001

	R^2		RMSE [dBA]	
Training set	0.98		1.02	
Validation Set	0.98		1.10	

Table A.43: Results for the ribbed-slick tire on the inner drum test bench at the CPX-middle microphone

Variable	Coefficient	Std. Error	t-Ratio	Prob>|t|
Speed	0.24	1.59e-3	148.2	<.0001
MPD	7.41	0.10	71.8	<.0001
Ltx FPC1^2	-1.60e-4	3.1e-5	-52.0	<.0001
(Speed-75.4)^2	-1.91e-3	6.6e-5	-29.2	<.0001
	R^2		**RMSE [dBA]**	
Training set	0.99		0.86	
Validation Set	0.99		0.82	

Summer

Table A.44: Results for the summer tire on the inner drum test bench at the leading edge

Variable	Coefficient	Std. Error	t-Ratio	Prob>|t|
Speed	0.23	1.44e-3	162.4	<.0001
(g-0.69)*Ltx FPC1	0.72	0.012	56.2	<.0001
(Speed-75.4)^2	-2.1e-3	6.1e-5	-34.2	<.0001
MPD	1.81	0.09	19.9	<.0001
	R^2		**RMSE [dBA]**	
Training set	0.99		0.78	
Validation Set	0.98		0.84	

Table A.45: Results for the summer tire on the inner drum test bench at the trailing edge

Variable	Coefficient	Std. Error	t-Ratio	Prob>|t|
Speed	0.24	1.83e-3	129.0	<.0001
(g-0.69)*Ltx FPC1	0.92	0.01	67.6	<.0001
$(Speed-75.4)^2$	-1.86e-3	7.7e-5	-24.1	<.0001

	R^2	RMSE [dBA]
Training set	0.98	1.00
Validation Set	0.98	1.02

Table A.46: Results for the summer tire on the inner drum test bench at the CPX-middle microphone

Variable	Coefficient	Std. Error	t-Ratio	Prob>|t|
Speed	0.23	1.54e-3	151.7	<.0001
(g-0.69)*Ltx FPC1	0.43	0.01	31.1	<.0001
MPD	2.89	0.10	29.6	<.0001
$(Speed-75.4)^2$	-1.83e-3	6.5e-5	-28.1	<.0001

	R^2	RMSE [dBA]
Training set	0.99	0.84
Validation Set	0.98	0.83

Winter

Table A.47: Results for the winter tire on the inner drum test bench at the leading edge

Variable	Coefficient	Std. Error	t-Ratio	Prob>|t|
Speed	0.22	1.96e-3	111.0	<.0001
(g-0.69)*Ltx FPC1	0.68	0.015	46.7	<.0001
$(Speed-75.4)^2$	-1.91e-3	8.3e-5	-23.1	<.0001

	R^2	RMSE [dBA]
Training set	0.97	1.06
Validation Set	0.96	1.28

Table A.48: Results for the winter tire on the inner drum test bench at the trailing edge

Variable	Coefficient	Std. Error	t-Ratio	Prob>|t|
Speed	0.21	1.33e-3	160.7	<.0001
(Absorption-3.66)*(MPD-0.86)	-1.24	0.02	-59.4	<.0001
Load	1.0e-3	3.7e-5	27.2	<.0001
$(Speed-75.4)^2$	-1.29e-3	5.6e-5	-23.0	<.0001

	R^2	RMSE [dBA]
Training set	0.99	0.72
Validation Set	0.98	0.79

Table A.49: Results for the winter tire on the inner drum test bench at the CPX-middle microphone

Variable	Coefficient	Std. Error	t-Ratio	Prob>|t|
Speed	0.24	1.91e-3	123.3	<.0001
(Absorption-3.7)*(MPD-0.86)	-1.08	0.03	-31.9	<.0001
$(Speed-75.4)^2$	-1.74e-3	8.0e-5	-21.6	<.0001
MPD	1.83	0.11	16.0	<.0001
	R^2		RMSE [dBA]	
Training set	0.98		1.02	
Validation Set	0.97		1.13	

A.2.4 Multiple linear regression on ISO tracks only

Ribbed-slick

Table A.50: Results for the ribbed-slick tire on ISO 10844 test tracks with ISO parameters

Variable	Coefficient	Std. Error	t-Ratio	Prob>|t|
Speed	0.19	0.01	16.8	<.0001
Absorption	-91.11	5.65	-16.1	<.0001
(Absorption-0.02)*(MPD-0.53)	-446.32	43.23	-10.3	<.0001
MPD	5.03	0.54	9.4	<.0001
$(MPD-0.53)^2$	-25.13	4.09	-6.2	<.0001
	R^2		**RMSE [dBA]**	
Training set	0.81		0.96	
Validation Set	0.86		0.89	

Table A.51: Results for the ribbed-slick tire on ISO 10844 test tracks with all parameters

Variable	Coefficient	Std. Error	t-Ratio	Prob>|t|
Speed	0.18	0.01	28.6	<.0001
Absorption	-50.95	2.81	-18.1	<.0001
MPD	6.03	0.40	15.1	<.0001
(Abbott FPC1-0.15)*(Abbott FPC2+0.01)	-612.43	43.47	-14.1	<.0001
(MPD-0.53)*(Ltx FPC2-1.51)	0.92	0.07	13.1	<.0001
$(Abbott FPC1-0.15)^2$	-124.82	12.66	9.9	<.0001
SRT	0.05	0.005	-9.3	<.0001
	R^2		**RMSE [dBA]**	
Training set	0.93		0.56	
Validation Set	0.96		0.48	

Summer

Table A.52: Results for the summer tire on ISO 10844 test tracks with ISO parameters

Variable	Coefficient	Std. Error	t-Ratio	Prob>|t|
Speed	0.18	0.01	28.2	<.0001
Absorption	-57.43	3.98	-14.4	<.0001
(Absorption-0.02)*(MPD-0.53)	-318.01	32.36	-9.8	<.0001
MPD	-2.22	0.31	-7.2	<.0001
$(Absorption-0.02)^2$	-845.51	252.24	-3.3	0.0001

	R^2	RMSE [dBA]
Training set	0.85	0.56
Validation Set	0.72	0.67

Table A.53: Results for the summer tire on ISO 10844 test tracks with all parameters

Variable	Coefficient	Std. Error	t-Ratio	Prob>|t|
Speed	0.19	0.01	34.9	<.0001
Absorption	-36.93	2.02	-18.3	<.0001
(Abbott FPC1-0.16)*(Abbott FPC2+0.01)	-361.70	34.98	-10.3	<.0001
(MPD-0.53)*(Ltx FPC2-1.40)	0.43	0.06	7.8	<.0001
SRT	0.03	0.005	5.8	<.0001
RKU	0.15	0.03	5.0	<.0001

	R^2	RMSE [dBA]
Training set	0.90	0.45
Validation Set	0.81	0.56

Winter

Table A.54: Results for the winter tire on ISO 10844 test tracks with ISO parameters

Variable	Coefficient	Std. Error	t-Ratio	Prob>|t|
Speed	0.19	0.01	24.9	<.0001
Absorption	-32.04	4.23	-7.6	<.0001
$(MPD-0.53)^2$	12.87	2.53	5.1	<.0001
$(Absorption-0.02)^2$	1038.29	219.28	4.7	<.0001

	R^2		RMSE [dBA]	
Training set	0.78		0.62	
Validation Set	0.74		0.73	

Table A.55: Results for the winter tire on ISO 10844 test tracks with all parameters

Variable	Coefficient	Std. Error	t-Ratio	Prob>|t|
Speed	0.19	0.01	32.7	<.0001
(RMS-0.35)*(Abbott FPC2+0.01)	-559.02	41.72	-13.4	<.0001
Abbott FPC2	-16.95	1.82	-9.3	<.0001
SRT	0.03	0.005	6.9	<.0001
(Absorption-0.02)*(Abbott FPC1 2+0.15)	380.04	55.96	6.8	<.0001
(RKU-4.28)*(SRT-46.68)	-0.02	0.004	-4.2	<.0001

	R^2		RMSE [dBA]	
Training set	0.86		0.49	
Validation Set	0.84		0.56	

A.2.5 Multiple linear regression on all roads

Ribbed-slick

Table A.56: Results for the ribbed-slick tire on all roads with ISO parameters

Variable	Coefficient	Std. Error	t-Ratio	Prob>|t|
MPD	7.44	0.16	46.7	<.0001
Speed	0.19	0.01	22.9	<.0001
Absorption	-42.80	3.83	-11.2	<.0001
$(MPD-0.53)^2$	-2.10	0.34	-6.1	<.0001
$(Absorption-0.02)^2$	683.03	125.11	5.5	<.0001

	R^2	RMSE [dBA]
Training set	0.86	1.08
Validation Set	0.86	1.00

Table A.57: Results for the ribbed-slick tire on all roads with all parameters

Variable	Coefficient	Std. Error	t-Ratio	Prob>|t|
MPD	7.31	0.17	43.8	<.0001
Speed	0.19	0.01	22.4	<.0001
Absorption	-26.9	6.6	-8.2	<.0001
(RSK+0.78)*(Ltx FPC1+0.87)	-0.05	0.01	-5.3	<.0001
(g-0.73)*(SRT-48.07)	0.17	0.06	2.6	0.009

	R^2	RMSE [dBA]
Training set	0.85	1.10
Validation Set	0.85	1.03

165

Summer

Table A.58: Results for the summer tire on all roads with ISO parameters

Variable	Coefficient	Std. Error	t-Ratio	Prob>|t|
Speed	0.18	0.01	30.8	<.0001
MPD	2.64	0.11	22.9	<.0001
Absorption	-29.96	2.28	-13.2	<.0001
$(MPD-0.79)^2$	2.36	0.24	9.8	<.0001
		R^2		RMSE [dBA]
Training set		0.76		0.78
Validation Set		0.75		0.74

Table A.59: Results for the summer tire on all roads with all parameters

Variable	Coefficient	Std. Error	t-Ratio	Prob>|t|
Speed	0.18	0.005	35.2	<.0001
MPD	2.83	0.13	22.1	<.0001
Absorption	-25.44	1.98	-12.9	<.0001
(RKU-3.58)*(RMS-0.50)	-1.39	0.15	-9.0	<.0001
$(SRT-48.36)^2$	-0.002	0.0003	-7.4	<.0001
Ltx FPC2	-0.05	0.006	-7.1	<.0001
Ltx FPC3	0.05	0.01	5.6	<.0001
(Absorption-0.02)*(Ltx FPC2-0.08)	-1.63	0.41	-4.0	<.0001
(g-0.73)*(SRT-48.36)	0.20	0.05	3.6	0.0004
(Ltx FPC3-0.08)*(g-0.73)	-0.46	0.13	-3.6	0.0004
(Ltx FPC2-0.08)*Abbott FPC2	-0.31	0.11	-2.9	0.0004
		R^2		RMSE [dBA]
Training set		0.83		0.64
Validation Set		0.75		0.71

Winter

Table A.60: Results for the winter tire on all roads with ISO parameters

Variable	Coefficient	Std. Error	t-Ratio	Prob>|t|
Speed	0.19	0.01	32.4	<.0001
MPD	1.86	0.12	15.9	<.0001
Absorption	-12.65	2.11	-6.0	<.0001
$(MPD-0.79)^2$	1.13	0.24	4.8	<.0001
	R^2		RMSE [dBA]	
Training set	0.74		0.79	
Validation Set	0.69		0.80	

Table A.61: Results for the winter tire on all roads with all parameters

Variable	Coefficient	Std. Error	t-Ratio	Prob>|t|
Speed	0.20	0.005	40.9	<.0001
MPD	1.66	0.10	16.9	<.0001
(SRT-48.46)*Abbott FPC2	0.88	0.08	11.2	<.0001
SRT	0.04	0.004	10.0	<.0001
Ltx FPC3	0.08	0.01	9.3	<.0001
Ltx FPC2	-0.07	0.01	-9.1	<.0001
(RKU-3.58)*Abbott FPC2	-6.02	0.77	-7.8	<.0001
(Absorption-0.03)*(Ltx FPC2-0.27)	-2.55	0.36	-7.1	<.0001
(RSK+0.77)*(Ltx FPC2-0.27)	0.13	0.02	6.3	<.0001
(RKU-3.58)*(SRT-48.46)	-0.01	0.004	-3.3	0.0025
	R^2		RMSE [dBA]	
Training set	0.83		0.64	
Validation Set	0.75		0.71	